Graphene Based Terahertz Devices

Vom Fachbereich Elektrotechnik und Informationstechnik
der Technischen Universität Darmstadt
zur Erlangung des akademischen Grades eines
Doktor-Ingenieurs (Dr.-Ing)
genehmigte Dissertation

von

Alaa Jabbar Jumaah, M.Sc.

geboren am 01. März 1984
in Bagdad

Referent:	Prof. Dr. Thomas Kusserow
Korreferent:	Prof. Dr. Ir. Idelfonso Tafur Monroy
Tag der Einreichung:	15. September 2020
Tag der mündlichen Prüfung:	26. Mai 2021

D17
Darmstadt 2020

Jumaah, Alaa: Graphene Based Terahertz Devices
Darmstadt, Technische Universität Darmstadt
Jahr der Veröffentlichung der Dissertation auf TUprints: 2021
URN: urn:nbn:de:tuda-tuprints-192229
Tag der mündlichen Prüfung: 26.05.2021

To the memory of my father, my mother, my brothers, my sisters, my wife, and my two eyes
(Layan and Kinaan)

Acknowledgements

This dissertation originates from my research activity at the Institute for Microwave Engineering and Photonics at the Technische Universität Darmstadt as a doctoral student. I am so grateful to the Innovative Training Network Convergence of Electronics and Photonics Technologies for Enabling Terahertz Applications (ITN CELTA) under grant number 675683 of Call: H2020-MSCA-ITN-2015.

I wish to express my deepest gratitude to Prof. Dr. Thomas Kusserow for his guidance, caring, patience, and providing me with an excellent atmosphere for doing research.

I would like to express my deep gratitude and appreciation to my inspiration source and practical mentor Dr.-Ing. Shihab Al-Daffaie for his guidance, helpful suggestion, encouragement, and his time that he gave me during this work.

A significant part of the work was possible due to the close collaboration with PD Dr.-Ing. habil. Oktay Yilmazoglu. I place on record, my sense of gratitude to him for his support in technology laboratory and sharing his great experience with me.

I would like to express my deep gratitude and appreciation to Dr. Sandeep Yadav, who helped me with the SEM images and the Raman characterization.

Special thanks to my good friends and colleagues at the Institute for Microwave Engineering and Photonics, especially Dr.-Ing. Julijan Cesar, M.Sc. Anuar Fernandez Olvera, and M.Sc. Ángel Blanco Granja. They were always willing to help and give their best suggestions. I am also deeply thankful one and all, who directly or indirectly, have helped or tried to help me during these exciting years. Very special thanks to Andreas Sermrad and Peter Kießlich for their great technical support and cooperation.

There are no enough acknowledgment and grateful words to my family, especially my mother. She was the biggest support and encouragement source for me. I am so grateful to my beloved wife for her understanding, support, and caring despite the difficulties that she had to face during these years.

Darmstadt, September 2020 Alaa Jabbar Jumaah

Abstract

Terahertz waves enable many applications such as microscopic imaging with a very high spatial resolution due to the (sub-)mm wavelength. Moreover, many optically opaque materials such as paper, envelopes, clothes, or many kinds of plastic are transparent to terahertz radiation. Additionally, the corresponding photon energy of the terahertz radiation, 1 - 100 meV, is harmless for various materials and biomolecules. Therefore, the terahertz wave is much safer in medical applications compared to X-rays waves. The development of technology to enhance terahertz devices (sources and detectors) was one of the biggest challenges in the terahertz field. Conventional interdigitated photomixers are one of the main efficient devices that can generate and detect terahertz radiation. However, these types of photomixers have many limitations that restricted the operation performance.

This dissertation presents new types of terahertz photomixers based on nanoelectrodes (single and multilayer graphene) that significantly enhance the terahertz output power, detection sensitivity, and operational performance. The nanoelectrodes design enhances the device characteristics directly and the operational performance. The DC measurements of the graphene photomixers indicated highly improved performance as compared to the conventional devices. The graphene photomixers showed a large increase in the generated photocurrent (more than one order of magnitude) and proved the device's reliability under very high bias voltage without damage. The terahertz measurement results of the graphene photomixers clearly enhanced by 30 times due to the effect of high transparency, electrical conductivity, and thermal conductivity of the graphene. The improvement of the terahertz output power in graphene devices compared to the conventional devices leads to potential applications in a higher terahertz frequency range.

This dissertation presents a novel approach to enhance the terahertz output power of the new types of photomixers with hybrid nanoelectrodes based on graphene and silver nanowires. Similar to graphene photomixers, the hybrid nanoelectrodes photomixers recorded even higher generated photocurrent (more than two orders of magnitude), 50 times higher terahertz output power, and device reliability under very high bias voltage without damage as compared to the conventional interdigitated photomixers. In this dissertation, all respective fabrication, characterization, and measurement details are presented and described.

Zusammenfassung

Terahertzwellen ermöglichen viele Anwedungen, wie makroskopische Bildgebung mit sehr hoher räumlicher Auflösung dank der sub-Millimeter Wellenlänge. Außerdem sind viele lichtundurchlässige Materialien, wie Papier, Briefumschläge, Kleidung, sowie viele Plastiken transparent gegenüber Terahetzstrahlung. Darüber hinaus ist die entsprechende Photonenenergie der Terahertzstrahlung, 1 - 100 meV, für viele Materialien und biologischem Gewebe unschädlich. Deswegen ist Terahetzstrahlung im medizinischen Umfeld viel sicherer im Vergleich zu Röntgenstrahlung. Die technologische Entwicklung, um Terahertzbauteile (Quellen und Detektoren) zu verbessern war eine der größten Herausforderungen im Bereich von Terahertz. Herkömmliche fingerförmig ineinandergreifende Photomischer sind die effizientesten Bauteile, welche Terahertzstrahlung erzeugen und detektieren können. Jedoch hat dieser Typ von Photomischern viele Einschränkungen, die die Leistungsfähigkeit begrenzen.

Diese Dissertation präsentiert neue Arten von Terahertz Photomischern basierend auf Nanoelektroden (einschichtiges und mehrschichtiges Graphen), welche die Terahertz Ausgangsleistung, die Detektorsensitivität und Leistungsfähigkeit signifikant erhöht. Das Nanoelektrodendesign verbessert die Bauteilcharakteristik und Leistungsfähigkeit direkt. Gleichstrommessungen von Graphenphotomischern zeigen eine deutliche Leistungssteigerung im Vergleich zu herkömmlichen Bauteilen. Graphenphotomischer zeigen eine große Steigerung des Photostroms (mehr als eine Größenordnung) und zeigen eine hohe Zuverlässigkeit, da sie hohe Biasspannungen ohne Schaden überstehen. Terahertzmessungen von Graphenphotomischer zeigen eine Erhöhung der Ausgangsleisgung um einen Faktor von 30 dank erhöhter Transparenz, sowie elektrischer und thermischer Leitfähigkeit des Graphens. Die Verbesserung der Terahertzausgangsleistung der graphenbasierenden Bauteile im Vergleich zu herkömmlichen Bauteilen ermöglicht das Potential für Anwendungen in einem Bereich höherer Terahertzfrequenzen.

Diese Arbeit präsentiert außerdem einen neuartigen Ansatz, um die Terahertzausgangsleistung von Photomischern mit hybriden Nanoelektroden basierend auf Graphen und Silbernanodrähten zu steigern. Ähnlich zu Graphenphotomischern, zeigen Photomischer mit hybriden Nanoelektroden einen noch größeren Photostrom (mehr als zwei Größenordnungen), 50 fache Terahertzausgangsleistung, sowie die Möglichkeit hoher Biasspannungen ohne Beschädigungen im Vergleich

zu herkömmlichen fingerförmig ineinandergreifenden Photomischern. In dieser Dissertation sind alle Details zu Prozessierungsschritten, Charakterisierungen und Messungen präsentiert und beschrieben.

Contents

Chapter 1

Introduction

1.1 Terahertz Photomixers

Terahertz (THz) radiation falls in between infrared radiation and microwave radiation in the electromagnetic spectrum. It covers the frequencies range between 0.1 THz and 10 THz. For a long time, due to the impossibility to overcome the limitation of the high-frequency end of RF sources or the low-frequency end of optical emitters, this frequency range had called the THz gap. Despite the difficulties to close this gap, this range of frequencies, whose wavelengths are from 3 mm to 30 μm and energy range from 0.4 to 40 meV, has attracted the scientific community. The interest in this frequency range is attributed to the wide potential applications in security [1], imaging [2], biology [3], medicine [4], material spectroscopy [5], and many other application fields. To fulfill such application requirements, many efforts were done within the last decade to fabricate and improve highly powerful THz sources with high cut-off frequencies of up to several THz at room temperature operation and highly sensitive THz detectors [6–9]. With the modern advances in this field, various THz sources are available nowadays. Currently, the main sources for THz radiation are based on either electronic sources, optical sources, or optoelectronic sources (photomixers). Photomixers are suitable for THz generation and detection. A photomixer uses interdigitated metal electrodes, such as gold material, placed on top of a planar high-speed photoconductive material such as low-temperature-grown (LTG) gallium arsenide (GaAs) [10]. The THz generation is defined as an optical heterodyne down-conversion of the optical beat signal, which consists of two optical laser sources. When the optical beat signal illuminates the active area of the photomixer, the THz photocurrent oscillation is generated at a frequency corresponding to the frequency difference between the two optical laser sources. By the applied biased field the generated photocurrent is tapped off there via gold electrodes and coupled to a suitable antenna for THz radiation into the photoconductive material. These photomixers have limitations. The gold opaqueness reduces the optical to electrical conversion efficiency that results in very low output power. Moreover, the combination of the optical power and the electrical power in the device causes heating [11]. Such heating can result in device thermal failure. Furthermore, the spectral bandwidth of a photomixer has two roll-off characteristics, the carrier lifetime and the device capacitance. At the low range of THz frequency, the main roll-off that limits the output power is the carrier lifetime. On the other hand, at the high range of THz frequency, the capacitance roll-off limits the spectral bandwidth of the photomixer. The lower photomixer capacitance results in higher THz output power at the upper part of the THz range. It is still necessary to obtain high-performance photomixer sources for several THz to be useful for extended practical applications.

Transparent nanoelectrodes instead of the conventional metal electrodes can improve the optical to electrical conversion efficiency and improve the reliability of the device. The nanoelectrodes configurations and technological steps can result in higher photocurrent as well as higher radiated power. These improvements are independent of the usual device optimization, which needs to change the band structure of the photoconductive material to reduce the carrier lifetime and change the antenna configuration to obtain better match impedance [12–15].

Terahertz antennas based on plasmonic resonant graphene sheets were analyzed and designed using Ansys HFSS software by M. Tamagnone et al. [16]. The authors showed that graphene is a promising material for the realization of miniaturized resonant THz antennas. The radiation efficiency is good given the extremely small electrical size, leading to performances even better as compared to the metal implementations. Additionally, the authors showed that their concept and analysis can be extended to enable dynamic reconfiguration of the terahertz plasmonic antenna concept using a graphene stack [17]. In 2013, V. Ryzhii et al. proposed a terahertz photomixing using plasma resonances in double-graphene layer structures [18]. The concept of terahertz photomixing enabled by the interband electron transitions due to the absorption of modulated optical radiation in double-graphene layer structures and the resonant excitation of plasma oscillations. According to their device model calculations, the model predicts that the radiation output power can exhibit sharp plasma resonant peaks in the THz range with the peak power markedly exceeding that at relatively low frequencies. In the same year, the concept of a graphene-based nanoantenna-enhanced photomixer to realize wideband-tunable THz frequency generation was proposed in [19]. In the model, double layers of graphene were used to guide and coupled the generated THz waves to a loading circuit. The high optical transparency graphene layer may allow exciting plasmonic nanoantennas around its tip in order to boost the intensity of pumped visible light.

In our group, a continuous-wave (CW) THz generation based on photomixer devices using nanowire electrodes was demonstrated in 2012 [20]. The use of nanowire electrodes instead of metal electrodes decreased the photomixer capacitance, resulting in higher THz output power than that of the conventional interdigitated metal photomixer. Despite their small size, the nanowires have shown a high ability to handle high current densities. However, the alignment of the nanowire electrodes was a critical issue. Therefore, a transparent 2D nanomaterial with a high capacity to handle high current densities was needed to replace the nanowire electrodes regardless of the device's capacitance. Since then, the high transparent graphene sheet was proposed to replace the nanowire electrodes. Al-Daffaie et al. had measured the short-circuit current of the multilayer graphene sheet as 9 mA per 10 μm width, resulting in a high current density of 40 MA/cm^2 [21]. In 2015, the first graphene photomixer was fabricated by Al-Daffaie et al. [22]. The graphene photomixer was fabricated with 2D multilayer graphene electrodes. The graphene photomixer showed a clear improvement in the performance of the device as compared with the conventional interdigitated photomixer. Where the graphene photomixer showed three times higher generated photocurrent than the generated photocurrent of conventional interdigitated photomixer, which results in twice THz output signal higher than that of the conventional device. Furthermore, graphene photomixer shows very high reliability under a high bias voltage.

Proceeding from this point, graphene is used in this dissertation to enhance the reliability of the THz photomixers under high generated photocurrent and increase the output THz power. The use of the graphene nanoelectrodes allows efficient optical power illumination to generate high photocurrent generation and shows highly reliable continuous-wave THz emissions. Various graphene nanoelectrodes designs were performed to decrease the device capacitance or to shorten the transit time required for the generated photocarriers to travel from one electrode to another. The new designs of graphene nanoelectrodes would further increase the photocurrent and the THz output power. This dissertation discusses a significant improvement of the THz output power for photomixers using new nanostructure configurations and technological steps.

1.2 Thesis Overview and Organization

The working principle of THz emitters and detectors based on photomixer devices was described in detail in Chapter 2. Various THz antennas were described in Chapter 2 as well.

Chapter 3 gives an introduction to the unique electrical, optical, and thermal properties of graphene material. Furthermore, the types of graphene used in this dissertation were described and compared.

Chapter 4 describes the possibility of replacing the metallic electrodes with graphene material. Additionally, Chapter 4 discusses the fabrication of an enhanced photomixer based on various graphene types and their characterization. Various nanoelectrodes forms have fabricated on top of LTG-GaAs as photoconductive material.

Chapter 5 shows the results of the generated photocurrent and the output THz signals of graphene THz photomixer emitters and compares them with the generated photocurrent and the output THz signals of conventional interdigitated photomixer emitters.

Chapter 6 describes the effect of the graphene transparency on the sensitivity of THz detectors. The results of the detected photocurrent of graphene THz photomixer receivers were compared with the results of conventional interdigitated THz photomixer detectors.

Chapter 7 shows further improvements in the performance of the photomixer using hybrid nanoelectrodes based on graphene and silver nanowire. Chapter 6 discusses various hybrid designs, fabrication steps, and obtained results of the generated photocurrent, and output THz powers.

Finally, Chapter 8 explores the achieved results and estimates future viewpoints.

Chapter 2

Conventional Terahertz Photomixers

Conventional photomixers use interdigital gold fingers as electrodes on top of a thin layer of photoconductive material, such as LTG-GaAs. These types of devices are suitable for THz generation and detection. Emitters are used to convert the optical beat signal into continuous waves at THz frequencies with the presence of a bias voltage. While detectors are used to convert the THz wave into an electrical signal by modulating the optical beat signal. The fundamentals of both types of photomixers are described in this chapter.

2.1 THz Photomixer Emitter

The conventional emitters are compact sources that use a pair of a single frequency and tunable laser sources for THz difference frequency generation by photoconductive mixing in LTG-GaAs. The resulting frequency can be tuned over several THz by tuning the frequency of the two laser sources. The laser frequency can be tuned due to the resulting shift in the laser wavelength by controlling the temperature or current of the two laser sources. A few nanometers in wavelength can be achieved in the case of diode lasers, such as distributed feedback laser diodes (DFB-LDs). The benefits of using these types of optoelectronic sources lie in:

1. **Room temperature operation**

   Electronic and optical THz sources need expensive and bulky cooling units to have reliable performance. On the other hand, photomixers sources, even detectors, can operate efficiently enough at room temperature for broad applications in real life. This feature will increase the compactness of the system.

2. Compactness, cost-efficiency, and ease-of-use

Photomixer sources have shown high performance with respect to their low cost, and less fabrication complexity as for the other THz sources. The use of optoelectronic THz devices promises a very compact THz emitter and detector in the THz measurement systems.

3. Low noise level

The noise characteristics of a receiver (photomixer) are very important. Photomixer receivers operate based on phase matching optical detection of the electrical field of the THz wave. The noise current in the photomixer receivers is the value of the root mean square of the generated current when the photomixer emitter is switched off. The noise measurements take place in the calculation of the high signal-to-noise ratio, which is known as the dynamic range of the terahertz power. In this sense, the noise will be eliminated even though the available THz power is only moderate.

Furthermore, CW THz photomixers have significant properties that put them into a leading position for the search for practical THz applications. In contrast to pulse photomixers as well as the electrical and optical sources, the CW THz photomixers are easy to tune over a large frequency range. The tuning range is done by the operation wavelength difference of the optical beat signal. Therefore, a CW THz system is capable of achieving a frequency resolution in the order of several MHz (< 10 MHz) by its fine and wide frequency tuning range of the beat signal, while the frequency resolution for the pulse system is about 5 GHz [23]. This feature leads the CW THz system to be the ideal system for high-resolution spectroscopy measurement [24, 25].

2.1.1 The Principle of Photomixing

THz photomixer emitter generates THz waves using the optical heterodyne down-conversion [26]. A conventional interdigitated photomixer consists of a photoconductive material that is excited with an optical beat signal. Two detuned DFB-LDs with different angular frequencies ω_1 and ω_2 are interfered with to generate the optical beat signal in a beam with a frequency corresponding to the frequency difference between the two DFB-LDs. The electric field of the optical beat signal is given by

$$E_{beat}(t) = E_1 e^{i(\omega_1 t)} + E_2 e^{i(\omega_2 t + \phi)} \tag{2.1}$$

where ϕ is the phase difference between the two optical signals. The incident optical beat power $P(t)$ at the surface on the photoconductive material is given by the following equations [27]

$$P(t) \propto |E_{beat}(t)|^2 \sim E_{beat}(t) \cdot E^*_{beat}(t) \tag{2.2}$$

$$P(t) = \left[E_1 e^{i(\omega_1 t)} + E_2 e^{i(\omega_2 t + \phi)}\right]\left[E_1 e^{-i(\omega_1 t)} + E_2 e^{-i(\omega_2 t - \phi)}\right] \tag{2.3}$$

$$P(t) = E_1^2 + E_2^2 + E_1 E_2 e^{i(\omega_1 - \omega_2)t - \phi} + E_1 E_2 e^{-i((\omega_1 - \omega_2)t - \phi)} \tag{2.4}$$

$$P(t) = E_1^2 + E_2^2 + E_1 E_2 \left[e^{i(\omega_1 - \omega_2)t - \phi} + e^{-i((\omega_1 - \omega_2)t - \phi)}\right] \tag{2.5}$$

$$P(t) = E_1^2 + E_2^2 + 2E_1 E_2 \cos((\omega_1 - \omega_2)t - \phi) \tag{2.6}$$

where $\cos((\omega_1 - \omega_2)t - \phi)$ is the intermediate freqency signal in THz region with frequency $\omega_{THz} = |\omega_1 - \omega_2|$ and at phase ϕ. Therefore, the total incident optical beat signal will be

$$P(t) = P_1 + P_2 + 2\sqrt{m P_1 P_2} \cos(\omega_{THz} t - \phi) \tag{2.7}$$

The average of the total incident power through a long time period $P_1 + P_2$ ranges between zero and one, and m is the mixing efficiency represented by the overlap between the two DFB-LDs. The resulted beat signal is used to illuminate the active region around the metal electrodes to generate instantaneous photocarrier pairs (electrons and holes) in the semiconductor periodically. The photocarrier pairs are

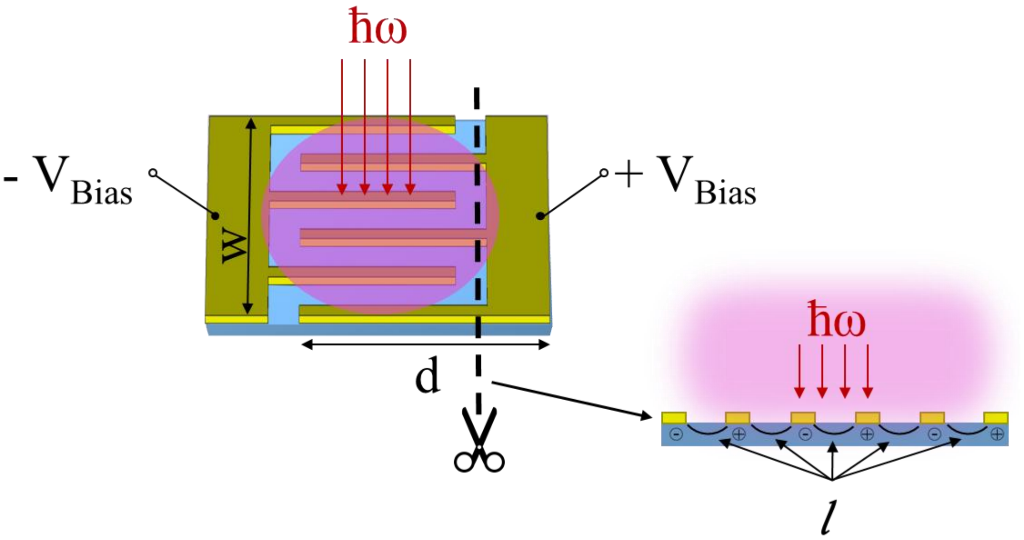

FIGURE 2.1: Conventional interdigitated photoconductive.

separated by an external field due to a DC bias. Otherwise, they will recombine again after a certain lifetime τ_c. Therefore, the number of generated photocarriers due to the applied light is the generation rate G_r multiply by the electron recombination lifetime, and it is given by

$$n_c(t) = \tau_c G_r = \tau_c \left(\eta_{ab} \frac{P(t)}{\hbar\omega\, A.l} \right) \tag{2.8}$$

where $P(t)$ is the absorbed optical power, η_{ab} is the absorption efficiency factor, $\hbar\omega$ is the photon energy, A is the area of the electrodes, and l is the transit path length that the generated photocarriers would follow to transport from one electrode to another.

The instantaneous photocarriers density $n_c(t)$ is produced an instantaneous photoconductance $G_{ph}(t)$ [28]. The total conductance of the photoconductor is the combination of the photoconductance due to the generated photocarriers, $G_{ph}(t)$, and the dark conductance G_{dark} generated due to impurities and dislocations in the photoconductive material crystal. The total conductance is given as [29]

$$G_{total}(t) = G_{ph}(t) + G_{dark} \tag{2.9}$$

Using the geometry in Figure 2.1, the $G_{ph}(t)$ is given as:

$$G_{ph}(t) = e n_c(t) \mu_c \frac{A}{l} \tag{2.10}$$

where μ_c is the carrier mobility, e is the electron charge, $A =$ W.d is the area of the electrodes, W is the width, and d is the total contact length of the photoconductor.

The total induced photocurrent $I_{ph}(t)$ in a photomixer device due to the incident optical beat signal with the presence of the bias voltage V_{bias} is given as [30]

$$\begin{aligned} I_{ph}(t) &= G_{ph}(t) V_{Bias} \\ &= \sigma_{ph}(t) \cdot \frac{A}{l} V_{Bias} \\ &= e \mu_c n_c(t) \frac{A}{l} V_{Bias} \end{aligned} \tag{2.11}$$

where $\sigma_{ph}(t) \cdot \frac{A}{l}$ is the conductivity over a unit volume. By substituting Equation 2.8 into equation 2.11 yields

$$I_{ph}(t) = \eta_{ab} P(t) \frac{e}{\hbar\omega} \tau_c \left(V_{Bias} \frac{\mu_c}{l^2} \right) \tag{2.12}$$

In photoconductive devices, the photocarriers, once generated, drift to the electrodes. They would follow a transit length toward the electrodes, which depends on the position in the structure where the photocarrier is generated. The relatively large separation of the electrodes implies a longer required transit time τ_t. This can be represented by the carrier's drift velocity $= \mu_c E$.

$$\tau_t = \frac{l}{\mu_c E} \tag{2.13}$$

It is known that the electric field is the voltage drop over the length of the conductor

$$E = \frac{V}{l} \tag{2.14}$$

From equations (2.13) and (2.14), the transit time in terms of voltage can be obtained

$$\tau_t = \frac{l^2}{\mu_c V} \tag{2.15}$$

Using equation (2.15) and solve it for the generated photocurrent $I_{ph}(t)$

$$I_{ph}(t) = \eta_{ab} P(t) \frac{e}{\hbar\omega} \left(\frac{\tau_c}{\tau_t}\right) \tag{2.16}$$

The term $\eta_{ab} P(t) \frac{e}{\hbar\omega}$ represents the number of generated electron—hole pair and the term $\frac{\tau_c}{\tau_t}$ is the photoconductive gain. The low quantum efficiency of the interdigitated electrodes photomixer limits the performance device. This low efficiency is raised from the low photoconductive gain because of the long carriers' transit time as compared to the carriers' recombination time. Electrodes configuration plays an important role in device performance. Smaller gaps between the electrodes result in shorter transit time. This would increase the photoconductive gain. However, smaller gaps increase the device capacitance and limit the optical to electrical conversion efficiency and the output power of the device at high frequency. On the other hand, Larger gaps between the electrodes reduce the device capacitance but increase the required transit time of the carrier to travel to the electrodes [31].

The resulting photocurrent contains a THz component due to the periodic modulation of the carrier generation rate [32, 33]. The high-frequency wave can be directly coupled from the photoconductive material into a suitable antenna for THz radiation. The output power of a THz photomixer P_{THz} is defined as [28]

$$P_{THz}(t) = \frac{I_{ph}^2(t) R_A}{2[1+(\omega\tau_c)^2][1+(\omega R_A C)^2]} \tag{2.17}$$

where R_A is the antenna resistance, and C is the device capacitance. R_A is fixed for the chosen antenna design, and τ_c is constant for the photoconductive material. A planer LTG-GaAs is well suited to photomixing applications because of its short carrier lifetime ($\sim$ 0.25 ps), relatively high mobility (>200 $\text{cm}^2\text{V}^{-1}\text{s}^{-1}$) for photoexcited electrons, and high electrical breakdown field (5×10^5 V/cm) [33]. Therefore, the THz output power can be increased by decreasing the device capacity and increasing the photocurrent.

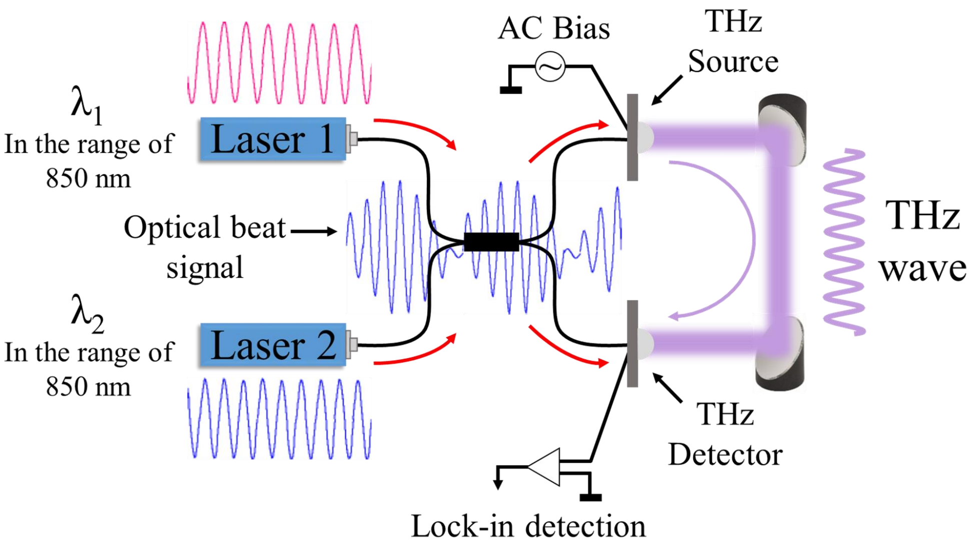

FIGURE 2.2: Coherent detection diagram for the CW—THz system.

However, these conventional interdigitated photomixers have limitations regarding bias voltage, optical beat signal power, reliability at high photocurrents, and the effective local heat dissipation which reduces the THz output power.

Furthermore, several breakdown mechanisms limit the reliability and the lifetime of the THz photomixer. The thermal effect of excessive power dissipation and electromigration in metal electrodes, among several, cause catastrophic device failure [22].

2.2 THz photomixer Detector

The significant advantage of photomixer devices is that they can also be used as THz detectors. In this approach, a detector will be operated without an external bias field. In CW homodyne detection systems, two photomixer devices are implemented. The first photomixer emitter is used to generate THz waves. The second photomixer receiver is used to detect the generated THz waves. In the strategy, the optical beat signal is split into two paths, as shown in Figure 2.2. The first path is used for the THz source, where the device needs a bias field to generate THz waves, as previously explained in section 2.1.1. The optics parts, the lenses, and parabolic mirrors were used to align and focus the THz beam onto the photomixer receiver. The second path is used for the THz detector. The incident optical beat signal directly to the active area of the device creates free carriers. The electric field of the incoming THz radiation induces a transient bias voltage across the gap between

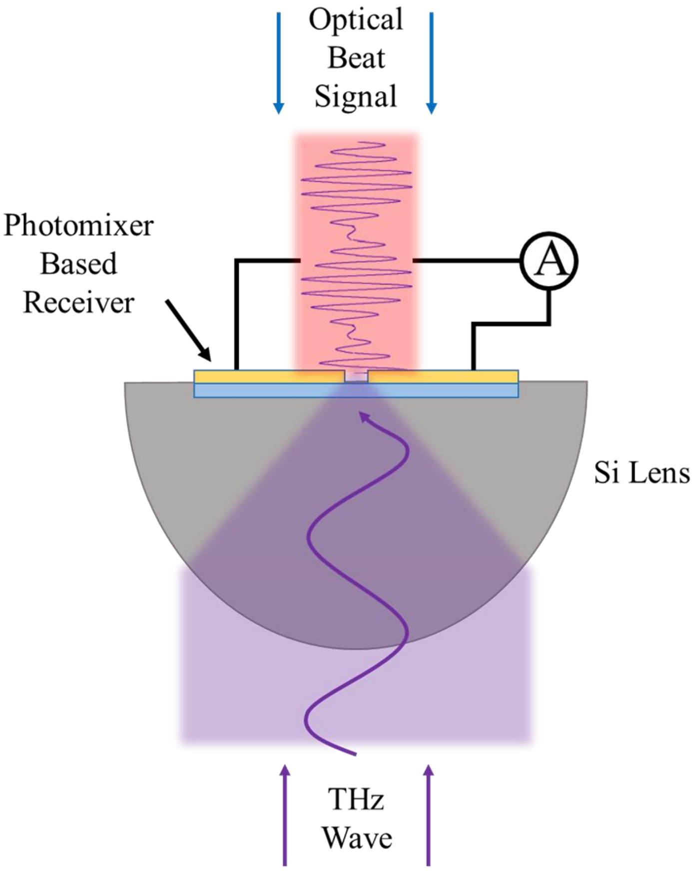

FIGURE 2.3: Photoconductive detector mounted on a hemispherical lens.

the two contacts of this receiver's antenna. The THz induced voltage separates the generated photocarriers and induced a photocurrent. The detected photocurrent is proportional to the product of the optical beat signal and the THz field, as shown in Figure 2.3. Therefore, the same principle of increasing the generated photocurrent is applied here. Increasing the number of generated photocarriers will result in a higher detected photocurrent [32, 34, 35].

2.2.1 Coherent Detection

According to the coherent detection scheme in Figure 2.2, one photomixer was used as a THz emitter, while another one was served as a THz receiver. For the second photomixer, both the terahertz wave and the original laser beat illuminate the receiver. The optical beat signal was applied to generate photocarriers. In the opposite direction, the incoming terahertz wave was employed as a bias field and generates a voltage drop between the antenna contacts. So, the optical beat signal modulates the conductivity of the photomixer. Equation (2.11) is valid here, where

$V_{Bias} = V_{THz}$ and $I_{ph} = I_{det}$. The detected photocurrent will be given by the following equations

$$\begin{aligned} I_{det} &= V_{THz}\frac{A}{L}\sigma \\ &= V_{THz}\frac{A}{L}e\mu_c n_c \end{aligned} \tag{2.18}$$

The detected photocurrent is proportional to the amplitude of the terahertz electric field and the phase difference $\triangle\varphi$ between the optical beat wave and the terahertz wave. The phase difference can be adjusted by varying the path difference between the fiber length of the receiver arm, and the fiber length of the emitter arm plus the terahertz path.

$$\triangle\varphi = 2\pi\nu_{THz}\Delta L/c \tag{2.19}$$

Thus, the amplitude of detected photocurrent represents the amplitude of the terahertz electric field when ΔL is zero, i.e. when the optical beat signal is in phase with the incident THz wave.

The use of nanomaterials, such as graphene, as transparent electrodes, results in an increase in the number of the generated photocarriers and increases the generated and the detected photocurrent for both types of photomixers (sources and detectors).

2.3 Broadband Antenna

The antenna design plays a crucial role in the polarization, pattern, and bandwidth of the radiated waves. The THz photomixer device used a planar antenna that is deposited on top of a photoconductive material. The contact of the photomixer fingers should be deposited onto the antenna contact directly. The tuning range of the THz radiation is mainly limited by the antenna design, where the lower and the upper cutoff frequency is determined by the antenna configuration.

2.3.1 Bow-Tie Antenna

A Bow-Tie antenna consists of two triangular sheets of metal, as shown in Figure 2.4. The main advantages of this type of antenna are simple design and broadband

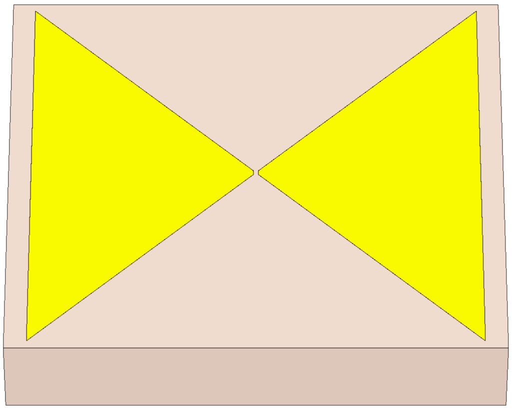

FIGURE 2.4: Bow-Tie antenna.

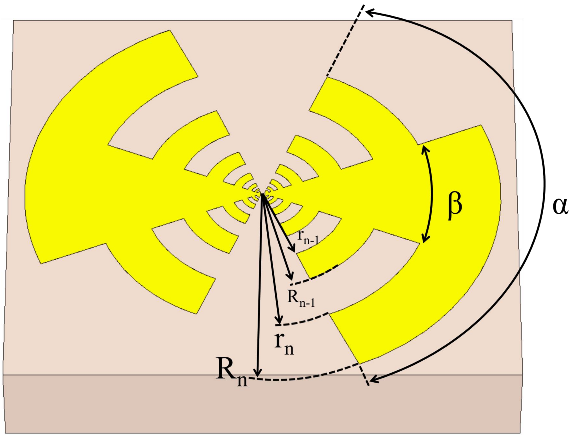

FIGURE 2.5: Log-Periodic antenna.

impedance. The bandwidth of this type of antenna is limited due to the finite gap between the feed points and finite size. The radiation of a Bow-Tie antenna is linearly polarized and has a bidirectional pattern with broad main beams perpendicular to the plane of the antenna [36].

2.3.2 Log-Periodic Antenna

The Log-Periodic antenna depicted in Figure 2.5 is considered a resonant antenna. It consists of a Bow-Tie antenna with attached self-complementary resonant teeth. These teeth are resonant at [37]

$$f_n = \frac{2c}{\pi (R_n + r_n)\sqrt{\varepsilon_{eff}}} \tag{2.20}$$

where ε_{eff} is the effective permittivity of the photoconductive material. Therefore, the radiated power is enhanced at this frequency f_n. The radiation power is linearly polarized parallel to the teeth edges. This is perpendicular to that of the Bow-Tie

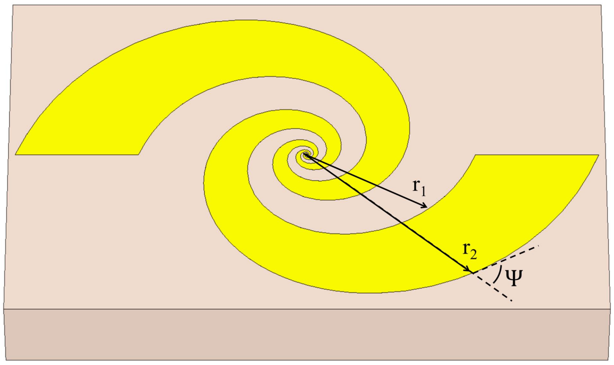

FIGURE 2.6: Spiral antenna.

antenna. This shows that the component of current that flows in the direction of the teeth dominates the radial component. The operation bandwidth is determined by the smallest and largest tooth. The upper cutoff frequency is limited by the gap defined by the photomixer. Typically the maximum frequency is limited to 4-5 THz. The lower cutoff frequency is limited by the space requirement of the antenna on the chip, which increases proportionally to the wavelength [38]. For the THz band, the lower cutoff frequency is typically chosen not much less than 100 GHz for sub-mm sized antennas.

2.3.3 Spiral Antenna

The spiral antenna shown in Figure 2.6 provides a relatively constant input impedance. The spiral antenna is designed to be frequency-independent antennas and circularly polarized with a sense that depends on the winding sense of the spirals. The spiral antenna has an almost constant radiation pattern and operates in very wide bandwidths. The low cutoff frequency is limited by the outer circumference of the spiral. The overall arm length L_{ant} is [37, 39]

$$L_{ant} = \frac{r_{2,max} + r_{1,max}}{2\cos(\Psi)} \tag{2.21}$$

On the other hand, the upper cutoff frequency depends on the configuration near the feed point. The main advantage of a spiral antenna is that it can receive linearly polarized waves in any orientation.

2.4 Typical Device Failure Mechanisms

Conventional interdigitated photomixer based on metal electrodes have limitations regarding performance reliability. The optical to electrical conversion is limited due to the opaqueness of the metallic electrodes, which limits the device output power. The device output power is limited by the maximum optical power that these devices can withstand before failure. The combination of optical power and electrical power causes heat in the small active area of the device, which results in the device's catastrophic thermal failure. The weakness of high heat dissipation from the small active area to the large size of the antenna metal through the electrodes results in dielectric breakdown due to the high heat collected in photoconductive material. The reliability of the THz devices is affected mainly by three breakdown mechanisms [21, 22].

2.4.1 Electromigration Failure

The transport phenomenon of electrons that occurs in metal electrodes due to the high current flow or due to the high electric field is known as electromigration. The high current density, electric field, temperature, and atom crystallinity can result in so-called device electromigration failure. Where the atomic displacement in the direction of electron flow occurs when a high current density exceeds 2×10^5 A/cm^2 [40]. The electric field that acts on atoms, which are not completely shielded by electrons, causes an opposite mass flow [41].

In this sense, the metallic lines suffer from high current flow, which causes damage to the electrodes (voids at the cathode side and hillocks at the anode side), on one hand. On the other hand, the high electric field creates voids on the anode side and hillocks on the cathode side. In general, either the current flow or the electric field dominates the electromigration behavior [22]. In [22], it has been shown that the conventional interdigitated emitter starts to fail when the photocurrent increases above $> 400\ \mu$A. The electromigration effect of the conventional interdigitated device is shown in Figure 2.7.

2.4.2 Thermal Failure

Due to the small size of the photomixer, the overheating in the device is a critical issue for the device's reliability. The high device temperature-induced is caused by the combination of optical and electrical powers. The absorbed optical power in the

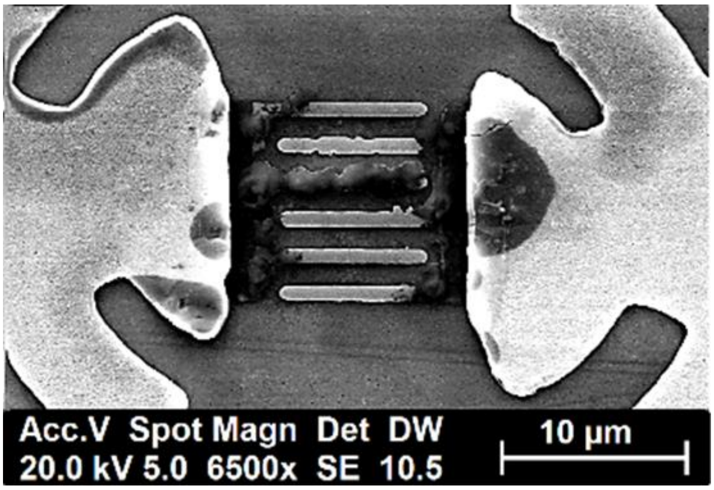

FIGURE 2.7: Electromigration failure of the interdigital photomixer [22].

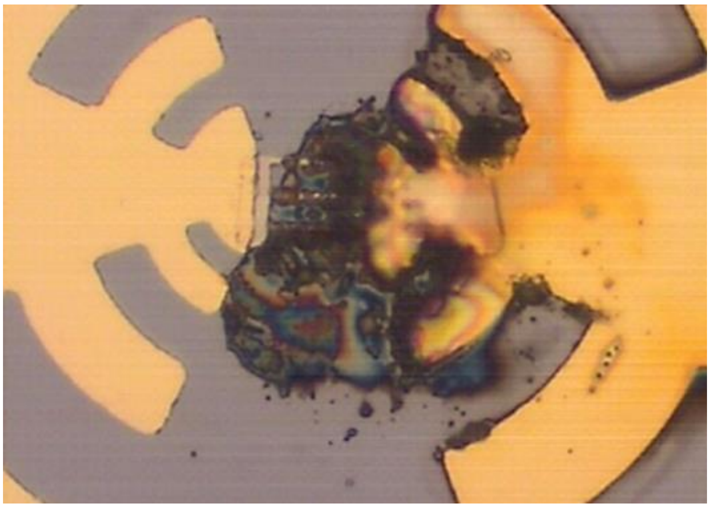

FIGURE 2.8: Thermal failure of the interdigital photomixer [22].

photoconductive material is transformed into heat, which forms a thermal load that will increase the temperature in the small active area of the THz device, as shown in Figure 2.8. Furthermore, the maximum handling photocurrent before the device failed is affected by the high temperature of the device, limits the THz output power of the device [33, 42].

The electromigration failures combined with thermal failures result in a catastrophic failure of the device as shown in Figure 2.9. The electromigration failure is correlated to thermal failure, where the atomic motion is supported by the heat generation, which leads to faster electromigration failure in the device.

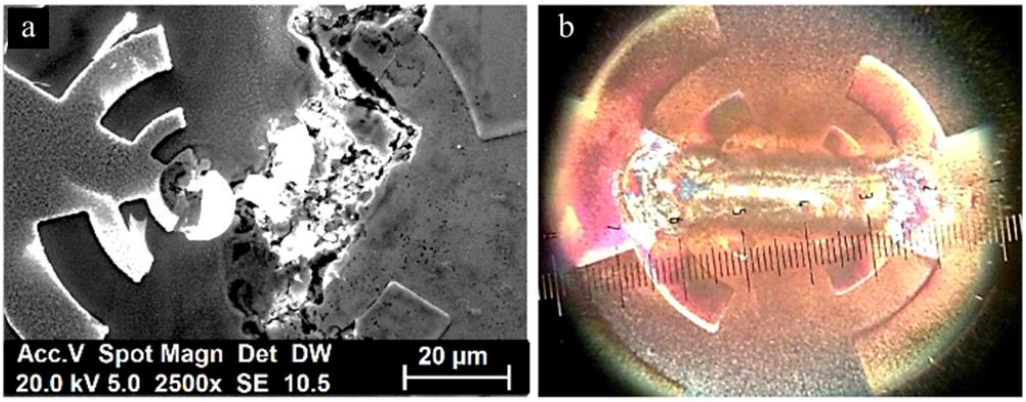

FIGURE 2.9: Combination of electromigration and thermal failures of the interdigital photomixer [22].

2.4.3 High-field Breakdown Failure

A DC bias field is required between the two electrodes of a THz photomixer emitter to accelerate the generated photocarriers of the modulated photoconductance. The generated photocurrent is proportional to the applied electric field, where the higher the electric field the higher the photocurrent, the higher the THz output power. However, it is a trade-off between increasing the applied electric field to obtain a higher generated photocurrent or increasing the applied electric field to increase the temperature of the device, causing a thermal failure in the device [28].

Chapter 3

Graphene

Chapter 3 discussed conventional photomixer using interdigitated metal electrodes. The optical to electrical conversion efficiency is limited due to the electrodes' opaqueness, which reduces the output power. Moreover, the combination of optical power and electrical power causes heating in the small active area of the photomixer device, which causes device failure.

Device electrodes based on nanomaterial are one of the feasible solutions to enhance device performance. The optical and electrical properties of graphene were studied to improve the photomixer performance. The combination of high transparency and the high electrical and thermal conductivity of the graphene results in photomixers with higher generated photocurrent, higher output power, and increased device reliability as compared to conventional interdigitated photomixers. In the following, the physical and electrical properties of various graphene growth will be illustrated in this chapter.

3.1 Graphene Properties

Graphene was discovered by Geim and Novoselov experimentally in 2004 [43]. Since then, it has become one of the most attractive materials being investigated. Graphene is a single 2D layer of carbon atoms arranged in a hexagonal lattice (see Figure 3.1). It

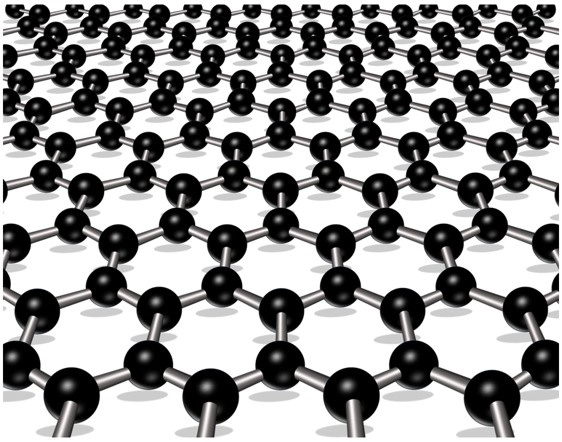

FIGURE 3.1: single-layer graphene

has many uncommon optical and electrical properties. In contrast to other transparent materials, such as indium tin oxide (ITO), the combination of high transparency and electrical conductivity makes graphene a very attractive material as transparent conductive electrodes, among many other potential applications. Moreover, graphene has a very high thermal conductivity that enhances lateral heat dissipation and improves device reliability.

3.1.1 Electronic Structure

Graphene is essentially a giant organic molecule and technically a semi-metal. When the electrons travel from one atom to the next, they follow the so-called pi-bonds that connect neighboring atoms. In contrast to metals (e.g., gold) where the electrons behave as if they were essentially free electrons (that is with a bare electron charge and mass), the interaction between the electrons in graphene occurs in the lattice in such a way that they appear to be massless [44]. This unique property provides graphene with its unique electronic properties.

Furthermore, multiple single-layer graphene sheets can be stacked and produce multilayer graphene. Therefore, typical graphene may comprise one layer to 10 layers of graphene, as shown in Figure 3.2. The variation in the number of graphene layers directly affects the sheet resistance and current-carrying capacity. On one hand, thinner graphene increased the transparency of the material, which allows almost all the light to propagate through graphene. On the other hand, a thicker graphene layer is required to carry reliable high current densities and to enhance the performance [45].

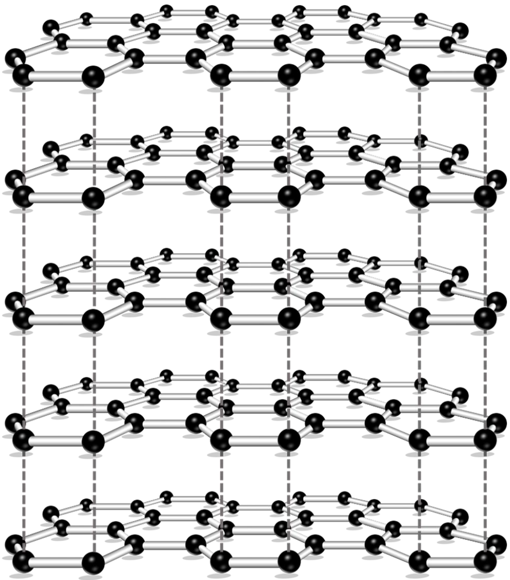

FIGURE 3.2: multilayer graphene

3.1.2 Electrical Conductivity

Graphene is an extremely desirable material to substitute the metal as an electrical conductor due to the unique gapless electronic structure and high intrinsic mobility of graphene. Graphene has remarkably high electron mobility at room temperature. It exceeds 2×10^5 cm^2/V·s [46] in suspended and annealed graphene devices. The graphene sheet resistance depends on the number of graphene layers. The thinner graphene the higher sheet resistance becomes. The average sheet resistance for single-layer graphene is 1150 Ω/sq. On the other hand, The average sheet resistance for seven-layers graphene is 220 Ω/sq [47]. Furthermore, graphene has reported having current densities on the order of 10^8 A/cm^2 for widths down to 16 nm [48].

3.1.3 Optical Properties

Graphene sheet has significant optical transparency for visible and infrared light. The optical transmittance of graphene is 95 - 97% depending on the number of the graphene layers [49]. This property allows almost all of the optical power to propagate through graphene. The increase of the optical power reaching the photoconductive material increase the number of generated photocarriers. The increase in the photocarriers density, which ultimately will accelerate by the bias field, results in increasing photocurrent and higher THz wave will be radiated.

3.1.4 Thermal Conductivity

The atomic structure of material influences the thermal conductivity of that material. The thermal conductivity becomes very important especially when the device dimensions decrease into nanometers. Where the combination of the optical power and the electrical power in the device causes heating [50]. Such heating can result in device thermal failure. Carbon forms (e.g. graphite, charcoal, and diamond) have a large variety of thermal conductivity. At room temperature, the lowest conductivity can be seen for amorphous carbon, which is about 0.01 W/mK. On the other hand, the diamond has a large conductivity of 2×10^3 W/mK [51].

Graphene has an extremely high thermal conductivity (about 5×10^3 W/mK at room temperature), which is 3 times higher than that of diamond [52–55]. Using graphene as nanoelectrodes for optoelectronic devices improves the lateral heat dissipation from the very small active area to the large antenna structure. By this, the stability of the device will increase. Furthermore, graphene has a reliable high-temperature operation [50, 56]. These advantages of graphene are the basis for a reliable high-power THz device.

3.2 Types of Graphene

Graphene purity, thickness, size, and other properties for specific needs can be defined by the processes of fabricating or extracting graphene. In recent years, various techniques were established to synthesis graphene. Mechanical cleaving (exfoliation) [43], chemical synthesis [57], chemical exfoliation [58, 59], and thermal chemical vapor deposition (CVD) [60] are the most commonly used techniques nowadays. However, there are many other methods are used to synthesis variant types of graphene. In general, graphene synthesis can be classified into two major categories, Top-down [61–64] and Bottom-up [65–76]. Each technique introduces some advantages and disadvantages to the quality of the graphene sheet. Two types of graphene were used in this work:

1. **Chemical vapor deposition (CVD)**

   Obtaining a large area, high quality, and transferable graphene until now is still a big challenge. CVD provides a good solution to produce large-scale graphene of high-quality [65, 78]. Where chemical decomposition of precursors such as methane on catalytic transition metal surfaces such as copper resulted in a single-layer or a few layers graphene [79, 80]. Transferring graphene sheets to

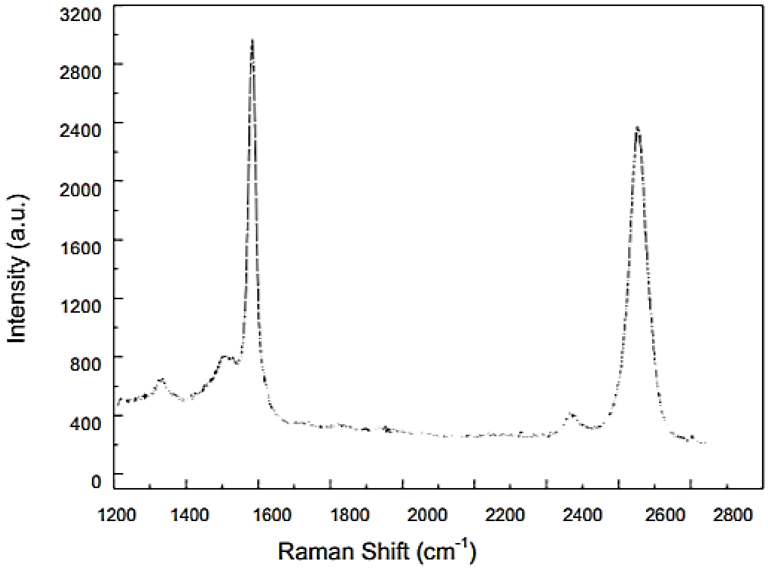

FIGURE 3.3: Raman spectra of ACS Material Trivial Transfer Graphene^{TM} (3-5 layers graphene) [77].

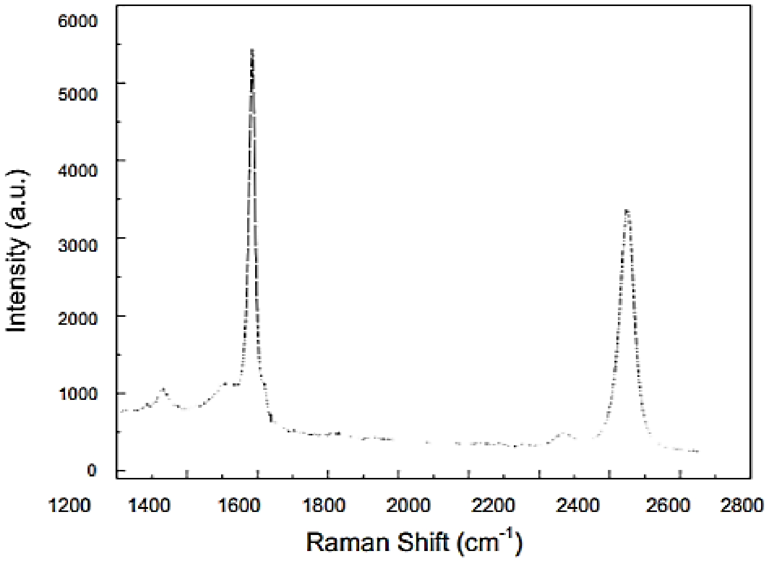

FIGURE 3.4: Raman spectra of ACS Material Trivial Transfer Graphene^{TM} (6-8 layers graphene) [77].

any other substrates is a very critical step. Poly-methyl-methacrylate (PMMA) is used as a support polymer to facilitate the transfer of graphene onto an alternate substrate. In this method, the synthesized graphene films laying on a copper substrate are coated with PMMA. The next step would be etching the copper substrate. Then, the coated graphene film is strong enough to be transferred to another substrate such as GaAs, Si, SiO_2, or glass without damaging the material. The advantage of using PMMA as a supporting layer is

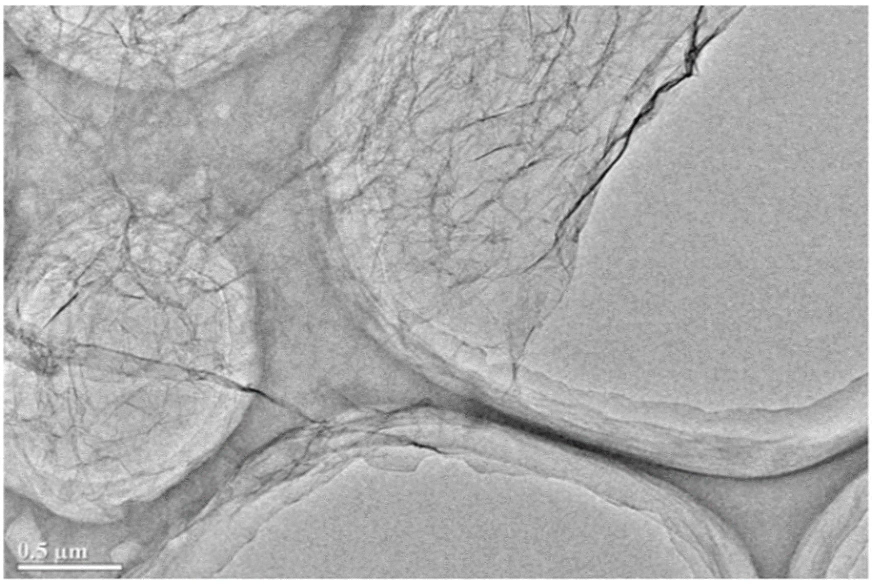

FIGURE 3.5: Typical TEM image of ACS Material N$^+$SLG [77].

that the PMMA can be easily dissolved by acetone without excessive damage [81].

Various industrial CVD graphene types (3-5, and 6-8 layer graphene) were purchased from ACS Material [77]. These types of graphene are provided as a homogeneous layer of a sheet resistance <600 Ω/sq and transparency >95%. The Raman spectra of ACS Material Trivial Transfer Graphene^{TM} of 3-5 layers graphene is shown in Figure 3.3 and the 6-8 layers graphene is shown in Figure 3.4 [77].

2. Nitrogen-doped Single-Layer Graphene Flakes (N$^+$SLG)

This type of graphene is prepared using the CVD method. The chemical composition of the N$^+$SLG flakes consists of Carbon ~ 88.0%, Nitrogen 1.0-3.0%, and Oxygen 7.0-7.5%. The flakes have a surface area of 500-700 m^2/g. The electrical conductivity of the flakes is >1000 S/m, which characterized at the density of 0.3 g/cm^3. The lateral size of the flakes is 05-5 μm [77]. The typical TEM image of ACS Material N$^+$SLG flakes is shown in Figure 3.5.

Chapter 4

Fabrications and Simulations

Enhanced THz photomixers are essentially required for many THz applications. Nanomaterials based on graphene are one of the main solutions to enhance the operational performance of photomixers. Conventional interdigitated photomixers based on metal electrodes were replaced by graphene nanoelectrodes in this work. In this chapter, graphene photomixers fabrication steps were discussed. The properties of graphene nanoelectrodes and metal electrodes were modeled and compared using various simulation software. The fabrication steps will be started with transferring graphene on top of the photoconductive material in section 4.1.

4.1 Graphene Trivial Transferring

The trivial transfer graphene technique was used to transfer the multilayer graphene sheet to other desired wafers. The purchased multilayer graphene (2.5 cm × 2.5 cm) is laid on top of a hydrophilic sponge substrate, and it is coated by a thin film of PMMA. By utilizing the wet transferring technique, a successful transferring of the graphene onto another substrate can be done by five simple steps:

The first step

> Few drops of deionized water were floated at the edge of the hydrophilic sponge substrate. After a while, the water drops will be absorbed by the sponge substrate. The absorbed water act as a separation layer between the multilayer

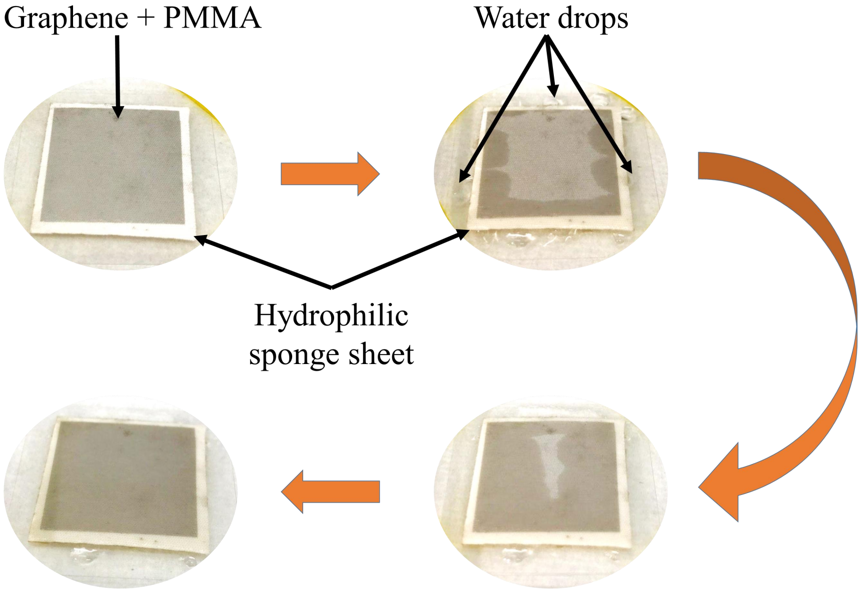

FIGURE 4.1: Graphene trivial transferring preparation.

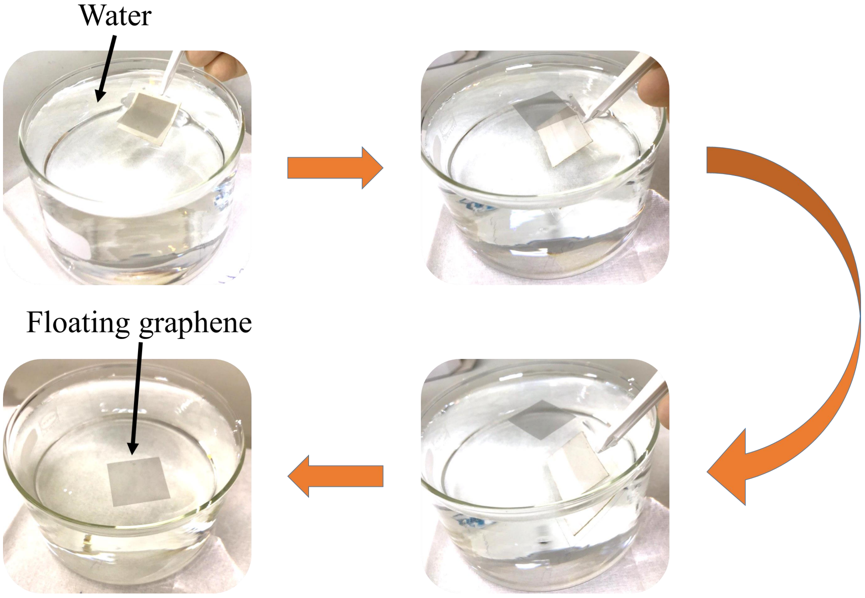

FIGURE 4.2: Floating graphene on the water surface.

graphene sheet and the sponge substrate. This step is necessary to maintain the homogeneity of the multilayer graphene sheet through the other transferring steps, as shown in Figure 4.1.

The second step

The sponge substrate with the floated multilayer graphene sheet was drowned nicely and easily in the deionized water. The multilayer graphene will float on the water surface, see Figure 4.2.

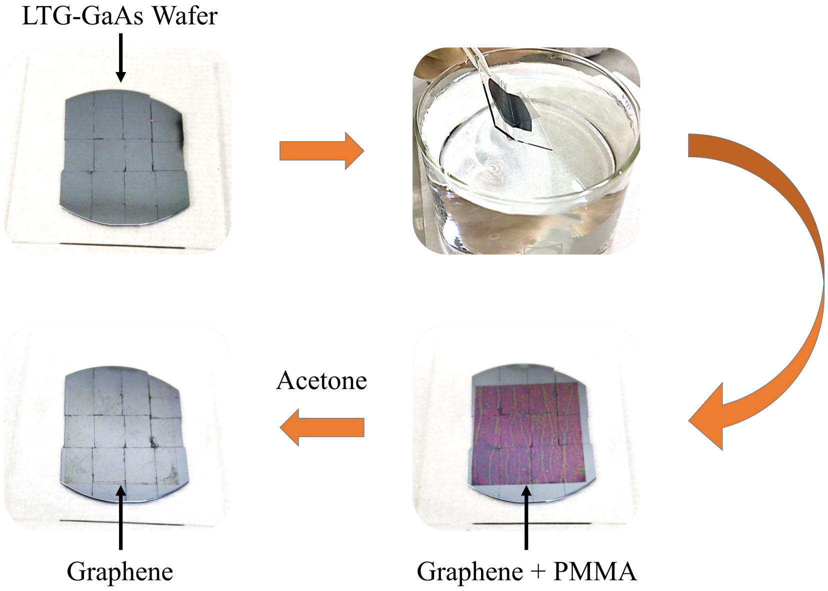

FIGURE 4.3: Trivial transfer graphene on LTG-GaAs.

The third step

An LTG-GaAs wafer was cut into small pieces. These pieces were aligned together on a class sheet using wax glue. The floated multilayer graphene sheet, which is coated with PMMA, is picking up from the water surface and transferred onto the surface of the collection of the LTG-GaAs wafer pieces, as shown in Figure 4.3.

The fourth step

The laid multilayer graphene with the PMMA layer on top of the LTG-GaAs has to be dry for further fabrication processes. Therefore, it should be kept safe until fully dried without any additional force. Heat treatment is strongly unrecommended because the water vapor will destroy the homogeneity of the graphene, which is under the PMMA layer.

The final step

The PMMA layer was removed using acetone, as shown in Figure 4.3. After the acetone cleaning, the placed multilayer graphene on LTG-GaAs is ready for further fabrication processes.

4.2 Graphene Devices Fabrication

Multilayer CVD-grown graphene was transferred onto LTG-GaAs substrates (thickness $\sim 350\ \mu$m), using the method mentioned in section 4.1. The fabrication of

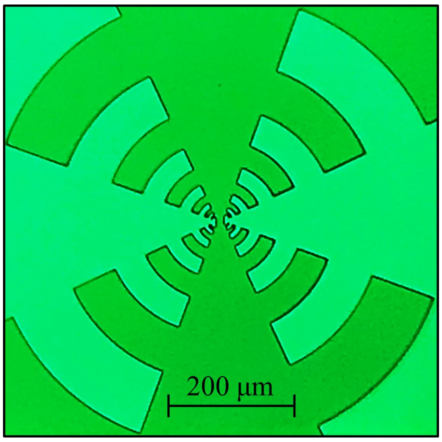

FIGURE 4.4: Microscopic image of the log-periodic antenna after the optical lithography process.

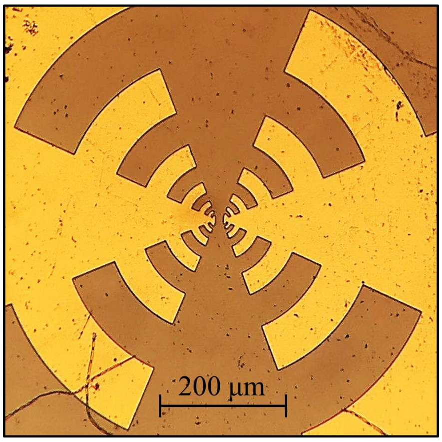

FIGURE 4.5: Microscopic image of the log-periodic antenna after the evaporation and lift-off process.

the photomixer with nanoelectrodes was performed by applying four steps of the standard optical lithography process.

The first step is to form the desired log-periodic antenna [25]. A broadband log-periodic antenna was designed using the dimension ratio of tooth/anti-tooth = 0.707, the ratio of the radial sizes of successive teeth = 0.5. The fabrication was started with flowed few drops of photoresist (AZ1518) on top of multilayer graphene. Using a spin coater (spin speed 4000 c/min for 40 s), a hot plate (under 90° for 90 s), and a standard lithography process, the photoresist liquid became a homogeneous layer with a thickness of 1.8 μm, as shown in Figure 4.4. Afterward, Ni (25 nm) / Au (150 nm) was evaporated to form the metallic form of the log-periodic antenna. Nickel is used for better adhesion to graphene. A lift-off process is necessary to remove the Ni and Au materials from the undesirable area, as shown in Figure 4.5.

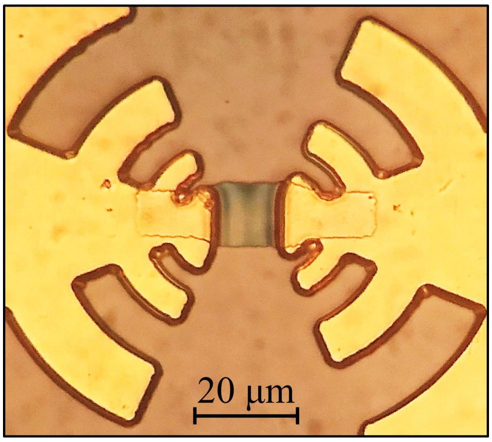

FIGURE 4.6: Microscopic image of the log-periodic antenna with a covered active area.

The second step is to keep the graphene only between the antenna contacts; few drops of a thin photoresist (AZ1505) have flowed on the top of the chip. The spin coater (spin speed 5000 c/min for 40 s for 40 s), a hot plate (under 90° for 90 s), and a standard lithography process were used again to create a homogeneous layer of photoresist with a thickness of 500 nm. The area between the antenna contacts was reserved by aligning a cap mask on the desired area, see Figure 4.6. The chip then was located inside the chamber of a plasma machine. An O_2 gas was used to blow the uncovered graphene material located on the unwanted area.

The third step is to form the nanoelectrodes of the photomixer; few drops of the thin photoresist (AZ1505) have flowed on the top of the chip again. The spin coater, a hot plate, and a standard lithography process were used same as in the second step to creating again a homogeneous layer of photoresist. A mask with an opened line with 1 μm width was aligned between the antenna contacts, see Figure 4.7. Finally, the graphene, which located in the opened line in the active area of the photomixer, was removed by blowing O_2 gas inside the plasma machine chamber.

The final step was performed to isolate the graphene layers from the environmental contamination. This will improve the current density of the device. Therefore, the photomixers were encapsulated by 150 nm SiNx.

For the interdigitated graphene nanoelectrodes, the second and third steps can be replaced by one optical lithography process step to form the interdigitated configuration, as shown in Figure 4.8.

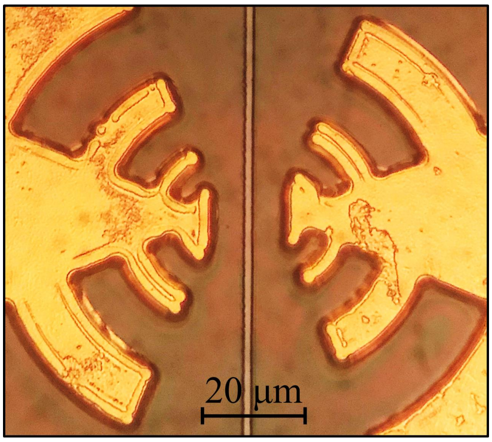

FIGURE 4.7: Microscopic image of the log-periodic antenna with a 1 μm gap in the active area.

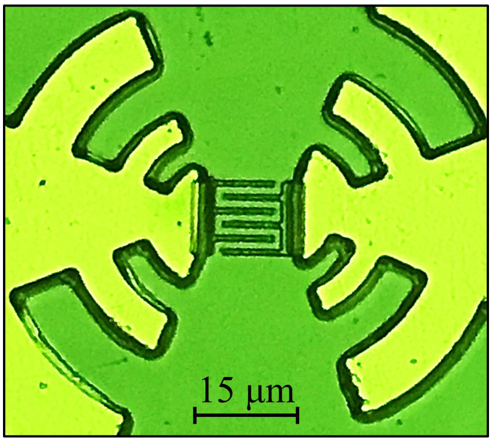

FIGURE 4.8: Microscopic image of the log-periodic antenna with interdigitated configuration after the optical lithography process.

4.3 Raman Characterization of Graphene

Due to the high transparency of graphene, it is impossible to identify the number of graphene layers via optical microscopes on substrates. Atomic force microscopy (AFM) [82, 83], transmission electron microscopy (TEM) [84, 85], X-ray diffraction (XRD) [86], Rayleigh scattering (RS) [87], and Raman spectroscopy [88] are the most common techniques used to identified and characterized the graphene layers on a substrate. In contrast to AFM, TEM, XRD, and RS, Raman spectroscopy provide an identification technique with high accuracy, fast, low cost, and sensitivity to the number of layers [87, 89]. With Raman spectroscopy, a laser source in the visible, near-infrared, or near ultraviolet range illuminates the graphene sheet. The scattered light would have a different frequency than the incident light frequency. The scattering intensity as a function of the frequency shifts will identify the number of graphene

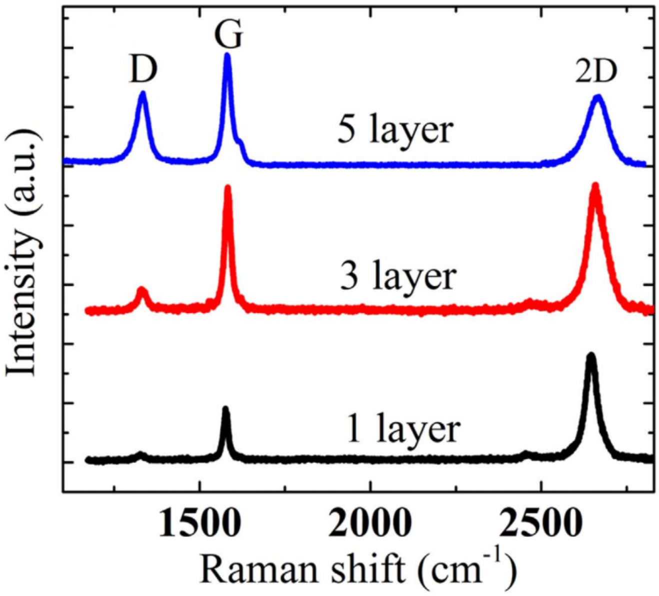

FIGURE 4.9: Raman output of graphene layers with different thicknesses [90].

layers.

Three significant bands must be taken into consideration in analyzing the Raman results of a graphene layer. The D band, the G band, and the 2D band, as shown in Figure 4.9.

1. The D band

The D band is known as the disorder band or the defect band and it represents a ring breathing mode from sp^2 carbon rings. The intensity of the D band is inversely proportional to the quality of graphene layers. The high-intensity peak can also appear at the edges of graphene layers [88, 91].

2. The G band

A sharp band that appears around 1587 cm^{-1} in the Raman shift spectrum is known as the G band. The intensity G band and its position indicate the graphene number of layers. The G band shifts downwards in the position as the number of graphene layers increased, while the intensity increase for the higher number of graphene layers [88, 91, 92].

3. The 2D band

The last important band is the second order of the D band known as the 2D band. The 2D band appears as a result of a two phonon lattice vibrational process and it does not represent defects or edges of graphene, as in the D band. Therefore, the 2D band is always appearing as a strong band in graphene even for very high-quality graphene. The thickness of graphene sheets can also be determined by the 2D band shape and the position of the band. For single-layer graphene, the 2D band is shown as a single symmetrical peak with a narrow full-width-half maximum. On the other hand, the band shape appears as a waveform of several peaks [88, 91, 92].

4.4 The Measurement Setup

In this work, a fiber setup was used for the characterization of the photomixers. Two tunable distributed feedback laser diodes (DFB-LDs) (wavelength ~ 850 nm) were coupled by a 50 : 50 combiner to generate the beat signal with a frequency corresponding to the frequency difference between the two DFP-LDs. Afterward, the beat signal was coupled into a cleaved polarization-maintaining optical fiber. The use of polarization-maintaining fiber is to stabilize the operation during the measurement. The end of the fiber was aligned close to the chip surface, in the range of a few μm, to fully illuminate the electrodes in the active area by the optical beat signal. Carriers will be generated in the photoconductive material between the electrodes due to the illumination of the beat signal. A DC power supply was implemented to accelerate the photogenerated carriers. The accelerated carriers will be radiated by the antenna as THz waves into the photoconductive material. The photomixer chip was mounted on a hemispherical Si lens. The Si lens was used to couple and direct the THz radiation into two parabolic mirrors. The parabolic mirrors are also used to direct the THz beam onto a Golay cell (Tydex GC-1P) as shown in Figure 4.10. The incident THz power onto the Golay cell would be converted into an electrical signal. The conversion of the THz output power into an electric signal is defined as the detector responsivity R. The responsivity measures the electrical output (V_{det}) per optical input (P_{THz}). The responsivity of a Golay cell is usually expressed in units of volts per watt of incident radiant power at a certain chopping frequency [93]

$$R(f) = \frac{V_{det}}{P_{THz}} \tag{4.1}$$

The electrical output signal of the Golay cell feeds a lock-in amplifier to measure the amplitude of the signal in terms of voltage. The measured amplitude of the voltage signal is proportional to the intensity of the THz output power. For the lock-in measurement, the DC bias was modulated by 20Hz. The measurement range is determined by the optical beat frequency, which corresponds to the frequency

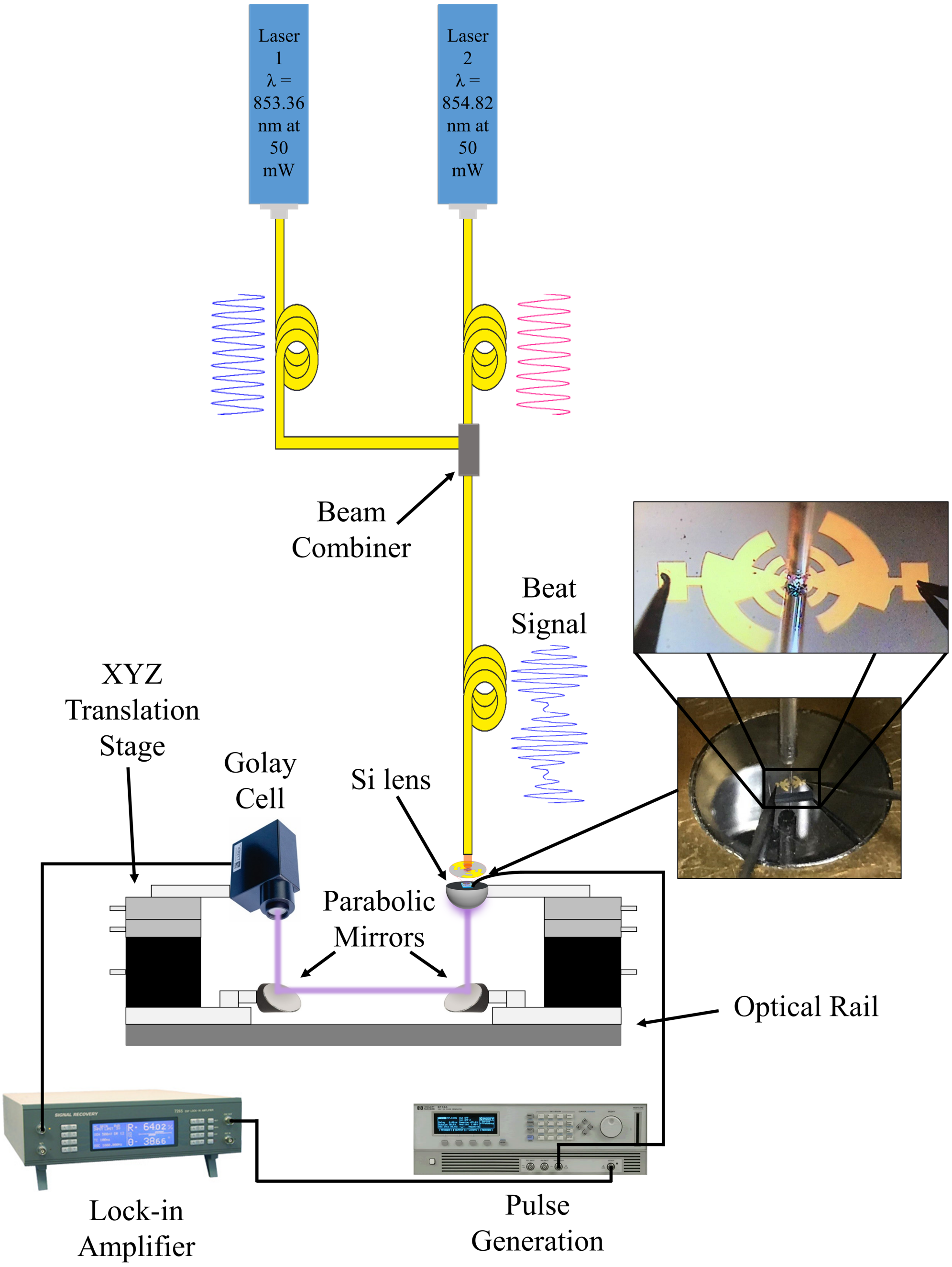

FIGURE 4.10: The Measurement Setup.

difference (Δf) between the two DFB-LDs. The Δf between the lasers is given by the following equations

$$\Delta f = f_1 - f_2 \tag{4.2}$$

$$\Delta f = \frac{c}{\lambda_1} - \frac{c}{\lambda_2} \tag{4.3}$$

$$\Delta f = \frac{c\,(\lambda_2 - \lambda_1)}{\lambda_1 - \lambda_2} \tag{4.4}$$

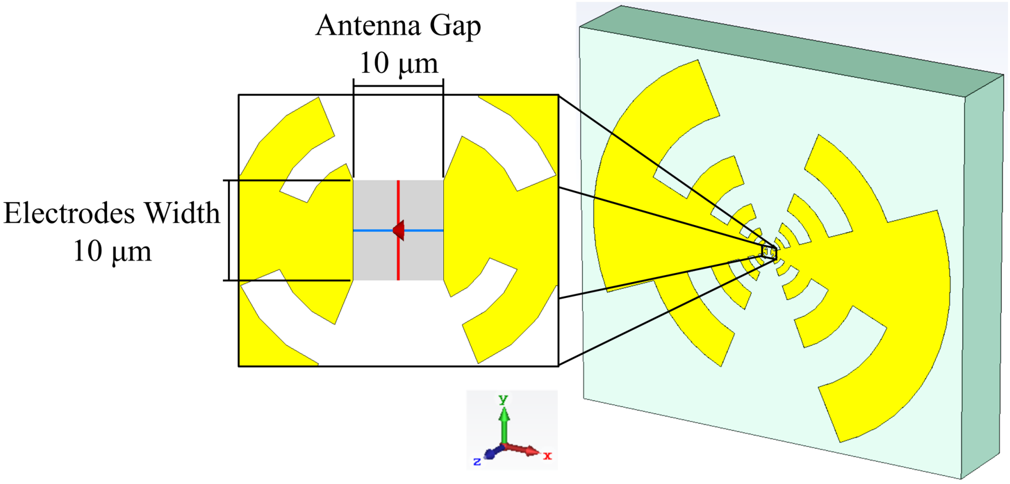

FIGURE 4.11: Layout of the construction of a log-periodic antenna with active area of 10 × 10 μm^2.

$$\Delta f = \frac{c\Delta\lambda}{\lambda_1 - \lambda_2} \tag{4.5}$$

where $\lambda_{1,2}$ are the wavelength of the two DFB-LDs. The optical beat frequency, and consequently, the THz measurement range is defined by determining λ_1, λ_2, and $\Delta\lambda$ of the two DFB-LDs.

4.5 Device Simulations

4.5.1 Antenna Design

The antenna design determines the bandwidth, directivity, tuneability, gain, and efficiency of the radiation. The upper cutoff frequency of an antenna is limited by the size of the active area between the photomixer contacts. Reducing the active area of the photomixer allows the device to extend the operating frequency range. The broadband log-periodic antenna was simulated using the 3D field simulation program CST Microwave Studio® based on Finite Integration Technique (FIT). The same antenna dimensions in section 4.2 were used for the simulation. The various gap widths between the antenna contacts (10 μm and 5 μm) were designed. These dimensions make the active area between the antenna contacts 10 × 10 μm^2 and 5 × 5 μm^2 [25]. The CST software was used to determine the characteristic of the designed antenna. The antenna characteristic is changed due to the configuration of the antenna. In this approach, reducing the distance between the antenna contacts caused a change in the value of the reflection coefficient of the antenna and increases the radiated frequency range.

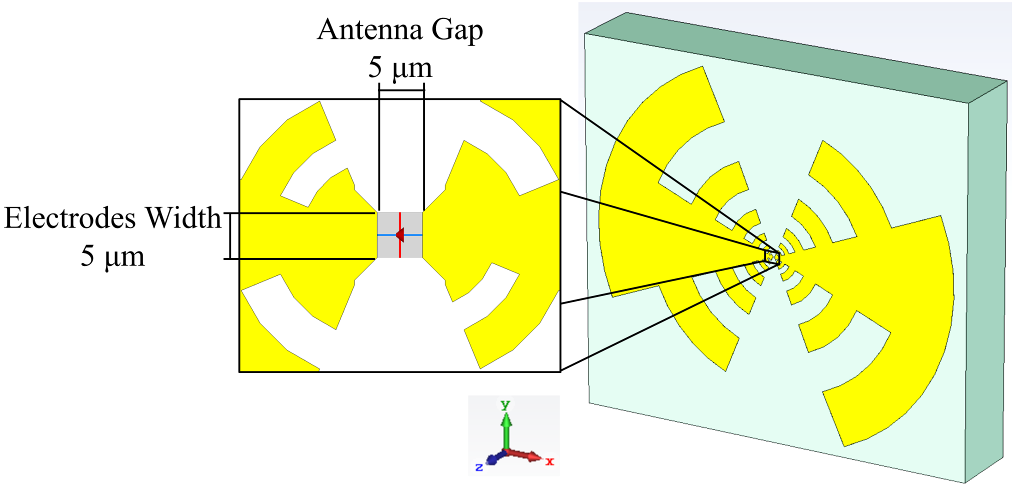

FIGURE 4.12: Layout of the construction of a log-periodic antenna with active area of 5 × 5 μm^2.

4.5.2 Nanoelectrodes Conductivity

The performance of graphene as a passive conductor was simulated using the CST Microwave Studio® based on FIT. Figures 4.13 and 4.14 illustrate the layout of the construction of a log-periodic antenna with gold and with graphene electrodes, respectively. In the design, the antenna (thickness is 150 nm) was located on top of a GaAs substrate (length 1100 μm, width 1000 μm, and thickness 200 μm). The electrodes were distributed in the active area with a length of 10 μm. The electrodes dimensions were 4.5 × 10 μm^2, and the gap separation between the electrodes was 1 μm. The thickness of the gold electrodes is modeled to be 150 nm. The thickness of the modeled graphene electrodes can be estimated from the thickness of the graphene sheet, where the estimated thickness for the multilayer graphene is $T_{MLG} = N T_{SLG}$, where N represents the number of layers and T_{SLG} is the thickness of single-layer graphene, $T_{SLG} = 0.335$ nm [94]. Therefore, to simulate the use of 6-8 layer graphene as electrodes, the thickness of the electrodes was chosen as 2.5 nm for graphene electrodes.

4.5.3 Graphene Transparency

The transparency of the electrodes plays a crucial role in increasing the number of generated photocarriers, which leads eventually to a higher generated photocurrent. In the infrared and visible light, gold electrodes reflect more than 95% of the incident light [95]. One of the main significant optical properties of graphene is transparency, where the optical transmittance of graphene is 95 - 97% depending on the number

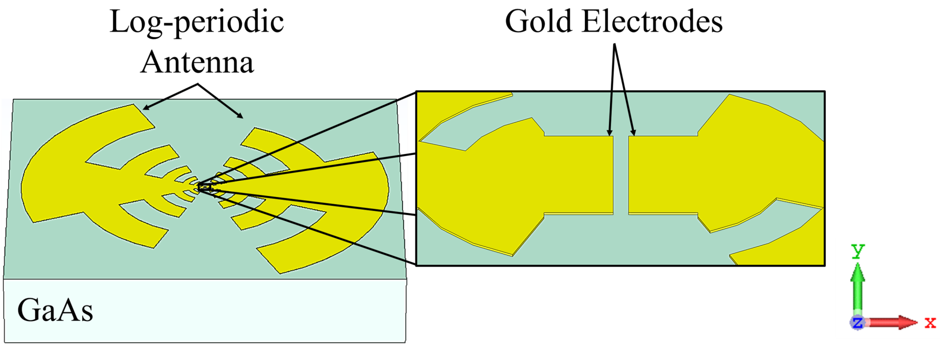

FIGURE 4.13: Layout of the construction of a log-periodic antenna with gold electrodes.

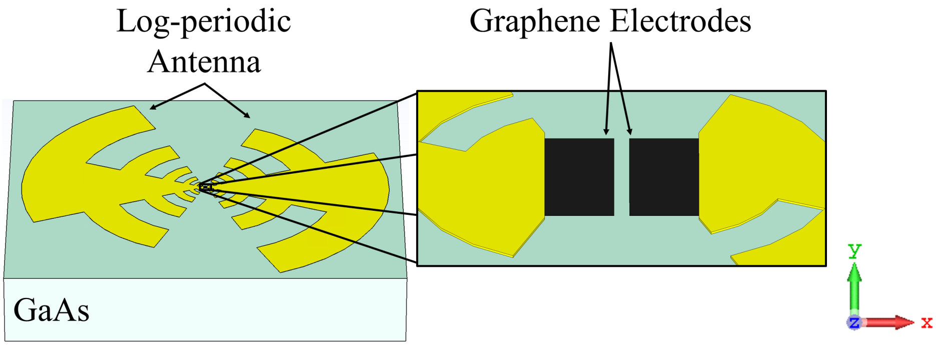

FIGURE 4.14: Layout of the construction of a log-periodic antenna with graphene nanoelectrodes.

of the graphene layers [49]. This property allows almost all of the optical power to propagate through graphene. The increase of the optical power reaching the photoconductive material increase the number of generated photocarriers. The increase in the photocarriers density, which ultimately will accelerate by the bias field, results in increasing photocurrent and higher THz power will be achieved. The use of transparent material as electrodes for optoelectronic devices increases the illuminated effective area, which leads to an increase in the photocarrier generation rate (G_r). The generation rate gives the number of generated photocarriers at each point in the photoconductive material due to the absorption of photons. The generation rate of photocarriers can be calculated at any location within the photoconductive material. Neglecting the reflected light from the surface, the amount of light that is absorbed by a material depends on the absorption coefficient (α in cm^{-1}) and the thickness of the absorbing material. The intensity of light at any point in the device can be calculated as

$$I = I_\circ \exp(-\alpha x) \tag{4.6}$$

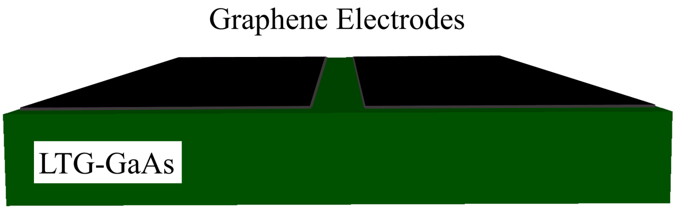

FIGURE 4.15: Layout of graphene nanoelectrodes.

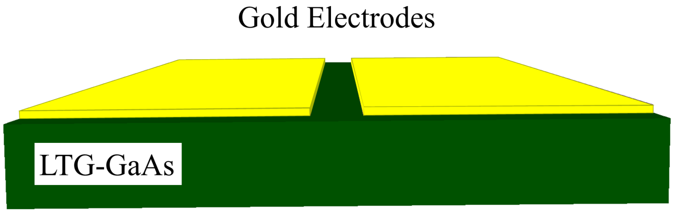

FIGURE 4.16: Layout of gold electrodes.

where $I_\circ$ s the light intensity at the top surface, and x is the distance into the photoconductive material at which the light intensity is being calculated.

Assuming that each photon absorbed generates directly an electron-hole pair, then the generation G_r at any point in the photoconductive material is determined by

$$G_r = \alpha N_\circ \exp(-\alpha x) \tag{4.7}$$

where $N_\circ$ is the photon flux at the surface (photons/cm^2.s). The above equations show that the light intensity exponentially decreases throughout the material and further that the generation is highest at the surface of the material.

From equations (2.8) and (2.11), the higher the photocarrier generation rate the higher the photocurrent can be generated.

The effect of the transparency of graphene was simulated using the Silvaco - Technology computer-aided design software (S-TCAD) based on the finite element method. The software was used to obtain the generation rate for optoelectronics devices using gold electrodes (the thickness is 150 nm) and 6-8 layer graphene nanoelectrodes (the thickness is 2.5 nm), respectively. Figure 4.15 and Figure 4.16 show the layout of graphene and gold electrodes, respectively. For both devices, the dimensions of the electrodes were 5.5 × 20 μm^2 and the gap separation was 1 μm.

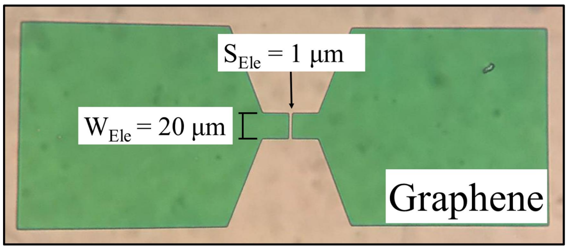

FIGURE 4.17: Transferred grpahene nanoelectrodes.

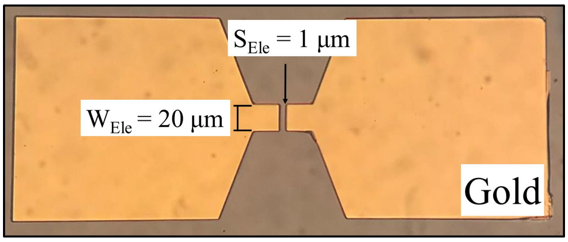

FIGURE 4.18: Gold electrodes.

The simulation was continuum experimentally by transferring graphene on top of LTG-GaAs and compared with gold electrodes. Figure 4.17 shows graphene pads using 6-8 layers graphene. The electrodes were formed between the pads using the standard optical lithography process, where the electrode width (W_{Ele}) was 20 μm and the gap separation between the electrodes (S_{Ele}) was 1 μm. Gold with the same dimensions was evaporated on top of LTG-GaAs as shown in Figure 4.18.

4.5.4 Device Capacitance Calculation

The device capacitance plays a very important role in the value of the device output power. Equation (2.17) shows that the low device capacitance results in higher THz output power, especially at the upper part of the THz range [22]. Various configurations of graphene nanoelectrodes were designed between the antenna contacts. The device capacitance was calculated mathematically and simulated using CST Electromagnetic Studio® based on FIT.

1. Interdigitated graphene nanoelectrodes

A 6-finger interdigital configuration was designed between 10 × 10 μm^2. The dimension of the finger width (W_f) was 0.5 μm, the spacing gap (S_g) between the fingers was 1.5 μm, and the finger length (L_f) was 9 μm, as shown in Figure 4.19. The capacitance of the interdigital-finger configuration can be calculated using the simplified conformal mapping technique [96, 97]

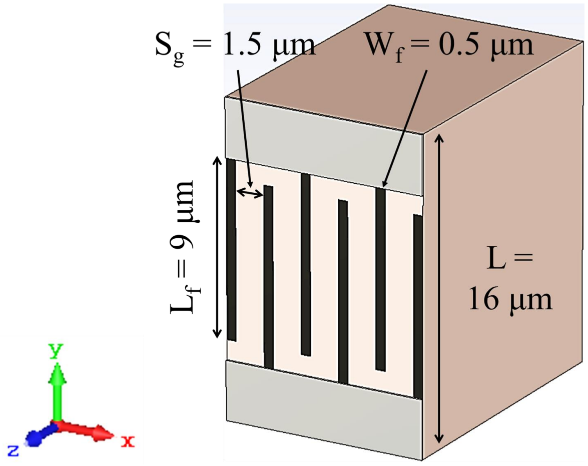

FIGURE 4.19: Interdigitated graphene nanoelectrodes.

$$C = \frac{K(k)}{K(k')}\frac{\varepsilon_0(1+\varepsilon_r)A_{act}}{w_g + w_e} \tag{4.8}$$

where ε_0 the absolute permittivity, $\varepsilon_r = 13$ is the relative permittivity of LTG-GaAs, A_{act} is the active area of the photomixer, S_g is the gap width, W_f the finger electrode width, and $K(k)$ is the complete elliptical integral of the first kind with:

$$k = \tan^2\left(\frac{\pi W_f}{4(S_g + W_f)}\right) \tag{4.9}$$

and

$$k' = \sqrt{1-k^2} \tag{4.10}$$

The approximation value of the elliptical integrals can be calculated from [98] with an acceptable relative error of 3×10^{-6} as given

$$\frac{K(k)}{K(k')} \approx \frac{1}{\pi}\cdot\ln\left(\frac{2(1+\sqrt{k})}{1-\sqrt{k}}\right) \tag{4.11}$$

$$\text{for} \quad 1 \leq \frac{K(k)}{K(k')} \leq \infty \quad \text{and} \quad \frac{1}{\sqrt{2}} \leq k \leq 1$$

$$\frac{K(k)}{K(k')} \approx \pi\cdot\ln\left(\frac{2(1+\sqrt{k'})}{1-\sqrt{k'}}\right)^{-1} \tag{4.12}$$

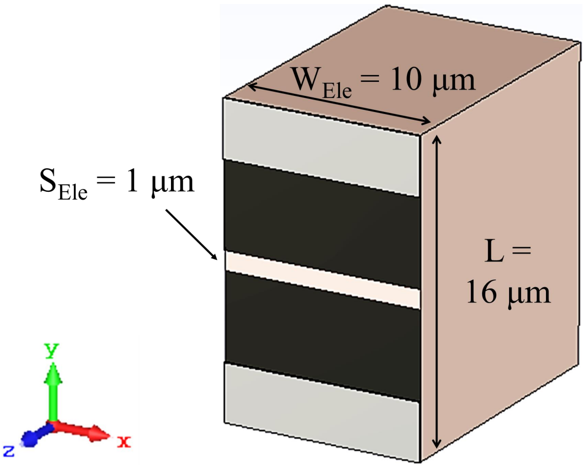

FIGURE 4.20: Graphene nanoelectrodes with 1 μm single gap and 10 μm width.

$$\text{for} \quad 0 \le \frac{K(k)}{K(k')} \le 1 \quad \text{and} \quad 0 \le k \le \frac{1}{\sqrt{2}}$$

2. Graphene nanoelectrodes with 1 μm single gap and 10 μm width

A single gap between the 2D graphene nanoelectrodes was illustrated in Figure 4.20. The active area between the antenna contacts was 10 × 10 μm^2. The capacitance value was calculated by applying the conformal mapping using the partial capacitance method as shown in equation (4.13).

$$C = \varepsilon_\circ W_{Ele}(\frac{2}{\pi} + \ln\frac{4L}{S_{Ele}} + (\frac{\varepsilon_r - 1}{\pi})\ln\frac{16H}{\pi S_{Ele}}) \tag{4.13}$$

where W_{Ele} is the physical electrode width, L is the physical electrode length, S_{Ele} is the gap between the electrodes, H is the physical thickness of the LTG-GaAs. The structure dimensions were $S_{Ele} = 1$ μm, $H = 350$ μm, W_{Ele} was 10 μm and L was 16 μm.

3. Graphene nanoelectrodes with 1 μm single gap and 5 μm width

Equation (2.17) shows that the output power of a photomixer is inversely proportional to the device capacitance. Reducing the contact width results in a reduction in the device's capacitance. The electrode width was reduced from 10 μm to 5 μm. The active area between the antenna contacts was 5 × 5 μm^2 as illustrated in Figure 4.21. Equation (4.13) was used to estimate the device capacitance using the Graphene nanoelectrodes with 1 μm single gap and 5 μm width.

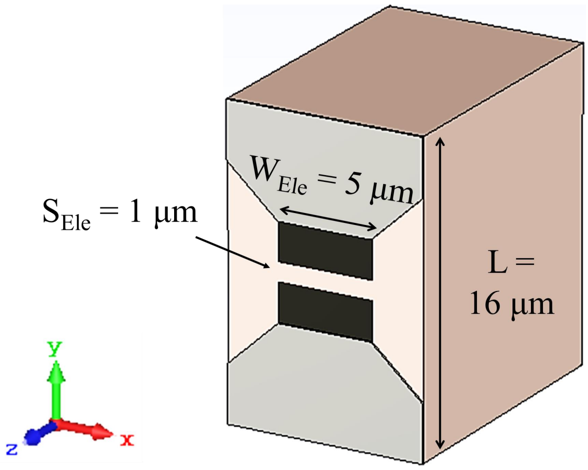

FIGURE 4.21: Graphene nanoelectrodes with 1 μm single gap and 5 μm width.

4.5.5 Electrodes Electrical Characteristic

Photocarriers are generated when an electromagnetic wave, such as a light source, incident upon a photoconductive material. The generated photocarriers will be contained within the photoconductive material. This will induce an electric field between the electrodes' fingers. The CST Microwave Studio® based on the FIT was used to simulate the produced electric field and the current density between the electrodes' fingers for various materials (gold and graphene). Moreover, the physical properties of the electrode material concerning the optical transparency were described by showing the power flow through the electrodes. A full plane wave as an electromagnetic source was applied from the side where the electrodes were located.

1. **Interdigitated gold electrodes**

   The same dimensions of the electrodes fingers used for the capacitance calculation were used in this simulation, as shown in Figure 4.22. A thickness of 150 nm was chosen for the gold electrodes. The electrode configuration was placed on top of the GaAs substrate.

2. **2D Graphene nanoelectrodes with 1 μm single gap**

   The same simulation was repeated using graphene nanoelectrodes. The geometry of the graphene nanoelectrodes with a single gap was illustrated in Figure 4.23. The dimensions of the graphene nanoelectrodes were $4.5 \times 10\ \mu m^2$. A gap of 1 μm separates the graphene nanoelectrodes from each other. A thickness of 2.5 nm was modeled for the nanoelectrodes to mimic the thickness of the 6-8 layer graphene.

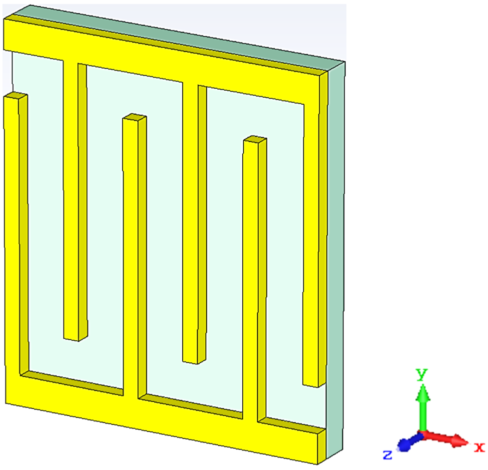

FIGURE 4.22: Interdigitated gold fingers.

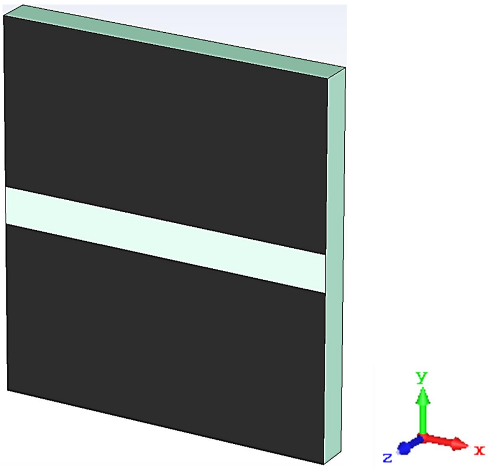

FIGURE 4.23: A single gap graphene nanoelectrodes.

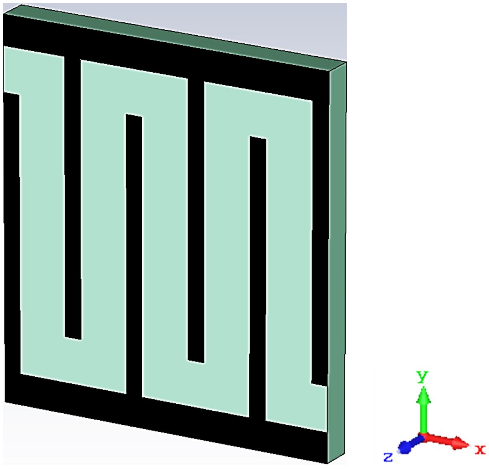

FIGURE 4.24: Interdigitated graphene nanoelectrodes.

3. Interdigitated graphene nanoelectrodes

The use of the interdigitated graphene nanoelectrodes combines the benefits of the transparency of graphene on one hand, and on the other hand, decreasing the transit time for the generated carriers from one electrode to another. Interdigitated graphene configuration was modeled using the same geometry as the interdigitated gold fingers, as shown in Figure 4.24.

Chapter 5

Graphene Based THz Emitter

Significant enhancement in the performance of the CW-THz photomixer emitters devices was aimed in this work. Two types (3-5, and 6-8 layers) of graphene material with various designs were used as nanoelectrodes. The benefit of using graphene nanoelectrodes instead of metal electrodes is to overcome the failure mechanisms of the conventional interdigitated photomixer [22]. Due to the high transparency of the graphene nanoelectrodes, an increase in the generated photocurrent will be obtained. Moreover, the high electrical and thermal conductivity of the graphene nanoelectrodes will provide a high capability for high generated photocurrent. This leads to an increase in the THz power in the upper part of the radiation frequency range.

5.1 Simulation Results

1. Antenna Design Results

Simulations were done to estimate the values of the reflection coefficient ($S_{1,1}$) over a radiation range between 100 GHz and 4 THz. In the software designs, two log-periodic antennas were compared using two different active areas ($10 \times 10\ \mu\text{m}^2$ to $5 \times 5\ \mu\text{m}^2$), as shown in Figure 4.11 and Figure 4.12. A discrete port was applied, to mimic the electrical field between the antenna contacts. The discrete port is mainly used to simulate lumped element sources inside the

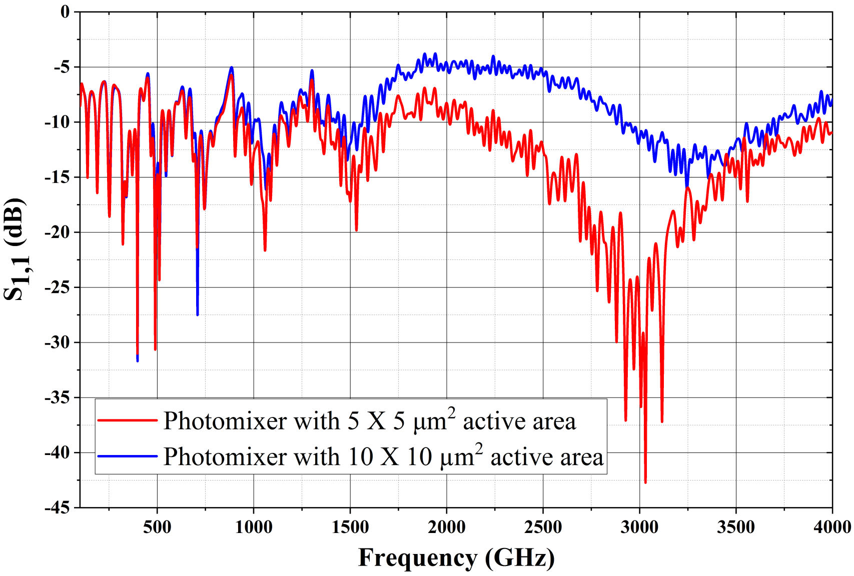

FIGURE 5.1: Comparison of the CST simulation results of the simulated $S_{1,1}$ for the photomixers with active area of 5 × 5 μm^2 and 10 × 10 μm^2.

calculation domain. The discrete port is a good approximation of the source in the feeding point of antennas to calculate the $S_{1,1}$.

Figure 5.1 shows simulated $S_{1,1}$ results over the frequency range from 100 GHz to 4 THz. The results can be divided into two regions.

I. The first region is started from 100 GHz up to 1.5 THz. Both photomixers showed a good agreement of the value of the reflection coefficient due to the same main design of the antenna.

II. The second region is started from 1.5 THz up to 4 THz, a significant reduction in the value of $S_{1,1}$ for the 5 × 5 μm^2 photomixer can be achieved. This reduction is because of the shorter distance between the antenna contacts. The total reflection coefficient of the 5 × 5 μm^2 photomixer ranges between -43 dB and -6.9 dB. The lowest value of $S_{1,1}$ (about -43 dB) was observed at 3.030 THz, which indicates that only 45 × 10^{-6} of the total delivered power will be reflected. In contrast, the 10 × 10 μm^2 photomixer exhibits higher $S_{1,1}$. The reflection coefficient of the 10 × 10 μm^2 photomixer ranges between -16 dB and -4.56 dB. This indicates that the total loss of the delivered power of the 10 × 10 μm^2 photomixer is higher than the total loss of the delivered power of the 5 × 5 μm^2 photomixer. Table 5.1 shows some $S_{1,1}$ values for some selected frequencies between 2 THz and 4 THz. This increases the operating frequency range of the THz photomixer, which allows fabricating a THz emitter with a high cut-off frequency of up to 4 THz.

TABLE 5.1: Comparison of the CST simulation results of the simulated $S_{1,1}$ for the photomixers with active area of 5 × 5 μm^2 and 10 × 10 μm^2.

Frequency (GHz)	**$S_{1,1}$ of 5×5 μm^2 (dB)**	**$S_{1,1}$ of 10×10 μm^2 (dB)**
2100	-11.039	-5.589
2300	-12.313	-5.541
2530	-17.452	-7.238
2700	-20.873	-7.873
2925	-37.229	-10.176
3000	-35.958	-10.947
3030	-43.479	-10.747
3280	-20.732	-12.49
3557	-17.255	-10.296
3800	-13.029	-8.499
3950	-11.808	-8.088
4000	-10.982	-7.909

2. Conductivity Results

Photomixers with gold and with graphene were simulated in section 4.5.2. A discrete port was used in the feeding point of antennas to calculate the $S_{1,1}$. Figure 5.2 shows the simulated results for the photomixers with gold and with graphene electrodes. For the simulation range from 100 GHz to 2 THz, the results show a generally good match between graphene and gold material in terms of the minimum value of $S_{1,1}$ for the photomixers. The electrical matching is due to the high conductivity and high mobility of the graphene sheet. This indicates that gold material can be replaced by graphene material as a very good conductor due to the high electrical conductivity of graphene.

3. Electrodes Transparency Results

A 25 mW optical signal was applied vertically to the center of the gap between the graphene and gold electrodes, as shown in Figure 5.3. A DC signal was applied to the electrodes. In the simulation, the DC signal was varied from 0 V to 40 V. It is very clear from Figures 5.4 and 5.5 that due to the opaqueness

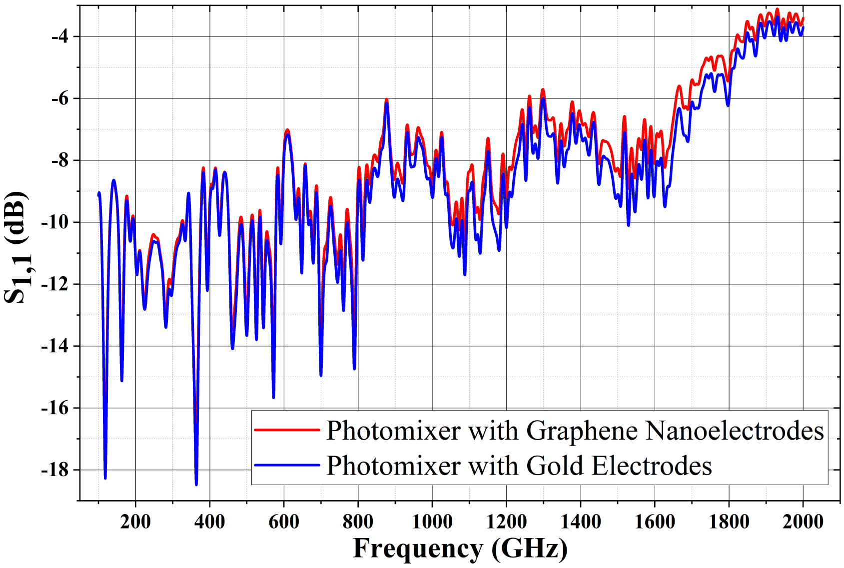

FIGURE 5.2: CST simulation results of the $S_{1,1}$ for the log-periodic antenna with PEC and graphene nanoelectrodes.

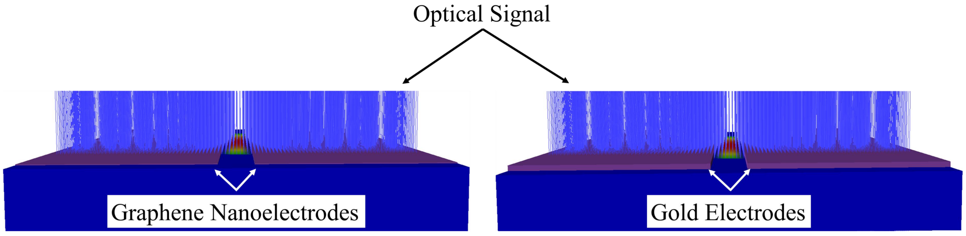

FIGURE 5.3: Silvaco TCAD simulation results of the photogeneration rate for the graphene nanoelectrodes.

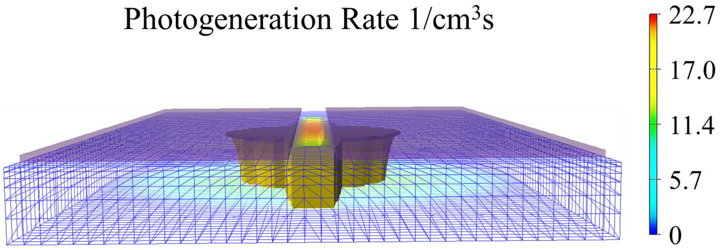

FIGURE 5.4: Silvaco TCAD simulation results of the photogeneration rate for the gold electrodes.

of the gold material the light beam cannot propagate through the electrodes. The beam of the photocarriers generation rate is confined in the gap between the contacts and very close to it because of the light diffraction in the material. On the other hand, the photogenerated rate for the device with multilayer graphene nanoelectrodes is much wider and it covers almost the entire illuminated area of the light beam. This indicates that a higher photocurrent can

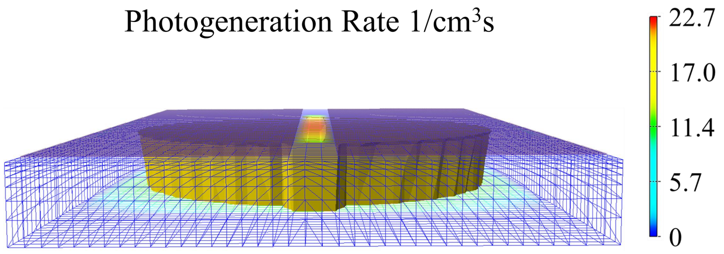

FIGURE 5.5: Silvaco TCAD simulation results of the photogeneration rate for the graphene nanoelectrodes.

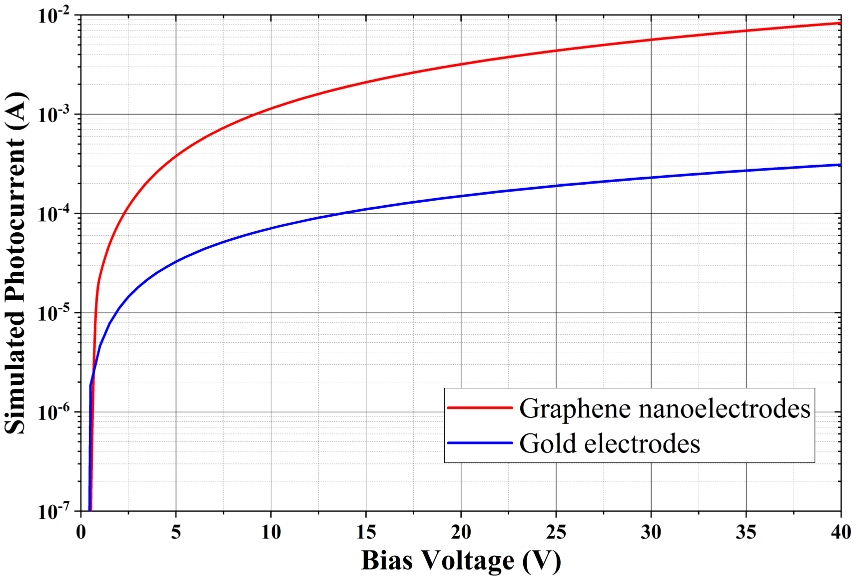

FIGURE 5.6: Comparison of the silvaco TCAD simulation results of the simulated photocurrent for the graphene and gold electrodes.

be generated. The wider the photocarriers generation beam the higher the number of carriers generated, the higher the generated photocurrent becomes. The simulation result showed that due to the transparency of the graphene nanoelectrodes, a higher photocurrent is generated as compared with the gold electrodes. Figure 5.6 shows the simulated photocurrent for devices with gold and with graphene electrodes using S-TCAD. The simulation proved that the graphene nanoelectrodes obtained more than one order of magnitude higher photocurrent than that of the gold electrodes over the whole bias measurement range.

The experimental DC Characterization was performed by applying a maximum optical power of 25 mW while the bias voltage was varied from 0 V to 40 V. The graphene nanoelectrodes show a maximum reliable photocurrent of $\sim$ 4 mA and an on/off ratio of more than four orders of magnitude due to the high

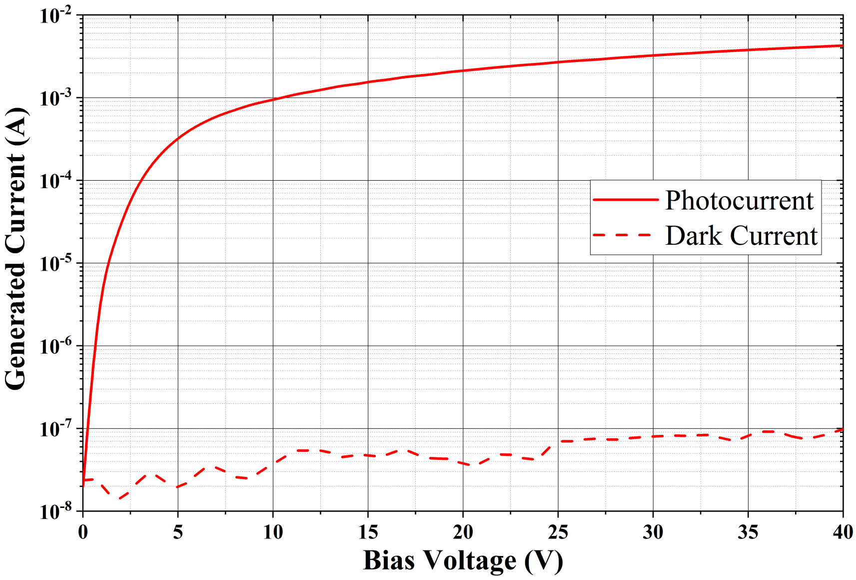

FIGURE 5.7: DC characterization of the graphene nanoelectrodes.

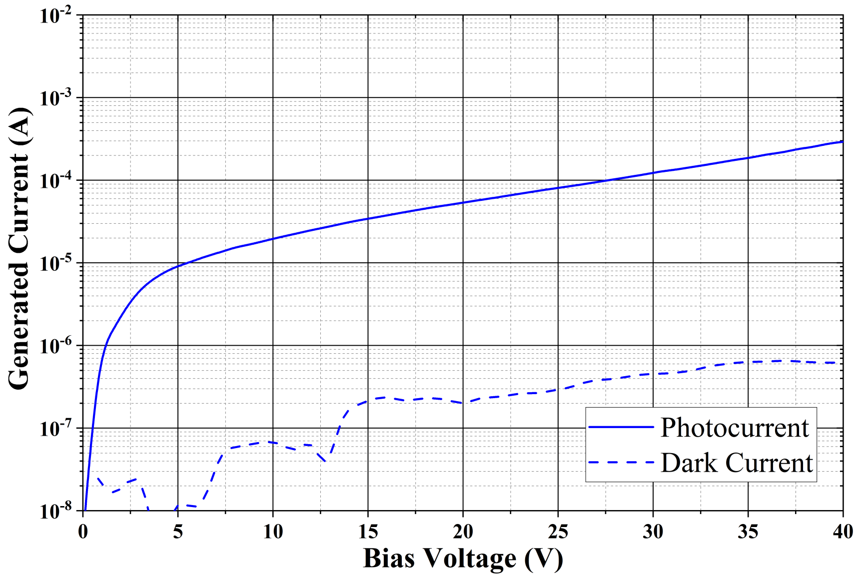

FIGURE 5.8: DC characterization of the gold electrodes.

transparency of graphene, as shown in Figure 5.7. The measurement results of the graphene pads were compared with gold pads. The same characterization conditions were applied for gold electrodes. The gold electrodes show lower photocurrent (~ 0.29 mA) and less on/off ratio (about 2 orders of magnitude) than graphene electrodes, as shown in Figure 5.8. Additionally, in contrast to graphene nanoelectrodes, the gold electrodes exhibit a higher dark current at high bias voltage than the graphene nanoelectrodes. This increase in the dark current increases the total generated current. Figure 5.9 shows a comparison of the generated photocurrent using graphene and gold electrodes. The

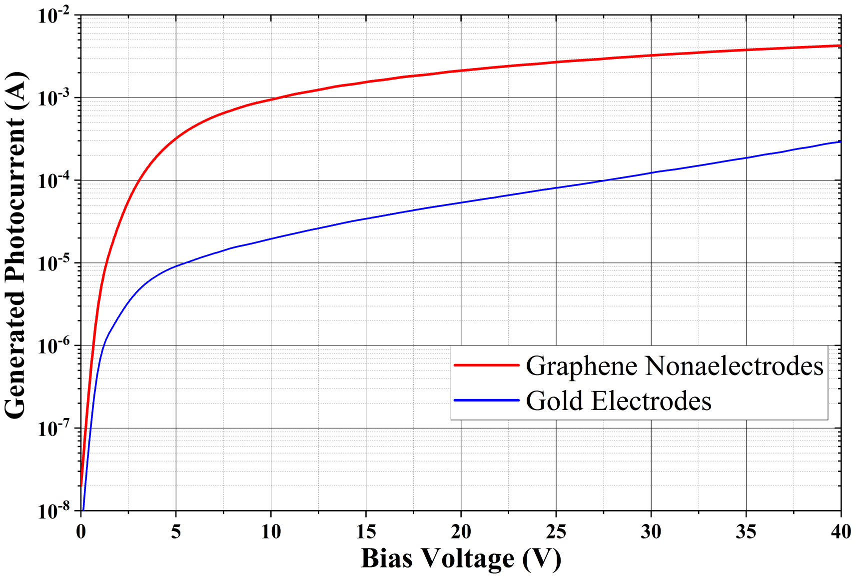

FIGURE 5.9: Comparison of the DC characterization of the graphene and gold electrodes.

graphene nanoelectrodes show 40 times at 20 V and about 13 times at 40 V of bias voltage higher photocurrent than what can be obtained by using gold electrodes. The reduction of the enhancement at high field is attributed to the higher dark current of the gold electrodes. It is worth mentioning that the DC measurements show generally a good agreement to simulation results with slightly lower overall values.

4. Device Capacitance Results

4.1. Interdigitated graphene nanoelectrodes

Due to the geometry of the interdigital 6-finger shown in Figure 4.19 and by using equations (4.9) and (4.10), $k = 1.1744 \times 10^{-5}$ and $k' \approx 1-k$. From the value of k and by using equation (4.12), the capacitance value for the interdigital graphene electrodes photomixer was calculated as 2.95 fF. This value is not far away from the simulation result ≈ 3.04 fF. The electrostatic solver of the CST software was used for the simulation and capacitance calculation.

4.2. Graphene nanoelectrodes with 1 μm single gap and 10 μm width

A single gap between the 2D graphene nanoelectrodes in 10×10 μm^2 active area was illustrated in Figure 4.20. By using equation (4.13), the total capacitance value was calculated as 2.95 fF. The simulation results confirmed the numerical calculation, where the CST simulation results showed a very close value of C ≈ 2.689 fF.

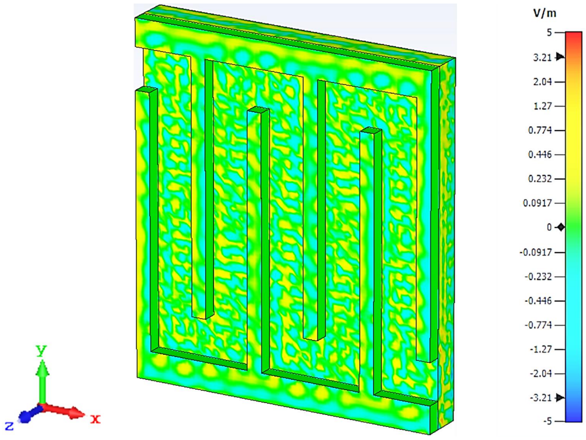

FIGURE 5.10: CST results of the electric field between the interdigital gold fingers.

4.3. Graphene nanoelectrodes with 1 μm single gap and 5 μm width

A single gap between the 2D graphene nanoelectrodes in 5×5 μm^2 active area was illustrated in Figure 4.21. The capacitance value was calculated by applying the same conformal mapping equation (equation (4.13)). The total capacitance value was calculated as 1.474 fF. The CST simulation results confirmed the numerical calculation, where the simulated C ≈ was 1.425 fF. This reduction in the device capacitance will result in higher output THz power.

5. Electrodes Electrical Characteristic Results

5.1. Interdigitated Gold Electrodes

The interdigitated electrodes configuration based on gold material is illustrated in Figure 4.22. The simulation results were shown that the generated electric field between gold fingers was 0.032 V/cm and the total current density was 0.169 A/cm^2. The distribution of the electric field between gold fingers shown in Figure 5.10. The opaqueness of gold electrodes limits the power flow from the wave source to the photoconductive material. The maximum power flow for gold electrodes was 4.2×10^{-6} V.A/cm^2. Figure 5.11 shows the optical power flow between the electrodes material along the X–axis of the medium.

5.2. 2D Graphene Nanoelectrodes with 1 μm single gap

Figure 4.23 shows 1 μm single gap between the 2D graphene nanoelectrodes. The electric field between the 2D configuration is the strongest, and it is decreasing further and further depending on the position where the photocarriers are generating far from the edges of the electrodes. Meanwhile, the transparency of the graphene sheet enhances the power flow and the optical to electrical conversion. The simulation results showed that the maximum

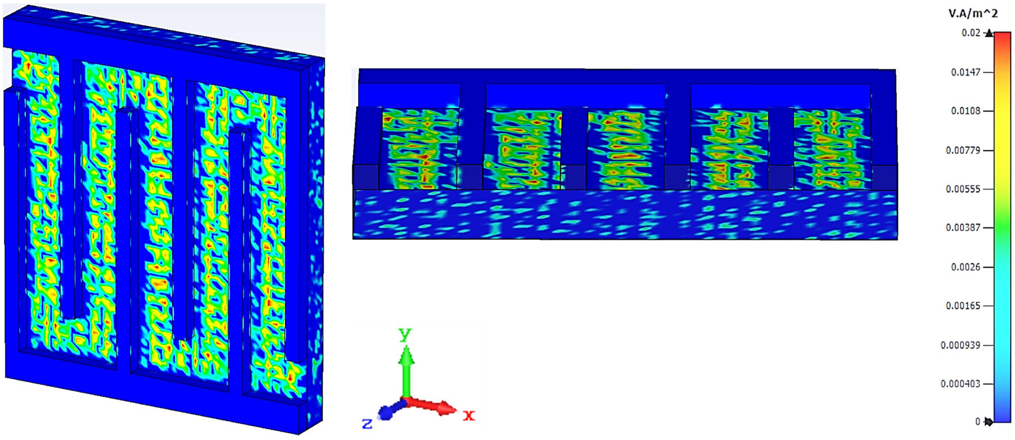

FIGURE 5.11: CST results of the power flow for the interdigital gold fingers.

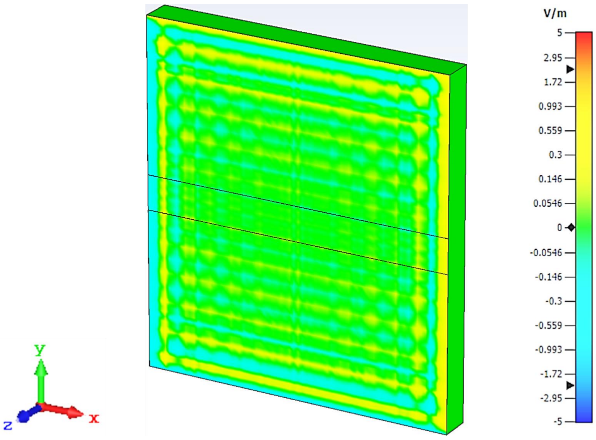

FIGURE 5.12: CST results of the electric field between the single gap graphene nanoelectrodes.

electric field between the nanoelectrodes of 0.022 V/cm was calculated. The electric field distribution between the 2D graphene nanoelectrodes shown in Figure 5.12. The effect of the transparency of the graphene sheet is shown by the increasing number of the generated photocarriers, which leads to higher current density. The maximum simulated current density was 0.735 A/cm^2, which is more than 4 times higher than that of the interdigitated gold electrodes. Furthermore, the simulation results of the single gap graphene nanoelectrodes showed a maximum power flow of 11.9 × 10^{-6} V.A/cm^2, which is about 3 times higher than that of the interdigitated gold electrodes.

5.3. Interdigitated Graphene Nanoelectrodes

Interdigitated graphene nanoelectrodes with the same geometry as the interdigitated gold finger were illustrated in Figure 4.24. The interdigitated graphene configuration combines the benefits of the transparency of the

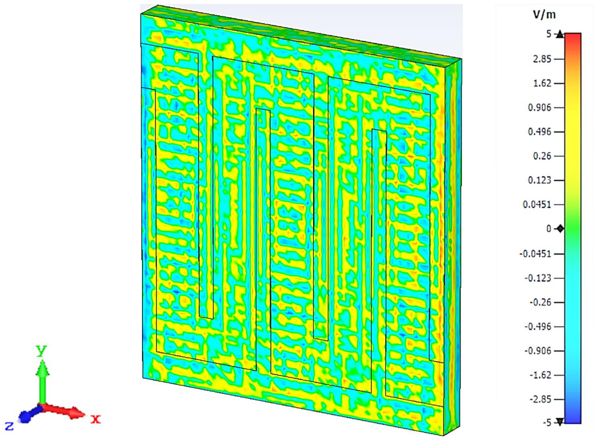

FIGURE 5.13: CST results of the electric field between graphene fingers.

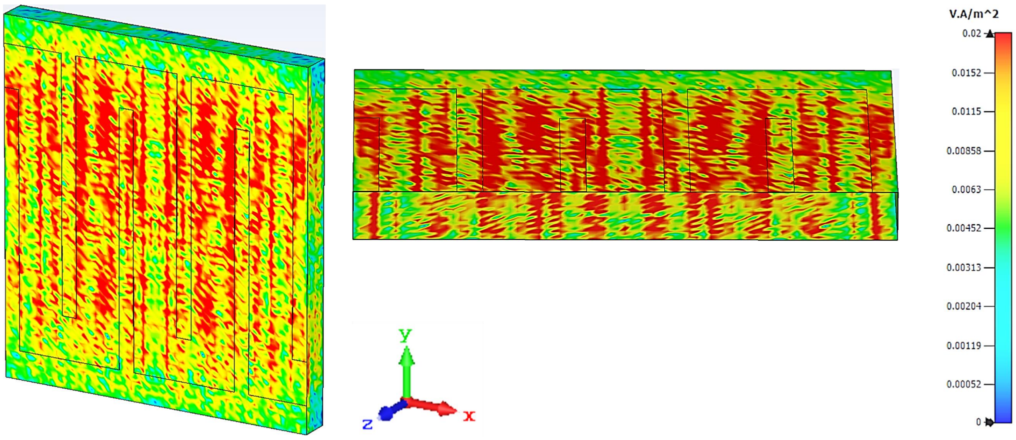

FIGURE 5.14: CST results of the power flow for the interdigital graphene fingers.

graphene and the reduced transit time for the generated photocarriers to travel from one electrode to another. The simulation results show that the generated electric field between the graphene fingers is about three times higher than that of interdigitated gold fingers. The interdigitated configuration exhibits a maximum electric field around 0.09 V/cm. Due to the transparency of the graphene sheet, which allows most of the wave beam to propagate and generates more carriers. The increase in the number of generated carriers results in a higher current density. The simulation results show that the maximum power of 11.5×10^{-6} V.A/cm^2 can flow for the interdigitated graphene nanoelectrodes, which is three times higher as compared with the power flow of the gold electrodes. Figure 5.14 shows the flowing of the power from the source of the wave to the photoconductive material. The high power flow leads to an increase in the current density of the material. The simulation results show that the maximum current density of 3.86 A/cm^2 can be generated.

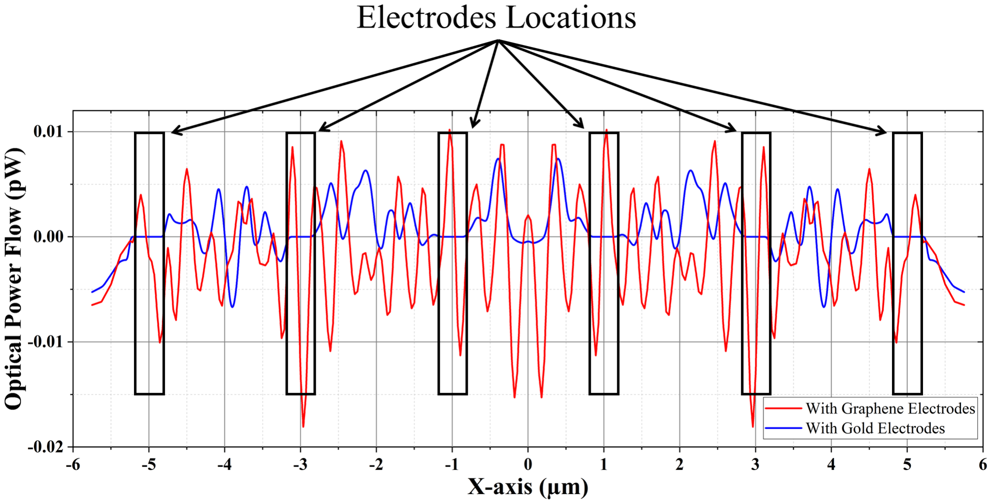

FIGURE 5.15: Comparison of the CST simulation results of the power flow of the interdigitated graphene and gold photomixers along the X–axis.

Figure 5.15 shows the standing wave of the optical power fluctuated between the photoconductive medium and the electrodes material for the interdigitated graphene and gold electrodes along the X–axis of the medium. Beneath the fingers, The gold electrodes show zero power because of the opaqueness of the gold material, which prevents the optical power to propagate through the electrodes. On the other hand, due to the transparency of graphene, higher optical power can be reached the photoconductive medium. This will increase the carrier density between and under the graphene electrodes.

6. Simulation Results Summary

Table 5.2 shows the summary of the CST simulation results for the various electrode configurations. Due to the high transparency of the graphene sheet, the optical power flow through graphene nanoelectrodes is higher as compared to the gold electrodes. The high power flow increases the current densities for the graphene nanoelectrodes. On the other hand, The interdigitated electrodes configuration provides a shorter transit time for the carriers because of the shorter transportation length between the fingers. This affects the value of the electric field between the electrodes' fingers. From table 5.2, interdigitated graphene nanoelectrodes exhibit the highest generated current density and the electric field between the fingers.

TABLE 5.2: The summary of the CST simulation results.

Electrodes configuration	**Capacitance**		**Electric field**	**Current density**	**Power flow**
	Calculated	**Simulated**			
Interdigitated gold electrodes	2.95 fF	3.04 fF	0.032 V/cm	0.169 A/cm^2	4.2×10^{-6} V.A/cm^2
Single gap graphene with 5 μm width	1.474 fF	1.425 fF	0.022 V/cm	0.735 A/cm^2	11.9×10^{-6} V.A/cm^2
Single gap graphene with 10 μm width	2.95 fF	2.689 fF			
Interdigitated graphene nanoelectrodes	2.95 fF	3.04 fF	0.09 V/cm	3.86 A/cm^2	11.5×10^{-6} V.A/cm^2

5.2 Measurement Results

The measurements are divided into two parts, the DC characterization and the THz output power measurements for the graphene nanoelectrodes photomixer. The measurements of the graphene photomixers are divided into three groups. The first group includes photomixers of single gap graphene nanoelectrodes with 5 μm and 10 μm width. The enhanced performance of the devices is attributed to the effect of the device's capacitance. The second group includes a comparison of interdigitated graphene photomixers with single gap graphene photomixers. The comparison shows the effect of the photoconductive gain of the photomixers. The third group shows the various graphene layers' effect on the performance of the device. The results were compared with conventional interdigitated photomixer.

5.2.1 DC Measurement Results

The relationship between the applied bias voltage and the generated photocurrent gives the first indication of the performance of the photomixer device.

1. Single gap graphene photomixers

Photomixers of an active area of 10×10 μm^2 and 5×5 μm^2 were fabricated. 6-8 layers graphene material with a single gap of 1 μm was performed as nanoelectrodes for these photomixers, as shown in Figure 5.16. The active area of the photomixers was illuminated with optical power, while the bias voltage was varied. The measurement results of the photomixers were compared

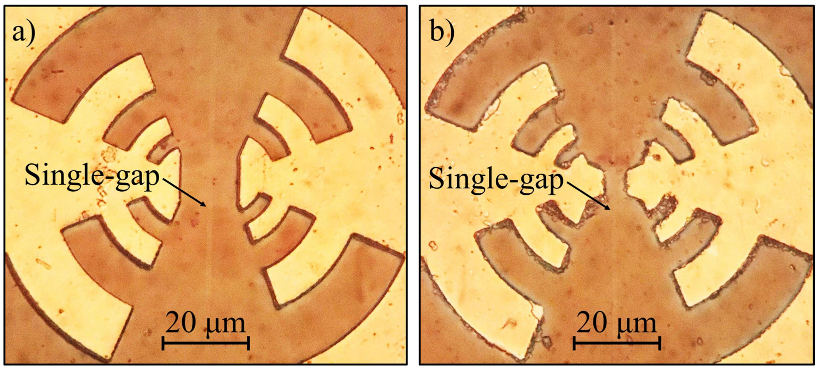

FIGURE 5.16: Microscopic image of the single gap graphene photomixersa with active area of: a) 10 × 10 μm^2, and b) 5 × 5 μm^2.

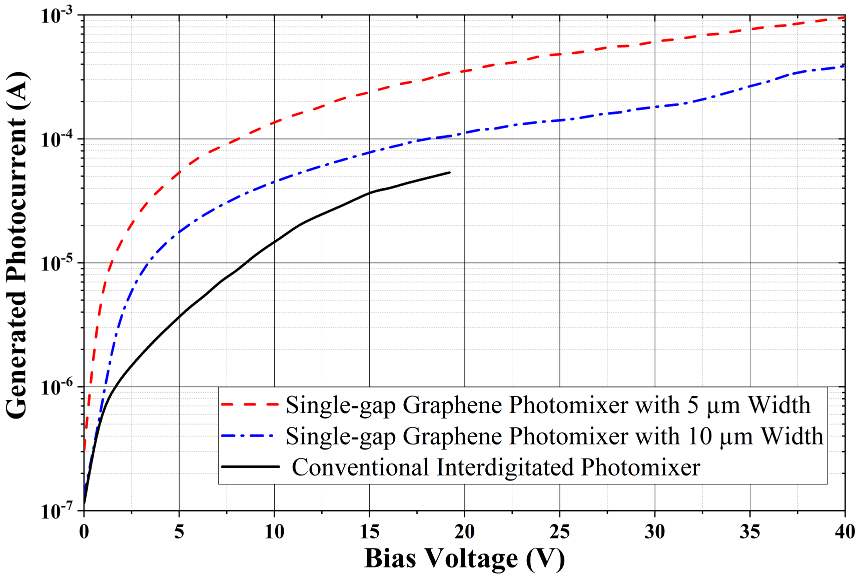

FIGURE 5.17: Comparison of the DC measurement results of the single gap graphene photomixer with 5 μm and 10 μm width and conventional interdigitated metal photomixer.

with the DC characterization of a conventional photomixer with interdigitated metal finger electrodes. The measurements were performed under the same conditions for all photomixers, where the active area of the photomixers was illuminated with a total optical power of 30 mW, while the bias voltage varied from 0 V to 40 V. The measurement showed that the conventional photomixer with interdigitated metal electrodes was damaged when a bias voltage reached $\sim$ 19 V due to the classical device failure in a small area as shown in Figure 5.17.

The photocurrent of the 10 μm photomixer is at least twice higher than the photocurrent of the conventional interdigitated photomixer. On the same approach, the 5 μm photomixer showed at least six times higher photocurrent than the conventional interdigitated photomixer. The increase in the

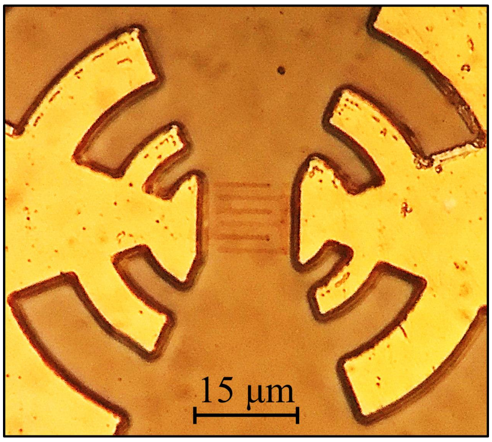

FIGURE 5.18: Microscopic image of the interdigitated 3-5 layers graphene photomixer.

photocurrent of the photomixers with multilayer graphene nanoelectrodes due to the transparency of the graphene allows most of the optical beat signal to propagate through the graphene and increase the number of the excited carriers which leads to the higher photocurrent. Additionally, due to less effect of the graphene by the ambient heat, the photomixers with multilayer graphene nanoelectrodes showed higher stability than the standard metal photomixer. This is represented by the durability of the photomixers with multilayer graphene nanoelectrodes at a high bias field (40 V).

2. Interdigitated 3-5 layers graphene photomixer

From equation (2.16), changing the configuration from single gap graphene nanoelectrodes to interdigitated fingers reduces the photocarriers' transport path length. Reducing the length of the optical transport path reduces the time required for the electron to reach from one electrode to another. In this approach, the benefit of using the high transparency of graphene will be combined the reducing the transit time for the electrons transporting between the two electrodes of the photoconductor with the increasing the number of the generated photocarriers due to the high transparency of graphene. The combined benefits result in a higher generated photocurrent and higher THz output power.

Figure 5.18 shows the interdigitated 3-5 layers graphene photomixer. The Raman characterization method was performed to confirm the number of the graphene layers and the existence of the graphene as nanoelectrodes in the active area of the photomixer. Figure 5.19 shows the Raman spectrum

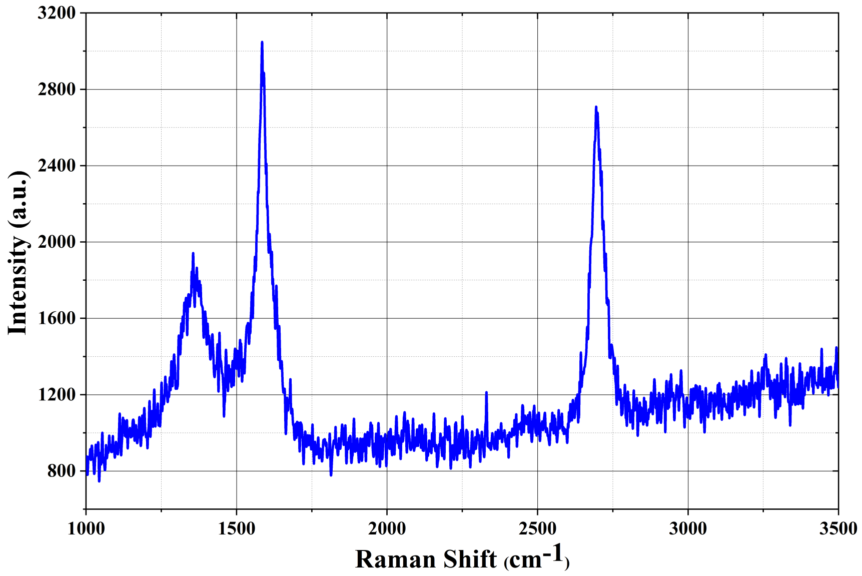

FIGURE 5.19: Raman spectra of the 3-5 layers graphene.

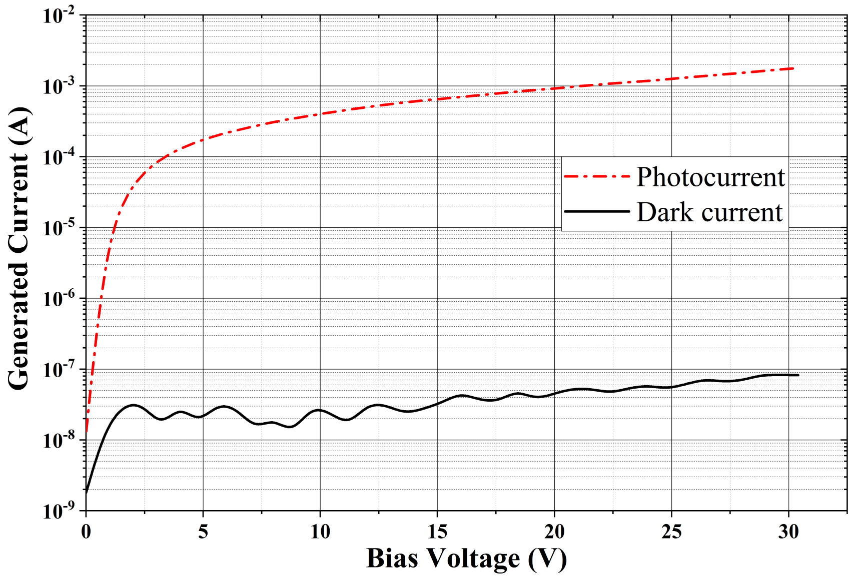

FIGURE 5.20: DC caharactrization of the interdigitated photomixer with 3-5 layers graphene.

of the graphene nanoelectrodes. The Raman characterization was taken at the Technical University of Darmstadt, Materials Science Department. The D band in Figure 5.19 is high due to the small size of the graphene fingers' width. The position and the amplitude of the G and 2D Band have a good agreement with the Raman spectrum of the 3-5 layers graphene shown in Figure 3.3.

The generated photocurrent of the photomixer with the interdigitated graphene nanoelectrodes was performed by applying a bias voltage. The bias voltage was varied from 0 V to 40 V. The total optical power of 30 mW the active area of

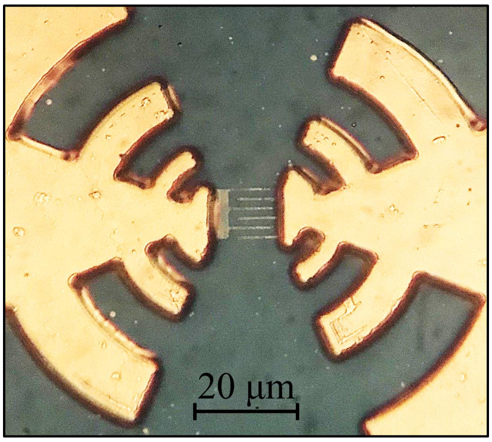

FIGURE 5.21: Microscopic image of the interdigitated 6-8 layers graphene photomixer.

$10 \times 10\ \mu m^2$ applied very close to the center of the nanoelectrodes, as shown in Figure 4.10. The maximum reliable generated photocurrent of 1.8 mA at 30 V was achieved before the high voltage damage the device. The dark current of the interdigitated 3-5 layers graphene photomixer was characterized using the same range of the bias voltage without illumination. The maximum generated dark current of 0.8 nA was reached. Due to the small dark current, an on/off ratio of more than four orders was achieved. Figure 5.20 shows the DC characterization of the interdigitated graphene photomixer.

3. Interdigitated 6-8 layers graphene photomixer

The variation in the number of graphene layers directly affects the sheet resistance and current capability. Higher transparency of thinner graphene increased the illuminated effective area to increase the number of generated carries. However, a thicker graphene layer is required to carry high current density and enhance performance and manufacturing reliability. Figure 5.21 shows the interdigitated 6-8 layers graphene photomixer. The number of the graphene layers and the existence of the graphene nanoelectrodes was confirmed using Raman spectroscopy. Figure 5.22 shows the Raman spectrum of the graphene nanoelectrodes. The D band in Figure 5.19 is high due to the small size of the graphene fingers' width. The position and the amplitude of the G and 2D Band have a good agreement with the Raman spectrum of the 6-8 layers graphene shown in Figure 3.4. The total optical power of 30 mW was illuminated the active area of the interdigitated 6-8 layers graphene photomixer. The DC characterization of the interdigitated 6-8 layers graphene

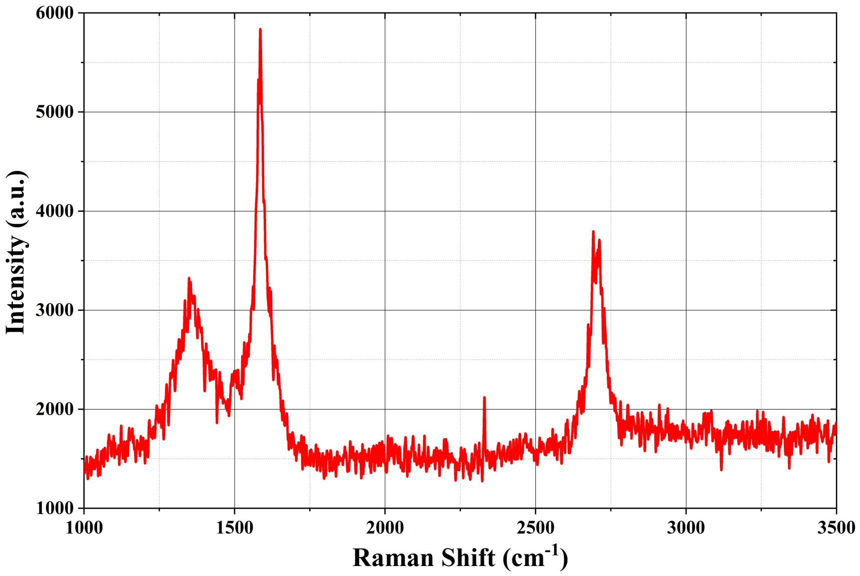

FIGURE 5.22: Raman spectra of the 6-8 layers graphene.

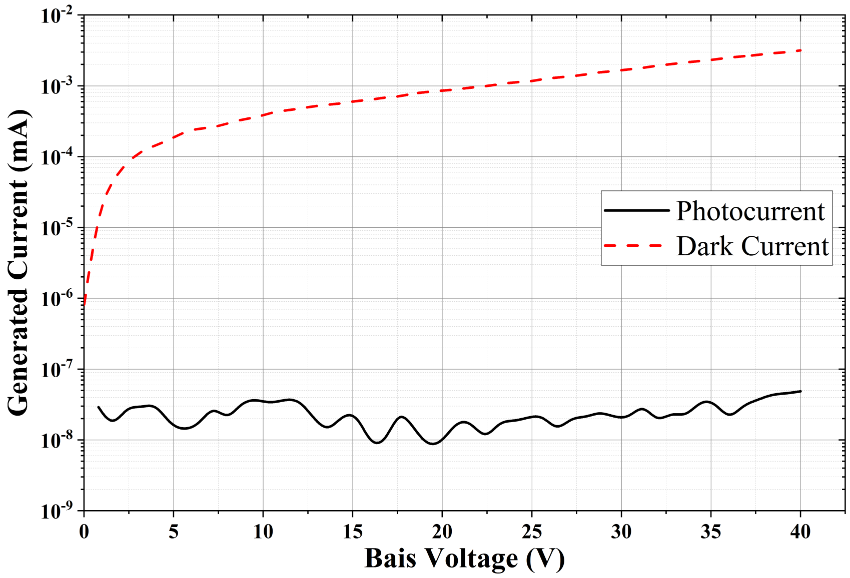

FIGURE 5.23: DC caharactrization of the interdigitated photomixer with 6-8 layers graphene [99].

photomixer was taken by varying the bias voltage from 0 V to 40 V. The interdigitated 6-8 layers graphene photomixer showed a maximum reliable generated photocurrent of 3 mA at 40 V without damage to the device and an on/off ratio of five orders of magnitude can be achieved, where the photomixer exhibits a dark current of 0.4 nA. The ability of the interdigitated 6-8 layers graphene photomixer to operate under a high bias field is attributed to the thicker graphene nanoelectrodes, which enhance the current flow and increases the reliability. Figure 5.23 shows the difference between the generated photocurrent and dark

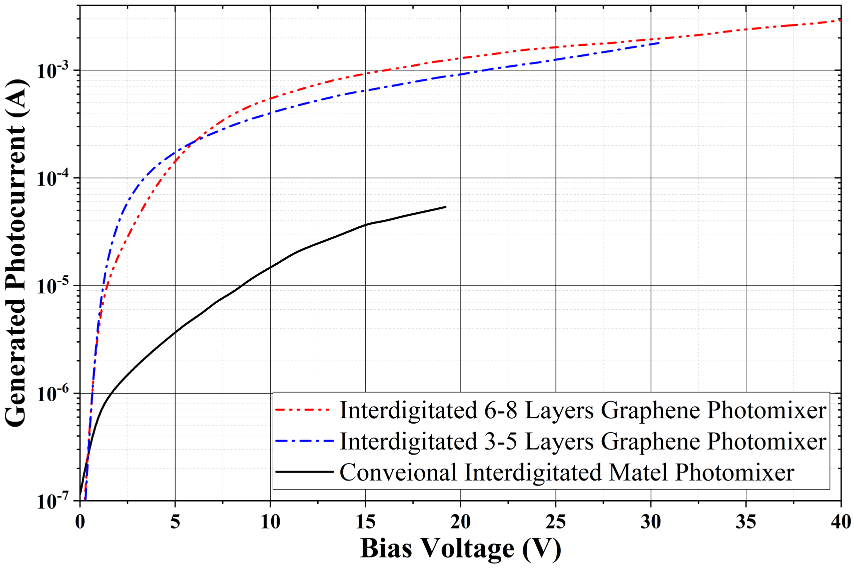

FIGURE 5.24: Comparison of the DC caharactrization of the interdigitated 3-5 and 6-8 layers graphene photomixers [100].

current. The DC measurement results of the photomixer with interdigitated 6-8 layers graphene nanoelectrodes were compared with the obtainable generated photocurrent of the photomixer with interdigitated 3-5 layers graphene nanoelectrodes as well as the conventional interdigitated metal photomixer from Figure 5.17. The generated photocurrent of both interdigitated graphene photomixers is at least one order higher than the generated photocurrent of the conventional interdigitated metal photomixer due to the transparency of the graphene which allows almost all of the optical beat signal to propagate through the graphene combining with the shorter transit time required for the generated carriers to travel from one electrode to another. The use of transparent interdigitated graphene increases the carrier density that leads to a higher photocurrent. On the other hand, due to the higher transparency of the 3-5 layers graphene than the 6-8 layers graphene, the generated photocurrent of the 3-5 layers graphene was higher at low bias voltage (< 6 V). On the other hand, by increasing the bias voltage above 6 V, the lower resistivity of the 6-8 layers graphene plays a crucial effect to increase the current flow and handling a high photocurrent, which more than 30 V can be reached, see Figure 5.24.

5.2.2 THz Signal Measurement Results

Two detuned DFB-LDs (center wavelength ~ 850 nm) were used to generate the optical beat signal ($P = 30$ mW) with a beating frequency corresponding to the frequency difference between the two DFB-LDs. By changing the frequency difference between the two DFB-LDs, the range between 50 GHz and 1 THz was covered. A bias voltage of 15 V was chosen to accelerate the photogenerated carriers. The corresponding THz output power of the device can be calculated by dividing the measured lock-in signal (voltage) by the responsivity of the Golay cell at a certain chopping frequency.

As expected from the results of the DC measurements, a significant improvement is obtained in the THz measurement results due to the use of multilayer graphene nanoelectrodes instead of the interdigitated metal finger electrodes.

1. **Single gap 6-8 layers graphene photomixers**
   The lock-in signal level is clearly increased for the whole THz measurement range, see Figure 5.25. Due to the transparency of the multilayer graphene nanoelectrodes, the single gap graphene photomixers with 5 μm photomixer exhibits more than one order of magnitude higher THz output signal than the THz output signal of the conventional interdigitated photomixer for the whole measurement range. While the single gap graphene photomixers with 10 μm photomixer show more than twice THz output signal higher than what can be achieved from the conventional interdigitated photomixer. The significant enhancement in THz output signal of the single gap graphene photomixers with 5 μm photomixer is attributed to the transparency of the graphene combining with the lower device capacitance, which is half the device capacitance of the single gap graphene photomixers with 10 μm photomixer. The equation (2.17) confirms that the lower the capacitance the higher the THz output power.

2. **Interdigitated 3-5 layers graphene photomixer**
   The measurement results of the interdigitated 3-5 layers graphene photomixer were compared with the THz output signal of the conventional interdigitated metal photomixer. The measurements of the THz output signal were performed under the same measurement conditions. The interdigitated 3-5 layers graphene photomixer shows about one order of magnitude higher THz output signal than what can be obtained by the conventional interdigitated metal photomixer, see Figure 5.26. The higher THz output signal is due to the high transparency of the graphene nanoelectrodes.

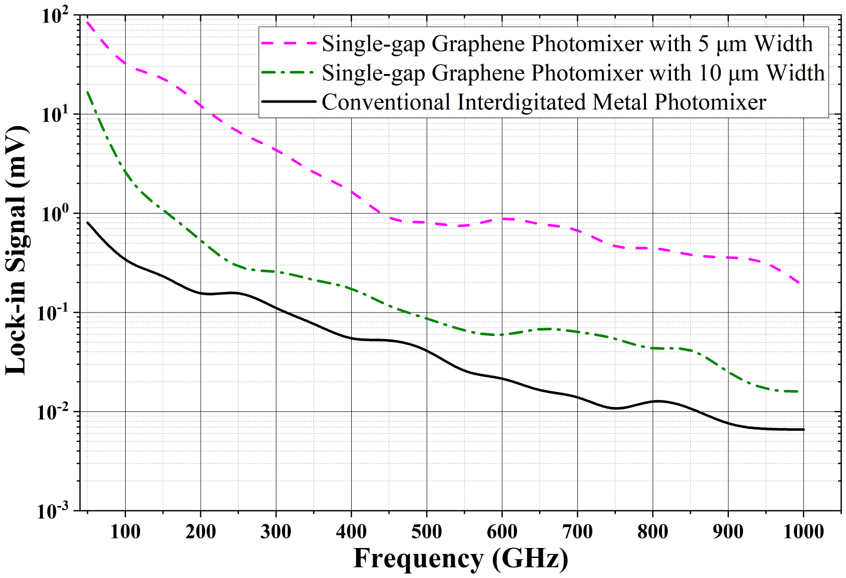

FIGURE 5.25: Comparison of the THz output signal measurement of the single gap graphene photomixers and the conventional interdigitated metal photomixer.

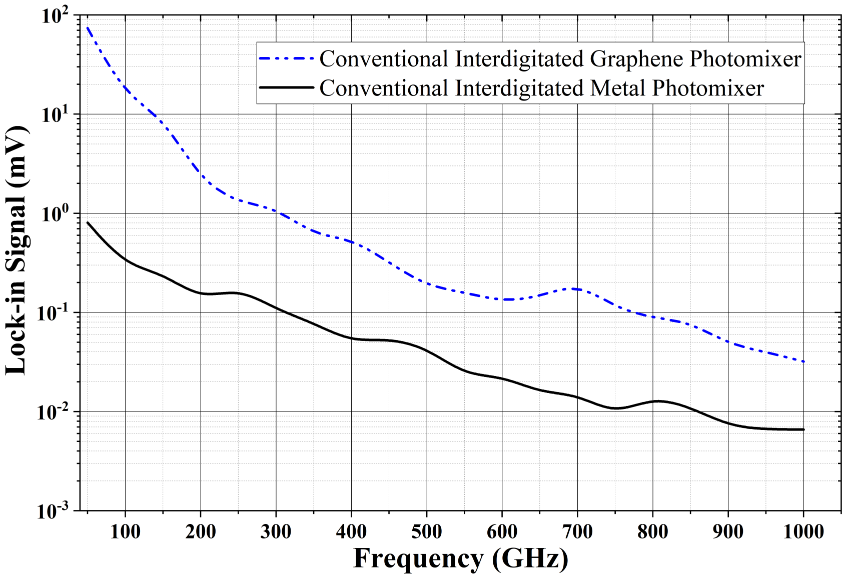

FIGURE 5.26: Comparison of the THz output signal measurement of interdigitated 3-5 layers graphene and metal photomixer.

The measurement results were compared with the obtained THz output signal of the single gap graphene photomixers. The interdigitated 3-5 layers graphene photomixer shows a higher THz output signal than what can be obtained by the single gap graphene photomixer with 10 μm, see Figure 5.27. The higher THz output signal is due to higher photoconductor gain. The transit time of the electron from one to another graphene nanoelectrode is shorter in the interdigital configuration compared to the single gab design of the 6-8 layers graphene. Furthermore, the higher transparency of the 3-5 layers graphene

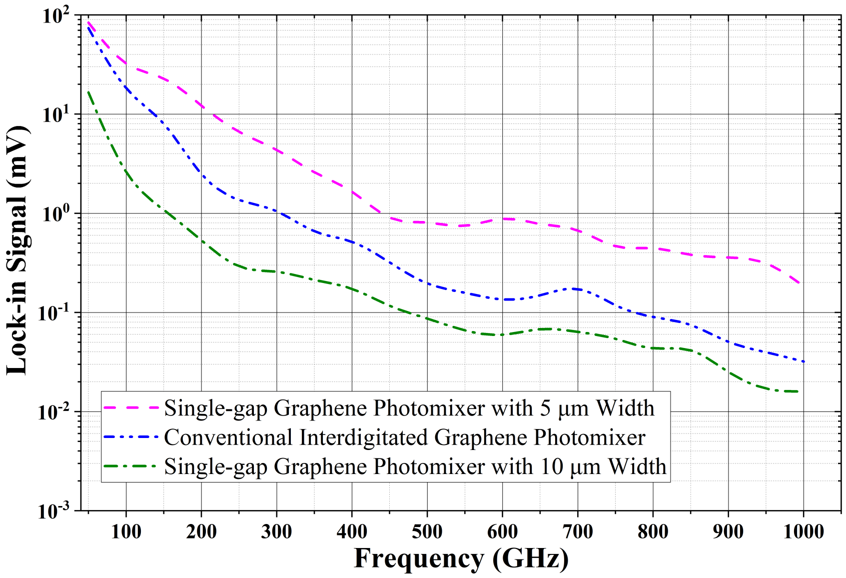

FIGURE 5.27: Comparison of the THz output signal measurement of the single gap graphene photomixers and the interdigitated 3-5 layers graphene photomixer [101].

used in the interdigital structure can enhance the THz output signal. On the other hand, the lowest capacitance value and the enhanced current flow in the 6-8 layers graphene allows the single gap graphene photomixer with 5 μm to provide the highest THz output signal. Where the device capacitance of interdigitated, single gap and 5 μm width, and single gap and 10 μm width graphene nanoelectrodes were $\sim$ 3 fF, $\sim$ 2.9 fF, and $\sim$ 1.4 fF, respectively. Therefore, the THz output signal of the 5×5 μm^2 6-8 layers graphene photomixer with a single gap of 1 μm is higher especially in the upper part of the THz regime as shown in Figure 5.27.

3. Interdigitated 6-8 layers graphene photomixer

A similar THz output signal measurement was performed for the interdigitated 6-8 layers graphene photomixer. The measurement scan was performed using the python program with 5 GHz frequency steps to obtain a highly accurate measurement. The same measurement conditions were applied here (the total optical power is 30 mW, the wavelength is $\sim$ 850 nm, and the bias voltage is 15 V). The measurement results were compared with the THz output signal of the conventional interdigitated metal photomixer. Similar to the interdigitated 3-5 layers graphene photomixer, the interdigitated 6-8 layers graphene photomixer shows one order of magnitude higher THz output signal than the THz output signal of the conventional interdigitated metal photomixer as shown in Figure 5.28. The enhancement in the THz output signal is attributed to the

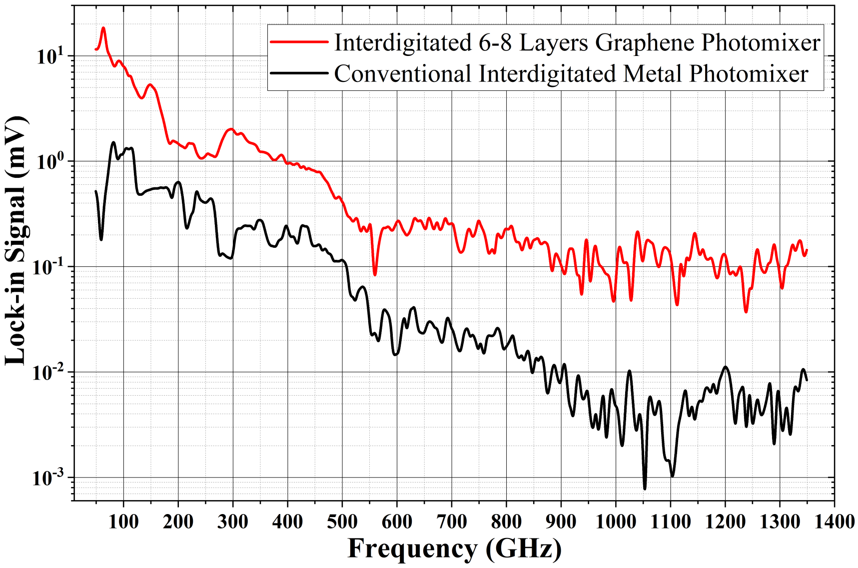

FIGURE 5.28: Comparison of the THz output signal measurements of the interdigitated 6-8 layers graphene and metal photomixers.

high transparency of graphene and the high capability of graphene to handle higher photocurrent.

The effect of the variation of the graphene layers on the THz output signal was investigated by comparing the measurement results. The THz measurements of the interdigitated 6-8 layers graphene photomixer were compared with the THz measurements of the interdigitated 3-5 layers graphene photomixer. Due to the less resistivity of the 6-8 layers graphene, the current flow in the thicker graphene layers was increased. This increasing the current flow provides a higher capability to handle higher photocurrent and a higher THz output signal can be achieved. Figure 5.29 shows the tendency of the THz output signal of the photomixers with the interdigitated graphene nanoelectrodes. The photomixer with 6-8 layers graphene nanoelectrodes shows a slightly higher power than the output power of the photomixer with 3-5 layers graphene nanoelectrodes especially in the upper part of the THz regime.

Figure 5.30 shows how much the performance has been improved over the entire measurement range for THz photomixer by using interdigitated 3-5 and 6-8 layers graphene configuration instead of conventional metal electrodes. The output power of the interdigitated 3-5 layers graphene photomixer improved by a factor of five at low frequency (> 800 GHz) as compared to the conventional interdigitated photomixer, in the high-frequency range even more than one order of magnitude higher output power levels were achieved.

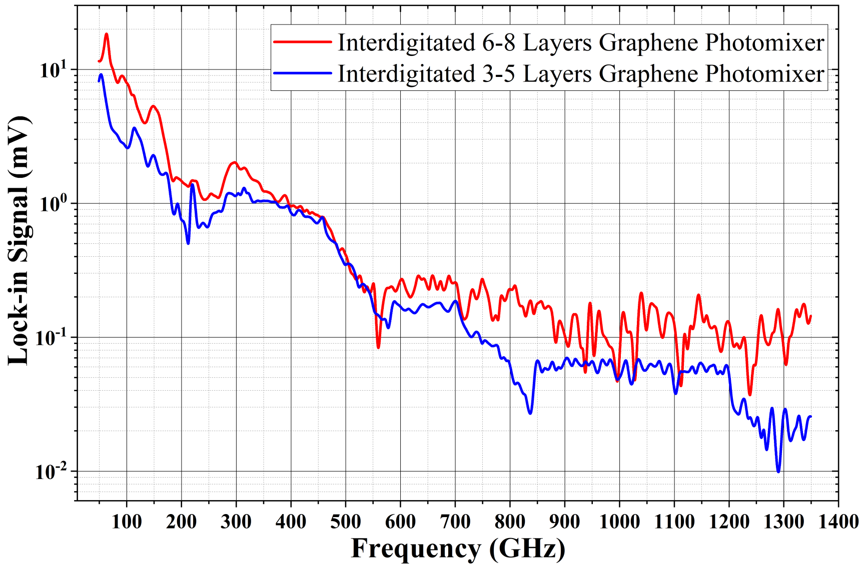

FIGURE 5.29: Comparison of the THz output signal measurements of the interdigitated 3-5 and 6-8 layers graphene photomixers.

The interdigitated 6-8 layers graphene photomixer exhibits higher output power for the whole measurement range. This increase in the output power is attributed to the less resistivity of the 6-8 layers graphene, which enhances the current flow in the thicker graphene layers. Generally, all THz photomixers showed approximately the same noise level. Therefore, the improvement in the THz output signal of a photomixer allows the device to operate as a THz source for much broader frequency ranges than that of the conventional interdigitated photomixer under the same antenna specifications.

5.3 Summary

The effect of using graphene as nanoelectrodes for various CW THz sources was investigated. Various designs (single gap and interdigitated configurations) were implemented using various graphene layers (3-5 and 6-8 layers). The nanoelectrodes design changes the device capacitance and the transit time for the carriers to travel from one electrode to another. This affects the value of the THz output signal. The single gap graphene photomixers with 5 μm show a significant reduction in the device capacitance, which allows one order higher THz output signal higher than that of the conventional interdigitated metal photomixer. On the other hand, the interdigitated nanoelectrodes exhibit a shorter transit time required for the carriers to travel from one finger to another. Due to this reduction of the transit time combined with the high transparency of graphene, the interdigitated graphene photomixer

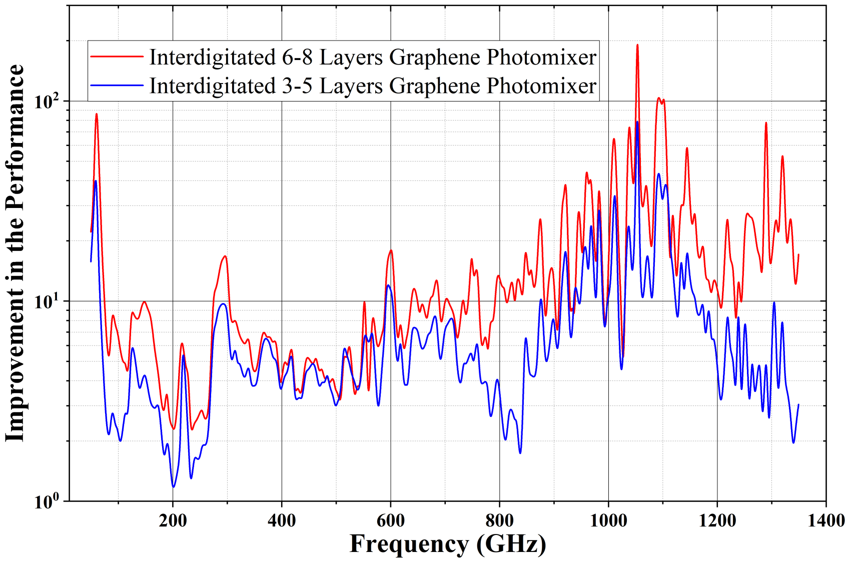

FIGURE 5.30: The ration of the performance of the interdigitated 3-5 and 6-8 layers graphene photomixers to the performance of the conventional interdigitated metallic photomixer over the whole spectral range of the measurement.

shows more than one order of magnitude higher THz output signal than what can be achieved by the conventional interdigitated metal photomixer. Furthermore, the number of graphene layers plays a big role in the electrical and optical properties of graphene nanoelectrode. On one hand, thinner graphene increases the transparency of the nanoelectrodes to improve the power conversion efficiency, and on the other hand, thicker graphene is required to carry high current densities and enhance the photomixer performance. The interdigitated 6-8 layers graphene photomixer shows higher reliability at high photocurrent than the interdigitated 3-5 layers graphene photomixer.

Chapter 6

Graphene Based THz Detector

The significant advantage of photomixer devices is that they can also be used as THz detectors. In this approach, a detector (photomixer) will be operated without an external bias for a THz wave originated from an emitter (another photomixer). For CW detection, the same optical beat signal, which is previously used to generate THz waves by applying a bias field, is also used to generate free carriers, which will be separated by the received THz waves and delivered to the detector antenna. The detected photocurrent is proportional to the product of the optical beat signal and the THz wave intensity. Therefore, the same principle of increasing the generated photocurrent is applied here. Increasing the number of generated photocarriers will result in a higher detected photocurrent.

THz detectors based on interdigitated graphene and gold photomixers were compared using a commercial THz source from TOPTICA Photonics GmbH. For this purpose, the commercial THz source was established in a homodyne coherent detection using the mechanical optics in Figure 4.10. A Si lens is used to collimate THz waves onto the photomixer detectors. In contrast to the Golay Cell detector, the Si lens has a smaller aperture window. Therefore, accurate system alignment is required for measurements to be made.

6.1 THz Setup Alignment

A TeraScan 780 system was borrowed from TOPTICA Photonics GmbH to characterize the graphene-based THz photodetectors. The TeraScan 780 system is based on a spiral emitter and detector photomixers. The optomechanical assembly in Figure 6.1 consists of two 3-axis stages. Each one has used to adjust one photomixer. There are also two parabolic mirrors, each one has 2 off-axis to collimate and refocus the THz beam. Both combined packages with the photomixers were mounted vertically on a rail, which can be considered as a manual delay stage. The length of the collimated beam path can easily change by moving one of the combined packages or both of them. This step was done to achieve a zero path difference between the receiver and the THz generation arm including the collimated beam path. When the system is correctly aligned, such a length shift should only have a minimal impact on the THz amplitude. It is worth mentioning that changing the length of the collimated beam path does not change the beam alignment, but serves to vary the THz phase.

The THz setup preparation was performed by applying four steps as follows:

1. **Alignment the collimated THz beam using a visible light source.**
   Visible light was mounted in the same position as the THz source. A target sign was placed in the same position as the THz receiver. The two mirrors were adjusted by their 2 off-axis to achieve the light spot in the center of the target sign. Fine adjusting to the mirrors should be made so that when the distance between the mirrors is changed, the light spot does not change from the center of the target sign.

2. **Alignment the vertical position of the photomixers.**
   The photomixers were placed in their positions. the vertical alignment was adjusted for both photomixers so that both photomixers have the same height. the distance between the front facet of the photomixers and the center of the mirrors. According to the datasheet provided by TOPTICA, the optimum distance should be 30 mm.

3. **Alignment the collimated THz beam using the THz photomixers.**
   The control system was used to measure the primary non-zero THz signal. If there is no signal at all, then start at a lower frequency (e.g., 100 GHz or 200 GHz). At lower frequencies, both, terahertz power and detection efficiency are higher and therefore the signal is stronger. Also, the larger wavelength facilitates the alignment. Fine chancing of the distance was made to achieve

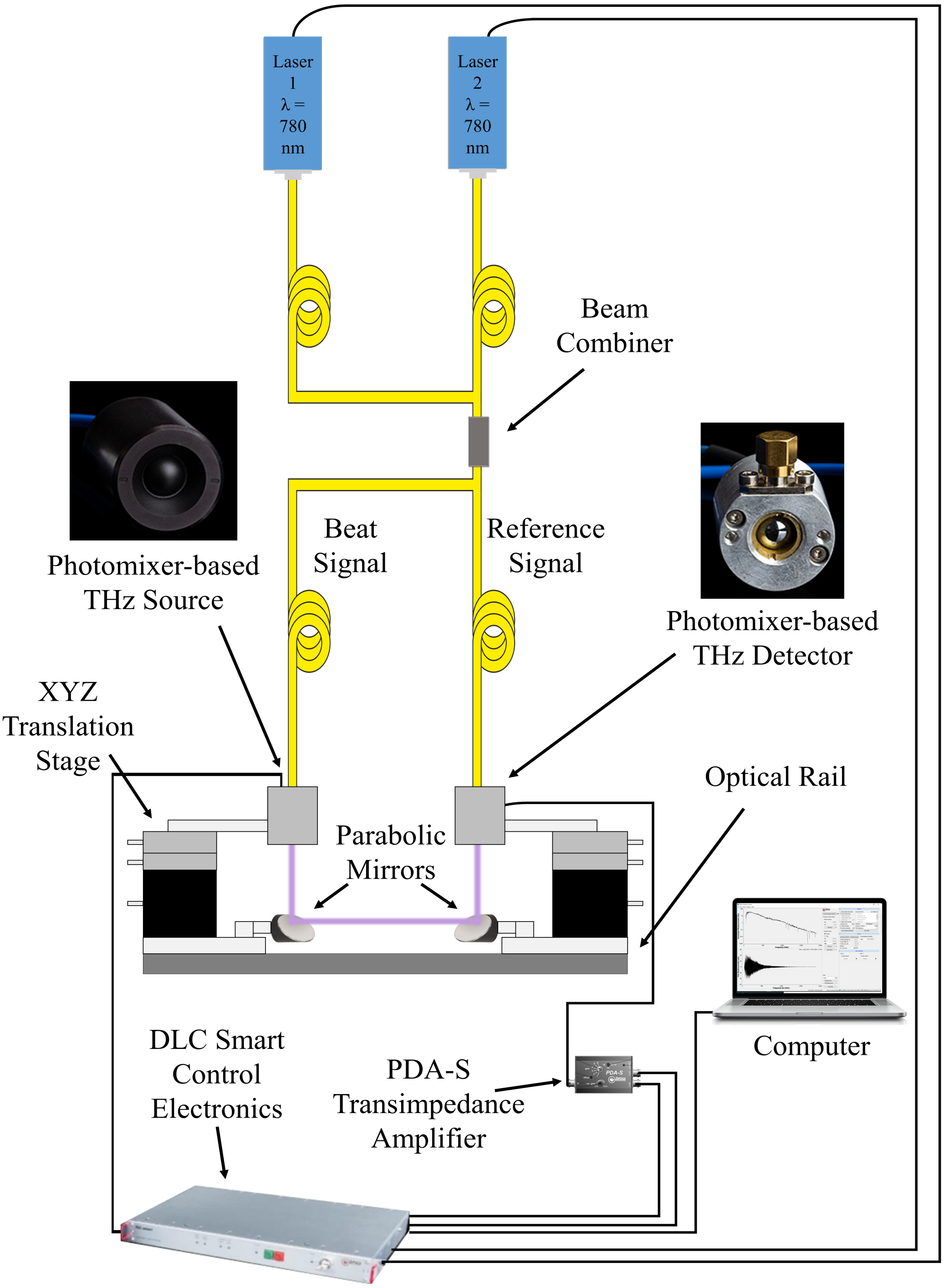

FIGURE 6.1: TU Darmstadt detection system using Toptica source and detector.

a positive or negative maximum of the signal. The goal of these steps is, to adjust the amplitude so that it matches, as much as possible, the value of the received signal specified in the production and quality control datasheet of TOPTICA [102].

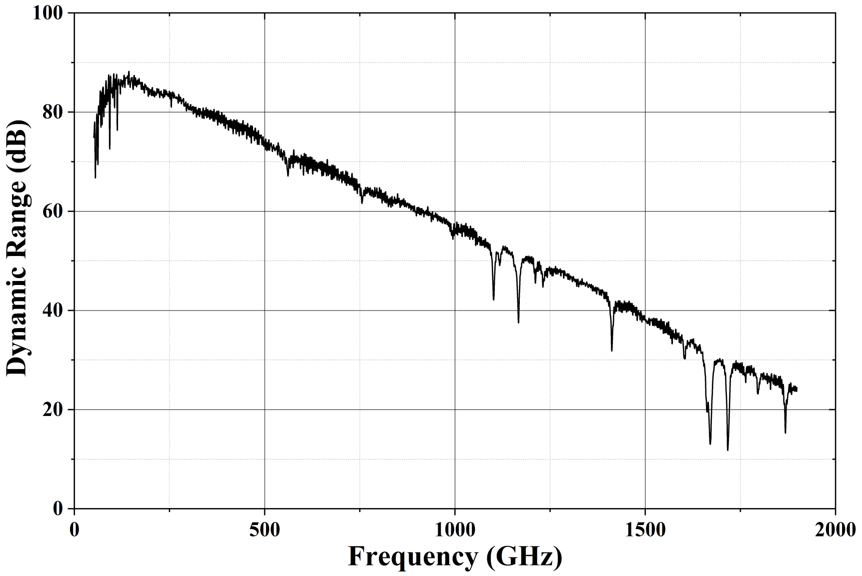

FIGURE 6.2: Spectrum acquired with TU Darmstadt optomechanics.

4. Checking the THz path alignment.

Both photomixers were moved together back and forth in the same direction of the collimated THz beam path. If there is no change in the value of the detected photocurrent signal, means the photomixers are in good alignment.

Noise characteristics of photoconductive detectors are very important. The noise photocurrent in the receiver I_{noise} can easily be determined by switch off the photomixer based emitter, and recording the generated current at the receiver. The resulting root mean square value is the measure of I_{noise}. Once the noise properties are known, the dynamic range DR of the terahertz power is computed via

$$DR(f) = 20\log\left(\frac{I_{signal}(f)}{I_{noise}}\right) \tag{6.1}$$

where$I_{signal}(f)$ is the signal photocurrent at a given frequency f. The dynamic range of TOPTICA's TeraScan 780 system is given in [102]. The obtained dynamic range that achieved (with 300 ms of integration time) shown in Figure 6.2 is considered as an accepted value for the system. By that, the coherent THz detection system is ready to characterize the THz receivers.

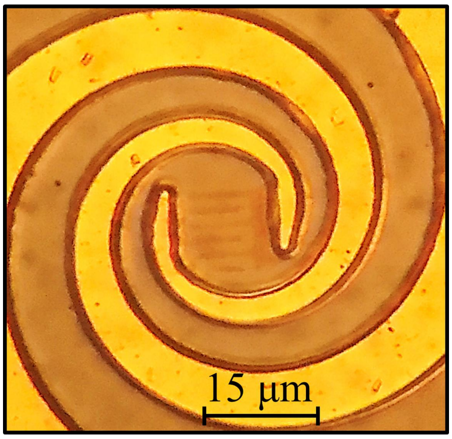

FIGURE 6.3: Microscopic image of the spiral antenna with interdigitated graphene configuration.

6.2 Graphene Detector Fabrication

A Multilayer graphene photomixer was fabricated to investigate the performance of the multilayer graphene as transparent nanoelectrodes to enhance the performance of the photomixer devices as THz detectors. Since the commercial THz emitter is based on a spiral antenna, which provides a circularly polarized wave, a spiral antenna was used to fabricate the graphene photomixer with interdigitated nanoelectrodes. The method of manufacturing the device is not different from the method of manufacturing the devices in 4.2. Where the 6-8 layers graphene is transferred first on top of LTG-GaAs substrate. Then Ni (25 nm) and Au (150 nm) were evaporated to form the spiral antenna with an active area of $10 \times 10\ \mu m^2$. The interdigitated nanoelectrodes were formed using the optical lithography process. The fingers' length and width were 9 μm and 0.5 μm, respectively. The spacing gap between fingers was 1.5 μm. A layer of SiNx was deposited on top of the device to isolate the nanoelectrodes from environmental contamination as well. The optical microscopic image of the spiral antenna with interdigitated graphene configuration is shown in Figure 6.3.

Scanning electron microscope and Raman spectroscopy were used to confirm the presence of graphene and the number of the graphene layers in the active area between the antenna contacts. Figures 6.4 and 6.5 show the SEM image and the Raman spectrum for the 6-8 layers graphene nanoelectrodes. The amplitude of the 2D peak of the Raman spectrum in Figure 6.5 confirms the thickness of the 6-8 layers graphene provided by [77].

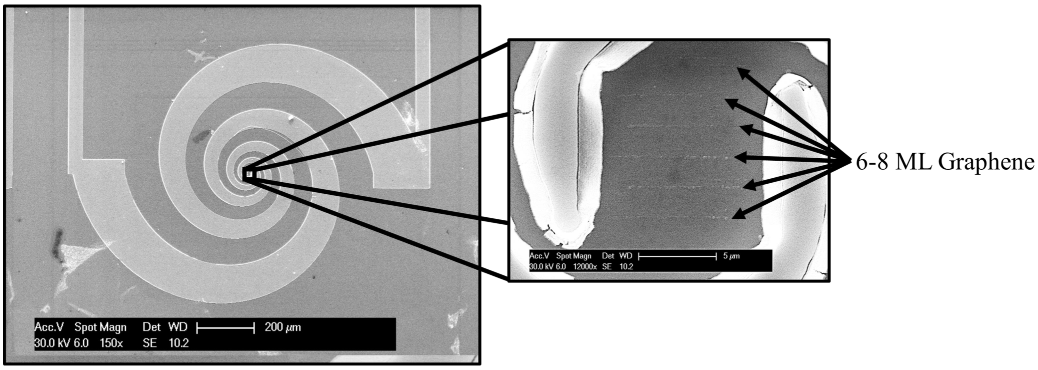

FIGURE 6.4: SEM photos of interdigitated graphene photomixer.

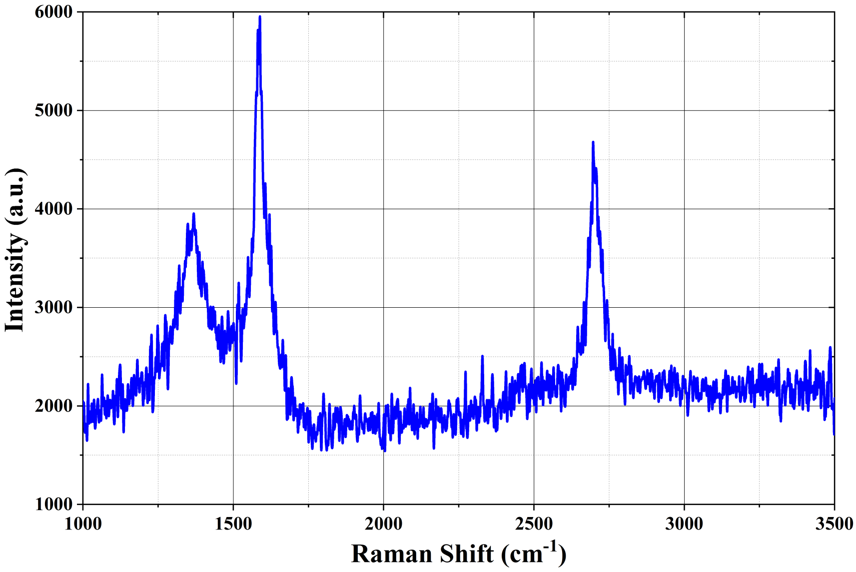

FIGURE 6.5: Raman spectra of the 6-8 layers graphene.

6.3 THz Measurements and Results

Interdigitated THz photomixers with graphene and with gold electrodes were characterized as detectors using TOPTICA TeraScan 780 system. Where the commercial THz receiver in Figure 6.1 was replaced with the interdigitated graphene and gold photomixers, as shown in Figure 6.6. Two detuned DFB-LDs ($\lambda = 780$ nm) were used in a homodyne detection system. The total optical power of 31 mW and 30.5 mW were used to illuminate the active area of the emitter and the detector photomixers, respectively. The radiation range of the THz beam was tuned by varying the frequency difference between the two detuned DFB-LDs. A scanning range of the THz radiation from 50 GHz to 1.9 THz was obtained. With a very fine adjustment of the optomechanical parts, a frequency-dependent photocurrent for both photomixers can be detected. When the terahertz frequency is scanned, the photocurrent measured in the receiver exhibits a sinusoidal pattern. The amplitude of the sinusoidal

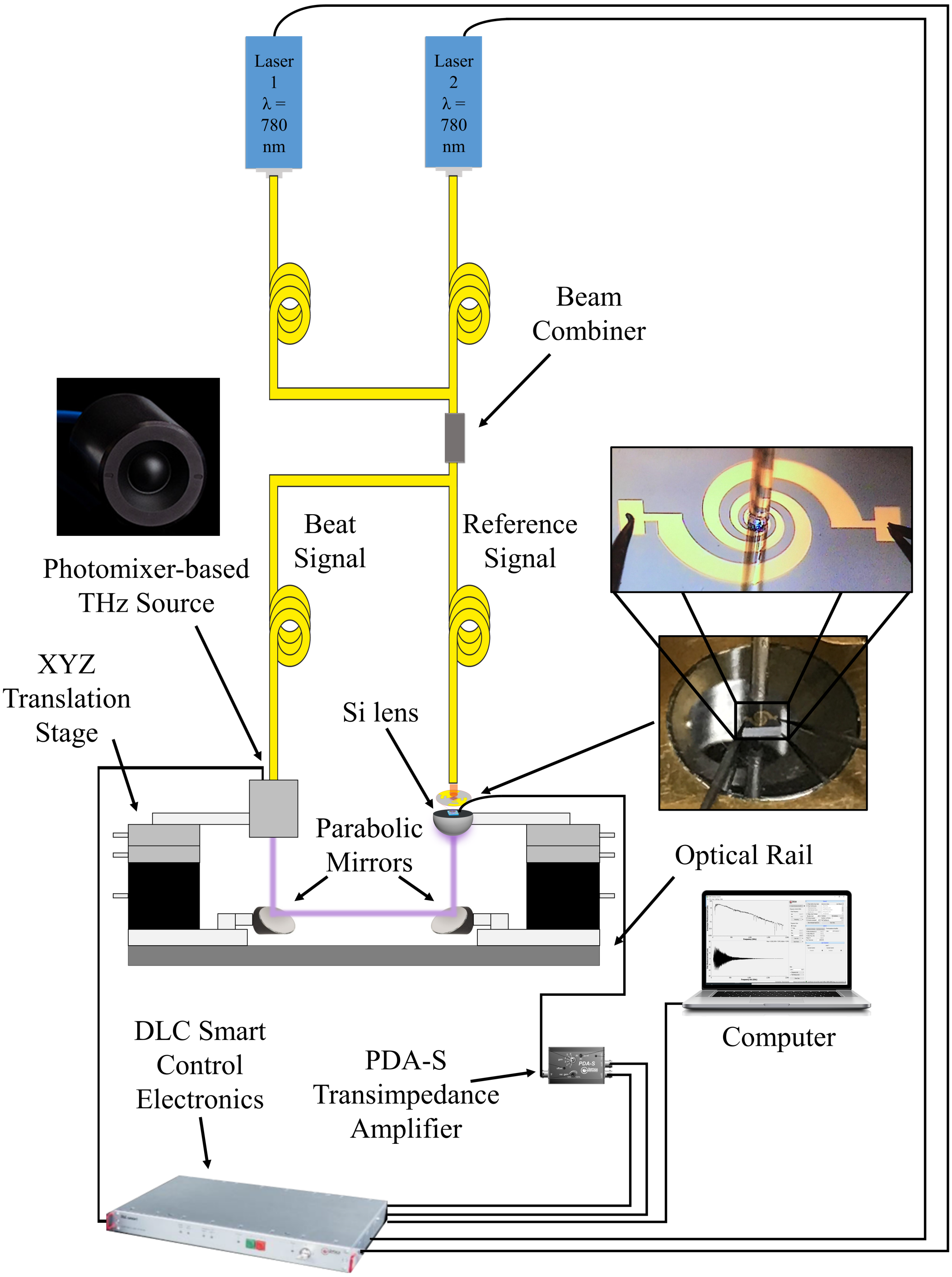

FIGURE 6.6: THz detectors characterization.

function of the measured photocurrent is decreased for a higher frequency, as shown in Figure 6.7.

TOPTICA'S TeraScan Control software offers the possibility to compute the envelope photocurrent in real-time, where the envelope of the fringe pattern yields the

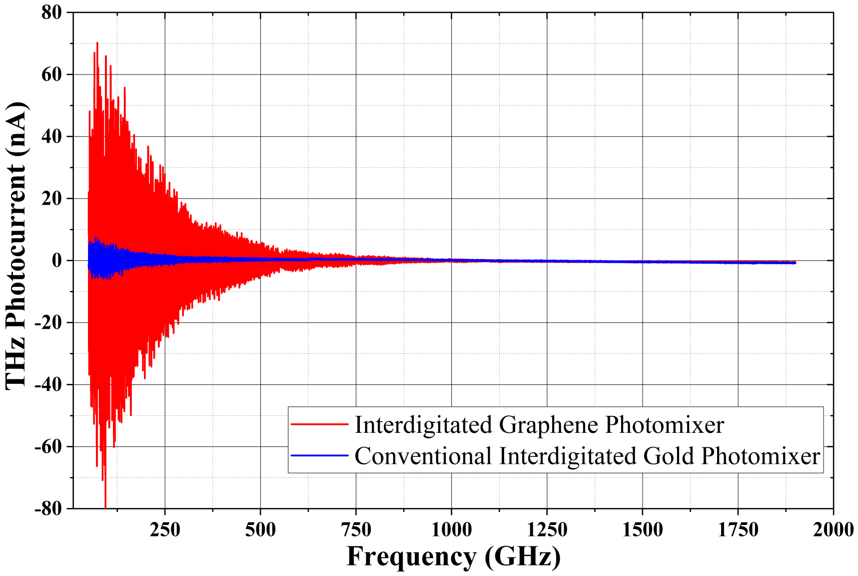

FIGURE 6.7: Comparison of the detected THz photocurrent of the interdigitated graphene and gold photomixers.

terahertz spectrum.

For the measurement, the frequency step of 0.05 GHz was chosen. Figures 6.7 and 6.8 show the detected and the envelope of the THz photocurrent for the photomixer with graphene nanoelectrodes and in comparison with the reference data obtained using the conventional photomixer with gold electrodes, respectively. From the measurement results, due to the high transparency of graphene nanoelectrodes, the range of oscillated photocurrent of the interdigitated graphene photomixer is higher than that of the conventional interdigitated gold photomixer over the whole frequency range. The envelope of the detected photocurrent of the photomixer with interdigitated graphene nanoelectrodes exhibits more than one order of magnitude higher than the obtained photocurrent detected by the conventional interdigitated gold photomixer. Furthermore, the photomixer with graphene nanoelectrodes was able to detect the THz beam up to 1.25 THz, which is considered as twice the spectral range of the detected THz beam by the conventional interdigitated photomixer, up to 600 GHz. This enhancement in the device performance is attributed to the high conductivity and high transparency of graphene, which allows almost all of the light beam to propagate through the nanoelectrode material and increase the number of carriers that are used to modulate the THz biasing field, on one hand. On the other hand, the high THz absorption by the thin graphene layer leads to generate a higher electrical field between the antenna contact.

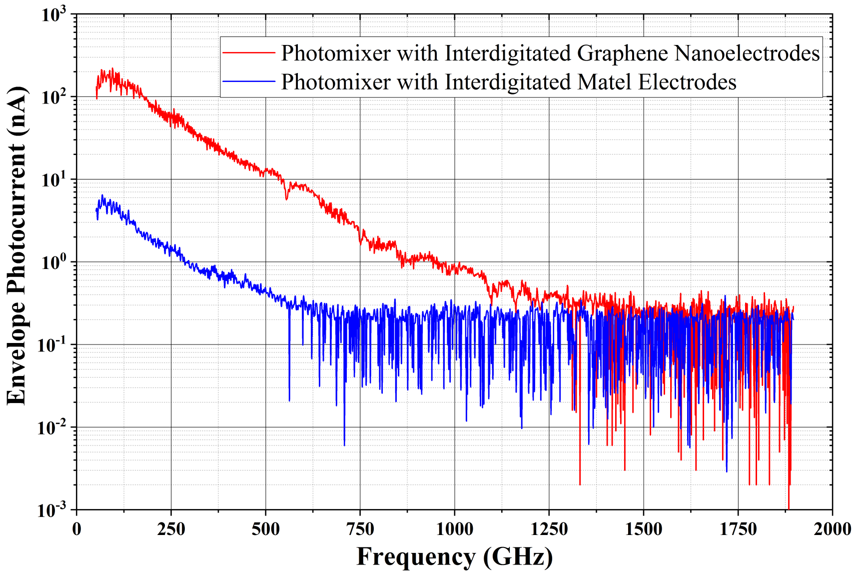

FIGURE 6.8: Comparison of the envelope of the detected THz photocurrent of the interdigitated graphene and gold photomixers.

6.4 Summary

Room temperature coherent detection of CW THz radiation was demonstrated in this chapter using interdigitated photomixers with graphene nanoelectrodes. The photomixer fabricated on LTG-GaAs as photoconductive material. The measurement results were compared with conventional interdigitated metal photomixer. The high transparency of the graphene sheet allows almost all of the light beam to propagate through the nanoelectrodes. The high the propagated light, the higher the carrier density, the higher the detected current. The measurement results show more than one order of magnitude higher detected current as compared to the detected current of the conventional interdigitated photomixer. Additionally, the interdigitated graphene receiver was able to detect twice the range of the detected THz beam by the conventional interdigitated gold receiver. This offers a path to produce highly responsive devices for THz applications.

Chapter 7

Hybrid Nanoelectrodes Based THz Emitter

Chapter 3 and Chapter 4 have discussed the enhanced performance of the THz sources and detectors based on graphene nanoelectrodes photomixer devices. In this chapter, the performance enhancement of the THz photomixer will be discussed using hybrid nanoelectrodes based on graphene and silver nanowire.

7.1 Advantages of the Hybrid Nanoelectrodes

Similar to graphene, nanowires demonstrate unprecedented enhanced functions essential to many areas of technology [103–105]. Silver nanowire (Ag-NW) THz photomixer has shown approximately one order of magnitude lower device capacitance than the conventional interdigitated photomixer. The reduction in the value of the device capacitance is due to the low fill factor (small contact area) in the active area of the photomixer. The effect of the low capacitance of the Ag-NW based photomixer results in a higher generated photocurrent, higher THz power, and wider frequency range as compared to conventional interdigitated photomixers [22]. Another reason for this enhancement of the Ag-NW based THz photomixer is the surface plasmon polaritons (SPP), which are obtained from the wave patterns of the SPP on the Ag-NW. The SPP on the Ag-NW was measured using a scattering-type scanning near-field optical microscope. [106]. The surface of the Ag-NW is atomically smooth, which reduces the overall propagation loss as compared to other materials. However, due to the very small structures, the light coupling for plasmon excitation into Ag-NWs remains a practical issue [107]. Furthermore, due to the low fill factor of the Ag-NW and the long transit time for the generated photocarriers, which are generated far from the nanowire, the contribution of these generated photocarriers will be lost. One of many solutions to these problems is employing the use of graphene and Ag-NW as hybrid nanoelectrodes for the photomixer.

The combined use of graphene and Ag-NW enhances the performance of the device that was reported in [108–110], which makes them a very promising material as a hybrid nanoelectrodes for THz photomixer devices. The NWs with a low fill factor can improve their own conductive paths by the conductivity of graphene. Where the photocarriers that generated far from the Ag-NWs will be drifted to the Ag-NWs electrodes through graphene. In this approach, graphene will act as a local transport center, and hence, the mean free path of the photocarriers will be reduced. Due to the reduced path of the photocarriers, the carrier lifetime will be reduced. Furthermore, the plasmonic enhancement at the edges of the graphene creates rich sources of generated photocarriers resulting in high drift current densities. The drifted current will be captured by the Ag-NW due to the presence of the SPP of the Ag-NW. The Ag-NW serves as a highly capable transport waveguide for the high current densities. Accordingly, the charge will transport simultaneously in the hybrid nanoelectrodes depending on the conductivity of the graphene and Ag-NW, where each part complements the advantages of the other component [109].

In this work, the hybrid nanoelectrodes for a CW THz photomixer consist of Ag-NW and various graphene types. Graphene flakes and multilayer graphene sheets as islands were fabricated as a part of nanoelectrodes. Due to the small size of the graphene, the light will be confined around the graphene. This light confinement will enhance the electric field between the graphene. The prediction of the electric field enhancement due to the light confinement was studied using Microwave Studio CST software.

Despite the very small size of the nanomaterial, the nanoelectrodes provide the capability of handling rather high currents [22], Where the high transparency and conductivity of graphene with the low fill factor of nanowire nanoelectrodes leading to higher photocurrents and higher THz output signals as compared with that of the conventional interdigitated finger electrodes.

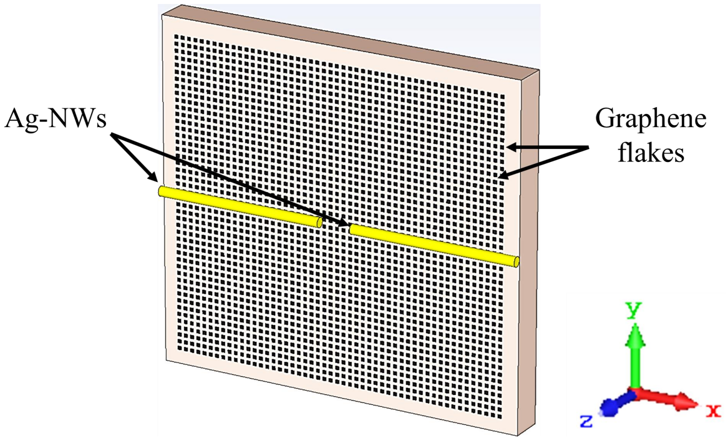

FIGURE 7.1: The simulated layout of the hybrid nanoelectrodes based on 100 × 100 nm^2 graphene flakes and 300 nm nanowire.

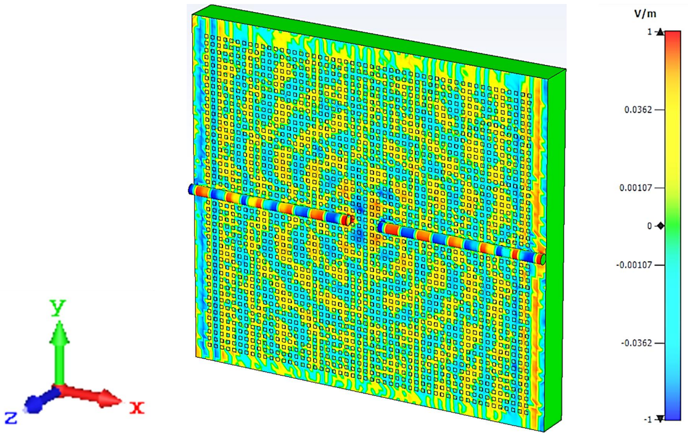

FIGURE 7.2: The CST simulation results of the generated electric field between the nanoelectrodes (100 × 100 nm^2 graphene flakes and 300 nm nanowire).

7.2 Hybrid Nanoelectrodes Simulations

Hybrid nanoelectrodes photomixers were simulated using the Microwave Studio CST software. The generated electric field between the nanoelectrodes due to various graphene sizes and Ag-NW were compared. The simulations were classified according to the graphene sizes and the diameter of the nanowire.

7.2.1 100 × 100 nm^2 Graphene and 300 nm Nanowire

Patterned graphene with optimized separation of graphene nanoparticles will improve the spatial plasmonic motion of the photocarriers drifted to the Ag-NW electrodes. For the simulation, the dimensions of graphene squares were 100 × 100 nm^2 and the thickness was 3 nm to mimic the graphene flakes. The separation between the squares was fixed to be 100 nm. Two Ag-NWs with a diameter of 300 nm were

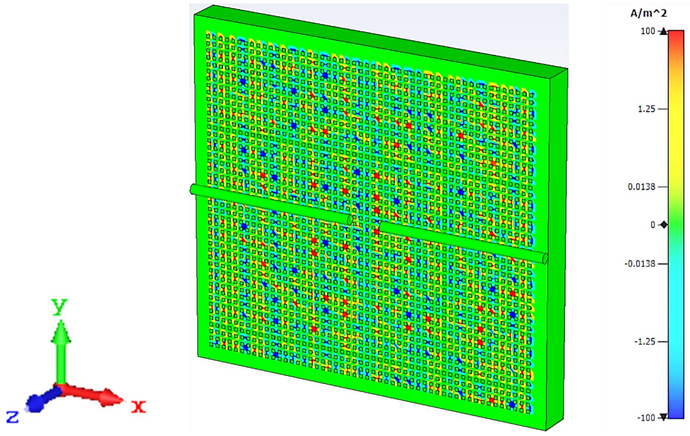

FIGURE 7.3: The CST simulation results of the generated current density of the hybrid nanoelectrodes (100 × 100 nm^2 graphene flakes and 300 nm nanowire).

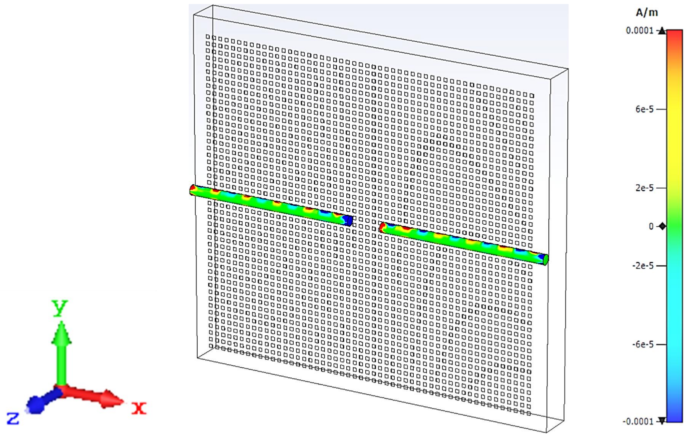

FIGURE 7.4: The CST simulation results of the surface current of the hybrid nanoelectrodes (100 × 100 nm^2 graphene flakes and 300 nm nanowire).

located at the center of the simulated active area with a 1 μm separation gap between them, see Figure 7.1. A full plane wave (electromagnetic wave) was located at a distance of 0.25 μm from the structure. From the simulation results, it is very clear that the light is confined around the graphene squares due to the small size of the graphene squares. This light confinement enhances the electric field between the graphene squares. The simulation results show a maximum electric field of 0.295 V/cm, as shown in Figure 7.2, which is about one order of magnitude higher than the value of the electric field of the gold electrodes, see section 5.1. Due to the high transparent graphene squares, which allows almost all of the optical beat signal to propagate through graphene material and increase the carrier density, the maximum current density of 13 A/cm^2 for the hybrid nanoelectrodes was calculated, see Figure 7.3. The high current density was confined close to the edges of the squares. Because of this confinement, the generated photocarriers are transported between

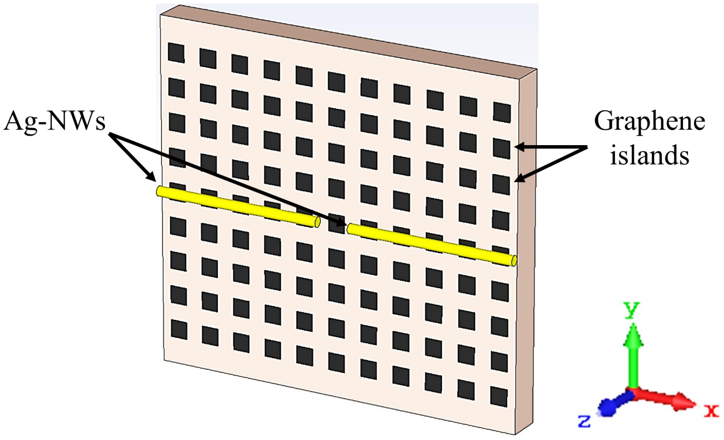

FIGURE 7.5: The simulated layout of the hybrid nanoelectrodes based on 500 × 500 nm^2 graphene islands and 300 nm nanowire.

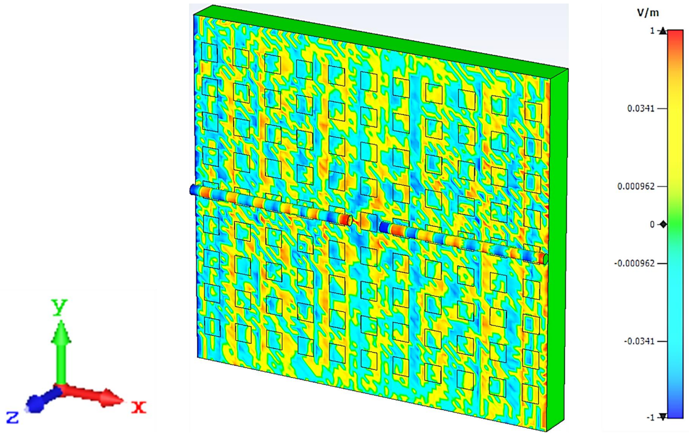

FIGURE 7.6: The CST simulation results of the generated electric field between the nanoelectrodes (500 × 500 nm^2 graphene islands and 300 nm nanowire).

these squares by a spatial plasmonic field, and this makes the graphene squares act as connected rather than isolated. The generated photocarriers are drifted to the Ag-NW. In this way, the conductivity of the NWs was improved by the high conductivity of the graphene squares, where the simulation results show a maximum surface current of 133×10^{-6} A/cm between the graphene squares and Ag-NW, as shown in Figure 7.4. Despite the small size of the Ag-NWs provide the necessary capability of handling rather high currents.

7.2.2 500 × 500 nm^2 Graphene and 300 nm Nanowire

The graphene islands (GIs) were mimicked and simulated as squares. The properties of the photoresist material used for the optical lithography process limit the pattern resolution to around 400 nm. Therefore, graphene was formed as squares with 500 × 500 nm^2. The space gap between the graphene squares is 500 nm. The same

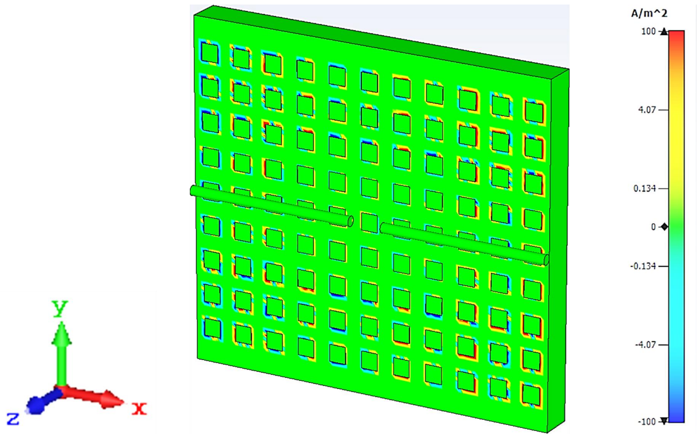

FIGURE 7.7: The CST simulation results of the generated current density of the hybrid nanoelectrodes (500 × 500 nm^2 graphene islands and 300 nm nanowire).

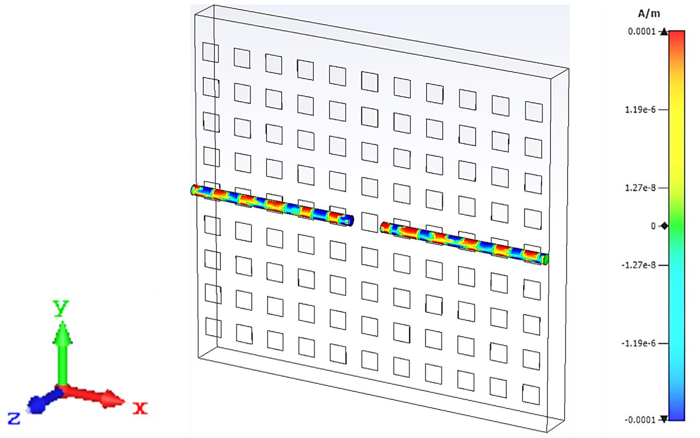

FIGURE 7.8: The CST simulation results of the surface current of the hybrid nanoelectrodes (500 × 500 nm^2 graphene islands and 300 nm nanowire).

configuration was used for the simulation, see Figure 7.5. The simulation results have a good agreement with the theory, the bigger the space gap between the graphene squares the less the electric field enhancement can be served. The 500 × 500 nm^2 graphene squares show a maximum electric field of 0.22 V/cm between the squares, as shown in Figure 7.6. However, the electric field between the squares is higher by 7 times than the electric field between conventional interdigitated fingers. Therefore, the reduction in the electric field enhancement between the graphene squares rather than graphene flakes is still acceptable. The high transparency of the graphene squares provides a maximum current density of 11.8 $\mathrm{A/cm}^2$, see Figure 7.7. On the other hand, the bigger the graphene area connecting the nanowire the higher the surface current flow can be achieved. The simulation results show the maximum surface current of 148×10^{-6} A/cm flowing between the graphene squares and Ag-NW, as shown in Figure 7.8, which is higher than the surface current between the

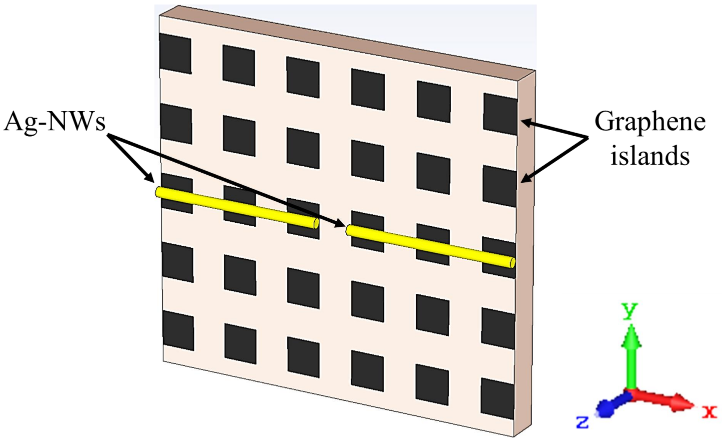

FIGURE 7.9: The simulated layout of the hybrid nanoelectrodes based on 1 × 1 μm^2 graphene islands and 300 nm Ag-NWs.

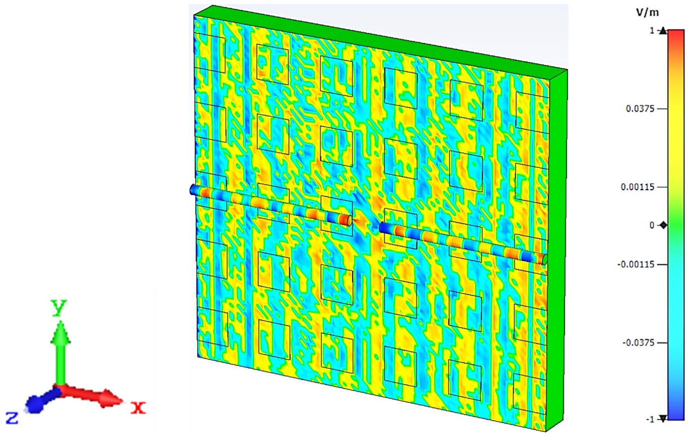

FIGURE 7.10: The CST simulation results of the generated electric field between the nanoelectrodes (1 × 1 μm^2 graphene islands and 300 nm Ag-NWs).

graphene flakes and Ag-NW.

7.2.3 1 × 1 μm^2 Graphene and 300 nm Nanowire

The fabrication of graphene squares with 500 × 500 nm^2 is not possible and needs a lot of optimization because of the properties of the photoresist material. Therefore, graphene squares of 1 × 1 μm^2 with 1 μm of space gap between the graphene squares was designed to compare the electric field, current density, and surface current enhancements. Figure 7.9 show the new hybrid graphene squares and Ag-NW nanoelectrodes design. The simulation results show a maximum electric field of 0.2 V/cm, a maximum current density of 12 A/cm^2, and a maximum surface current of 170 × 10^{-6} A/cm as shown in figures 7.10, 7.11, and 7.12, respectively. The reduction in the value of the enhanced electric field and is attributed to the big space gap between graphene squares. On the other hand, the big size of the squares which

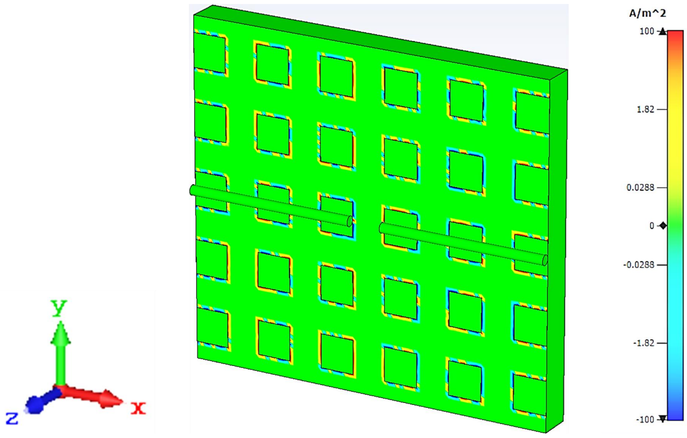

FIGURE 7.11: The CST simulation results of the generated current density of the hybrid nanoelectrodes ($1 \times 1\ \mu m^2$ graphene islands and 300 nm Ag-NWs).

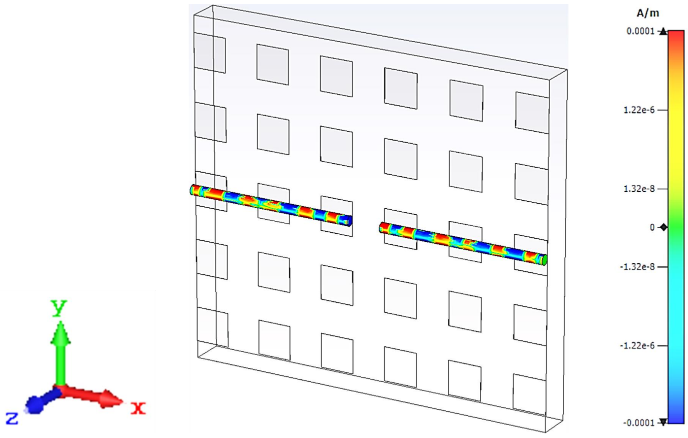

FIGURE 7.12: The CST simulation results of the surface current of the hybrid nanoelectrodes ($1 \times 1\ \mu m^2$ graphene islands and 300 nm Ag-NWs).

touches the Ag-NW provides an increase in the value of the surface current flow between the graphene squares and Ag-NW. Table 7.1 shows a summery of the CST simulation results for hybrid nanoelectrodes using various graphene configurations.

7.3 Hybrid Nanoelectrodes Photomixer Fabrication

The hybrid nanoelectrodes photomixers fabrication is classified into two categories according to the graphene types. In the first group, the hybrid nanoelectrodes are based on nitrogen-doped single-layer graphene (N^+SLG) flakes (lateral size 0.5-5 μm, obtained from ACS Material LLC.) and 300 nm Ag-NW [77]. In the second group, the hybrid nanoelectrodes are based on multilayer graphene islands and 120 nm or 300 nm Ag-NW.

TABLE 7.1: Comparison of the CST simulation results for the hybrid nanoelectrodes using various graphene configurations.

	Hybrid nanoelectrodes based on Ag-NW and		
	100×100 nm^2 graphene flakes	**500×500 nm^2 graphene islands**	**1×1 μm^2 graphene islands**
Electric field (V/cm)	0.295	0.22	0.2
Current density (A/cm^2)	13	11.8	12
Surface current flow (A/cm)	133×10^{-6}	148×10^{-6}	170×10^{-6}

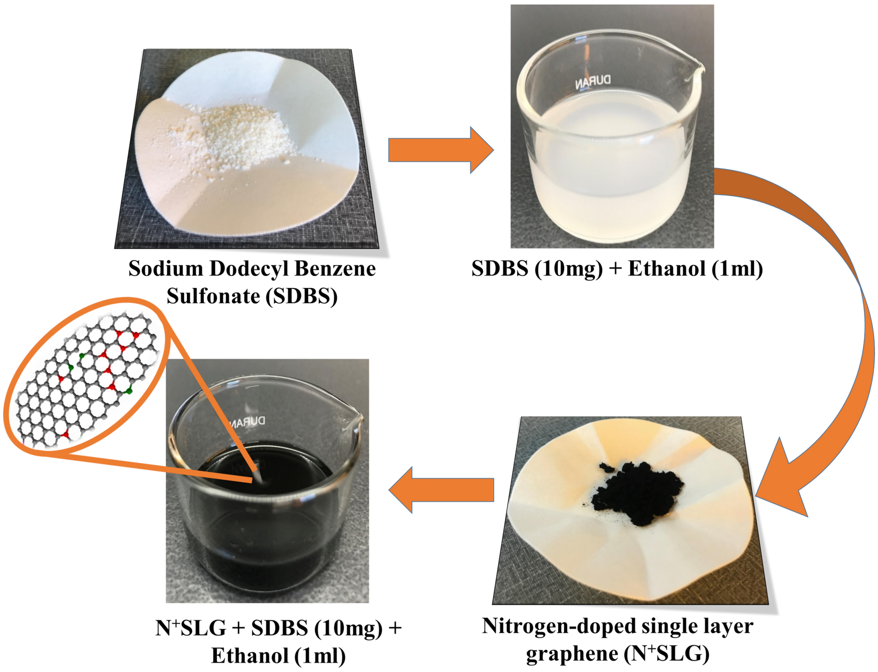

FIGURE 7.13: Dispersed graphene flakes in the solvent liquid.

7.3.1 Hybrid Nanoelectrodes Based on Ag-NW and Graphene Flakes

The fabrication of the THz hybrid nanoelectrodes photomixer based on Ag-NW and graphene flakes are a little bit different from the multilayer graphene photomixer. For this type of photomixer, firstly, a log-periodic antenna was formed on top of the LTG-GaAs wafer using a standard optical lithography process. Then, the antenna was fabricated by evaporating Ti(25 nm) and Au(150 nm). Secondly, N$^+$SLG flakes were dispersed in ethanol with a dispersion aid [Sodium Dodecyl Benzene Sulfonate (SDBS)] with the properties 0.1 mg, 1 ml, and 10 mg, respectively. Thirdly, this

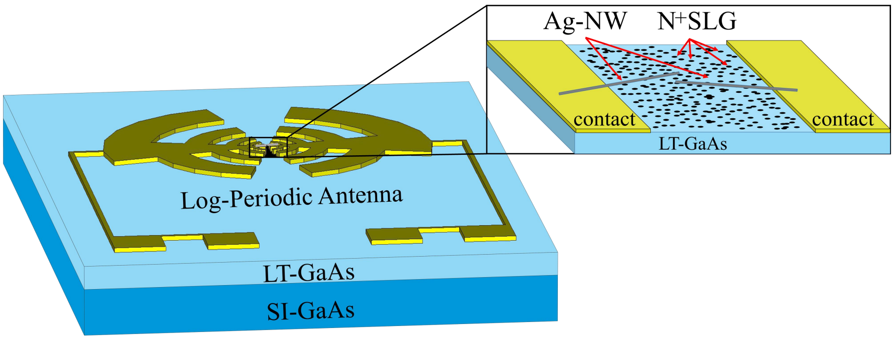

FIGURE 7.14: Schematic diagram of the photomixer with hybrid electrodes (N^+SLG/Ag-NW) on LTG-GaAs.

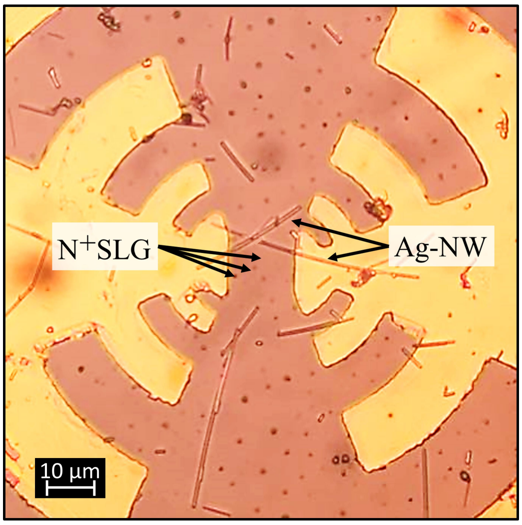

FIGURE 7.15: Optical microscope image of the photomixer with hybrid electrodes (N^+SLG/Ag-NW) on LTG-GaAs.

dispersed graphene was mixed with Ag-NW (∅ 300 nm). Few drops of the mixed solution were applied in the antenna gap to deposit the graphene flakes in random positions and the nanowire was randomly aligned to perform as nanoelectrodes between the antenna contacts. Figures 7.13 shows the dispersed method of the graphene flakes in the solvent liquid. Figures 7.14 and 7.15 the schematic diagram and the microscope image of the hybrid nanoelectrodes photomixer based on N^+SLG and Ag-NW on LTG-GaAs. However, controlling the fabrication of small gaps (in the range of 100 nm) between the graphene flakes is impossible since the location of the graphene flakes and the Ag-NW are located randomly. Therefore, an optimized gap between the graphene can result in optimum field enhancements and higher THz signal powers. The gap between graphene could be optimized by using multilayer graphene instead of graphene flakes and patterning the multilayer graphene into graphene islands.

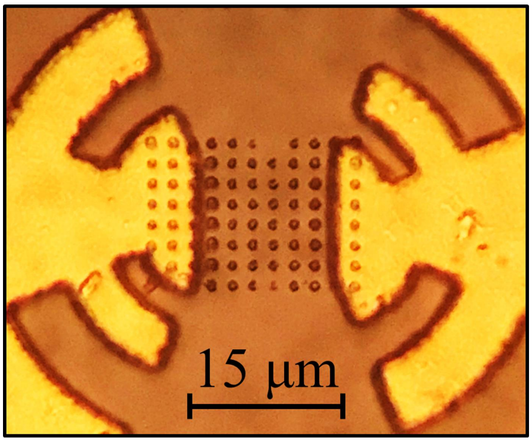

FIGURE 7.16: Optical microscope image of the photomixer with graphene islands.

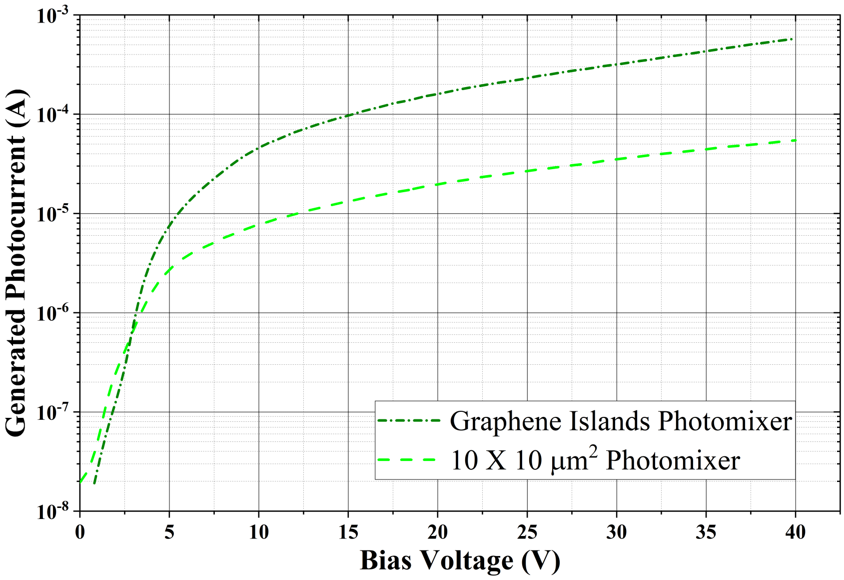

FIGURE 7.17: Comparison of the generated photocurrent for the photomixer with and without graphene islands.

7.3.2 Hybrid Nanoelectrodes Based on Ag-NW and Graphene Islands

The fixed location for the graphene is extremely important to enhance the plasmonic effect between the nano components. For this problem, forming graphene islands using a standard optical lithography process was proposed. From table 7.1, hybrid nanoelectrodes based on Ag-NW and 1×1 μm^2 graphene squares is considered a reasonable configuration to be fabricated. The fabrication of the hybrid nanoelectrodes based on Ag-NW and graphene islands can be done by two major steps:

1. Graphene Islands Fabrication

The fabrication of the graphene islands is not different than the fabrication of the interdigitated graphene fingers, detailed in section 4.3, except that there is no SiNx layer on top of the chip. Figure 7.16 shows an optical microscopic image of the photomixer with photoresist on top of the $1 \times 1\ \mu m^2$ graphene islands. The effect of the islands in the active region was tested by a DC characterization method. The DC measurement was compared with an open gap photomixer. Figure 7.17 shows the comparison of the generated photocurrent for photomixer with and without graphene islands. The photomixer with graphene islands exhibits a maximum generated photocurrent of 0.578 mA, which is one order higher photocurrent than that of the open gap photomixer (0.0546 mA). The enhancement in the generated photocurrent is attributed to the reduced transport path for the generated photocarriers.

2. Ag-NW Alignment

Industrial Ag-NWs were purchased from ACS Material LLC. [77]. Two diameters ($\varnothing = 120$ nm and 300 nm) were investigated with graphene islands as hybrid nanoelectrodes. The Ag-NWs were dispersed in ethanol. Placement under the microscope method was used for the Ag-NWs distribution and alignment. Where a drop of ethanol with Ag-NWs is placed very close to the active region of the photomixer using a thinned toothpick. This step is very critical, therefore, an optical microscope was used to avoid touching the active region. Any contact to the active region by the toothpick will remove the graphene islands. This method is not accurate and a lot of optimization is required to save time and achieve high performance. Figure 7.18 and 7.19 show an optical microscopic image for the hybrid nanoelectrodes photomixer using Ag-NW with a diameter of 120 nm and 300 nm, respectively.

7.4 DC Measurement Results

The DC characterization for the hybrid nanoelectrodes photomixers was measured using the setup in Figure 4.10. The measurement results were compared with the DC characterization of a conventional interdigitated photomixer.

1. Hybrid nanoelectrodes Based on Ag-NW and Graphene Flakes

The hybrid nanoelectrodes photomixer, shown in Figure 7.15, was characterized using a total optical beat power of 28 mW to illuminate the active area of the photomixer. On the other hand, the bias voltage varied from 0 - 15 V. The DC characterization of the hybrid nanoelectrodes photomixer, shown in

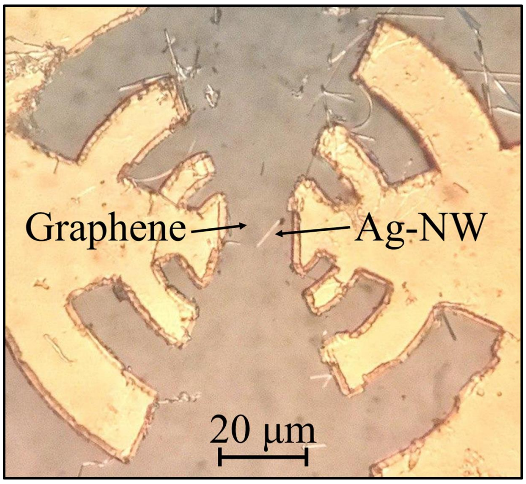

FIGURE 7.18: Optical microscopic image of the hybrid nanoelectrodes photomixer using 120 nm Ag-NW.

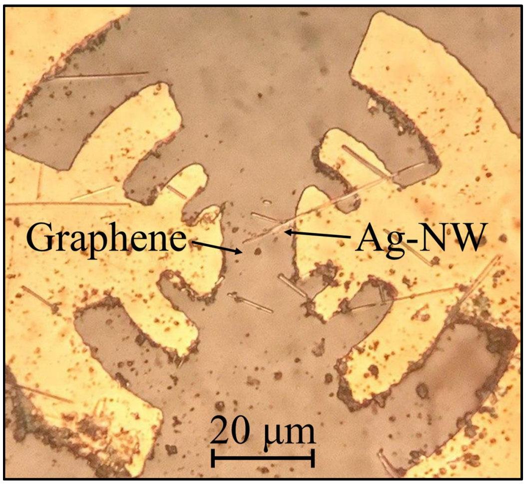

FIGURE 7.19: Optical microscopic image of the hybrid nanoelectrodes photomixer using 300 nm Ag-NW.

Figure 7.20, showed a highly reliable maximum photocurrent of ∼ 1.8 mA, a small dark current of 90 nA, and an on/off ratio of more than four orders of magnitude as reported in [111].

The DC measurement results were compared to a conventional photomixer with interdigitated metal finger electrodes using the same conditions above. The conventional photomixer showed a maximum generated photocurrent of 260 μA before local heating damages the device at 15 V. The hybrid nanoelectrodes showed an increase of the maximum achievable photocurrent under reliable conditions by more than 7 times due to the improved conductivity. Figure 7.21 shows a comparison of the DC characteristic between the hybrid

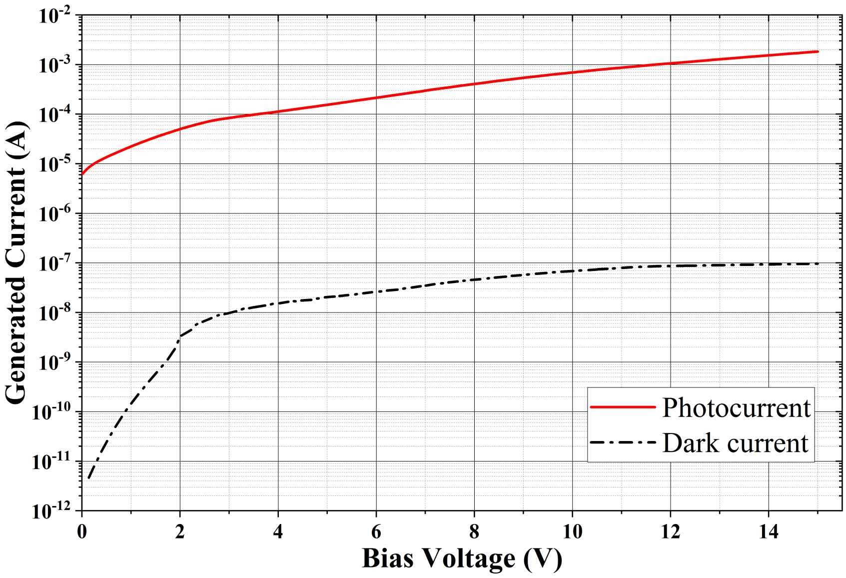

FIGURE 7.20: DC caharactrization of the photomixer with hybrid electrodes (N^+SLG/Ag-NW).

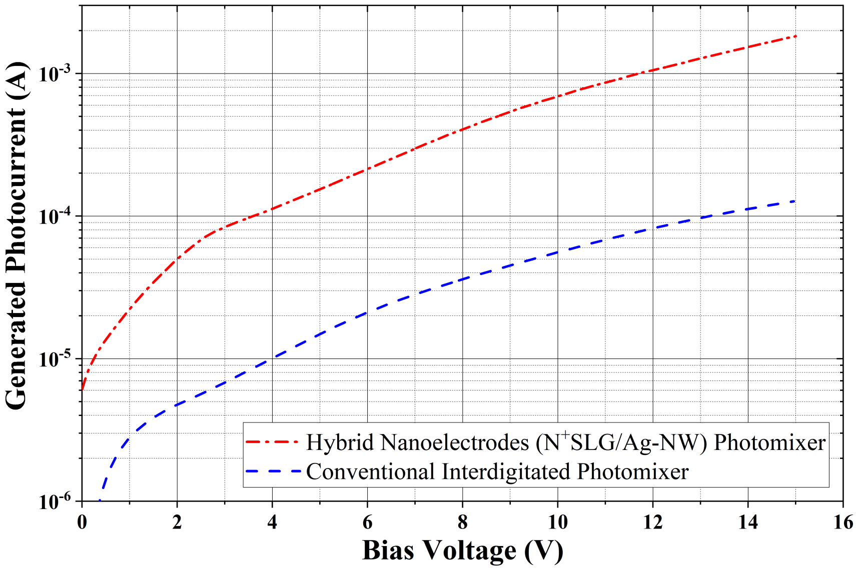

FIGURE 7.21: DC caharactrization of the photomixer with hybrid electrodes (N^+SLG/Ag-NW).

nanoelectrodes photomixer and the conventional interdigitated metal finger electrodes photomixer.

2. Hybrid Nanoelectrodes Based on Graphene Islands and 120 nm Ag-NW

The active area of the photomixer was illuminated with a total optical power of 30 mW. The dark and the generated photocurrents of the device were measured by varying the bias voltage from 0 V to 40 V. the measurement results showed a maximum photocurrent of 2.58 mA, a small dark current of ~ 25 nA, and an

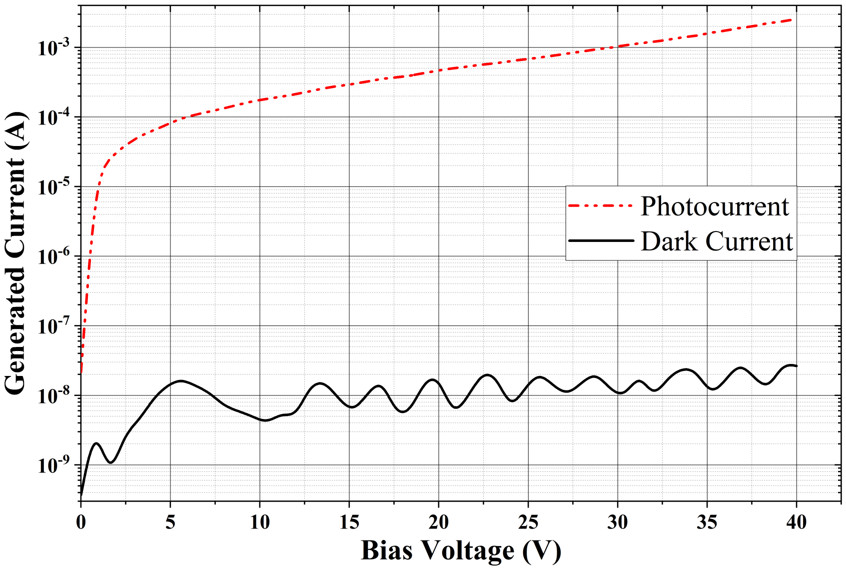

FIGURE 7.22: DC caharactrization of the hybrid nanoelectrodes based on 1 × 1 μm^2 graphene islands and 120 nm Ag-NWs.

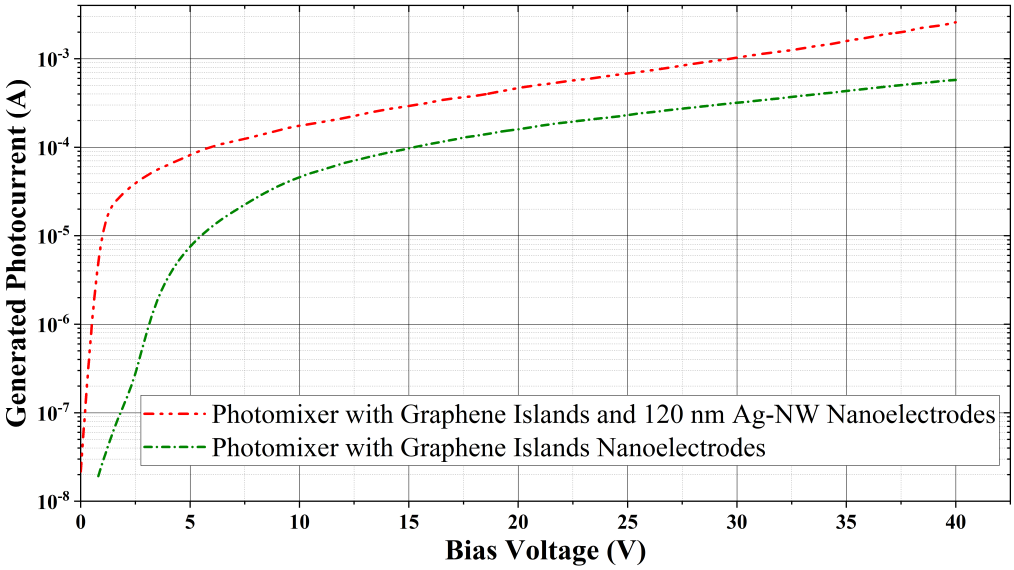

FIGURE 7.23: Comparison of the generated photocurrent for the photomixer with hybrid nanoelectrodes based on 1 × 1 μm^2 graphene islands and 120 nm Ag-NWs and the photomixer with graphene islands.

on/off ratio of more than five orders of magnitude, as shown in Figure 7.22. The generated photocurrent of the hybrid nanoelectrodes photomixer was compared with that of the photomixer with graphene islands. It is very clear the conductivity of the NW was improved by the conductivity of the graphene islands. Where the generated photocurrent was improved by approximately five times, see Figure 7.23.

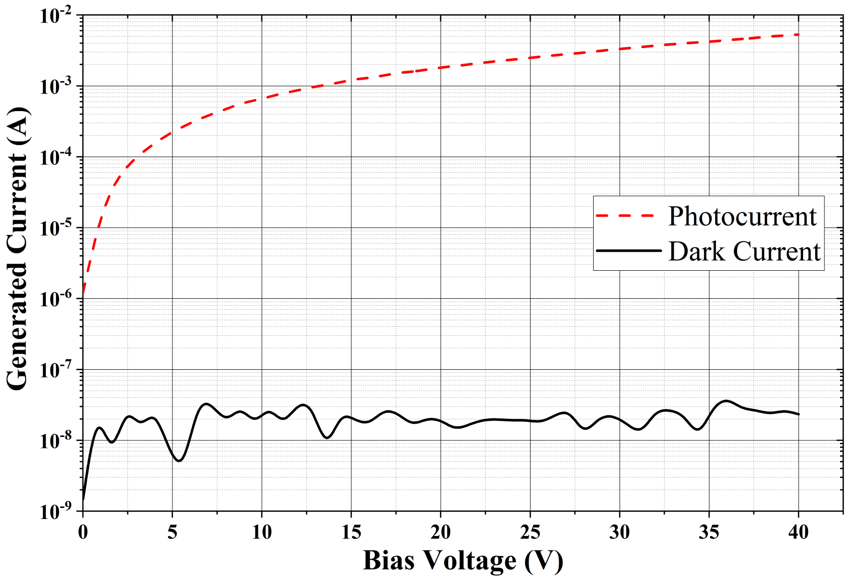

FIGURE 7.24: DC caharactrization of the photomixer with hybrid nanoelectrodes based on 1 × 1 μm^2 graphene islands and 300 nm Ag-NWs.

3. Hybrid Nanoelectrodes Based on Graphene Islands and 300 nm Ag-NW

The 120 nm Ag-NW was replaced by a 300 nm Ag-NW. The various diameter size affects directly the capability of the NW to handle higher currents. The higher the diameter the less the flow resistance, which leads to a higher current flowing. The effect of the various diameter was investigated by measuring the DC characterization for hybrid nanoelectrodes photomixer based on 300 nm Ag-NW and graphene islands. The measurement results showed a maximum photocurrent of 5.3 mA, a small dark current of 26 nA, and an on/off ratio of approximately five orders of magnitude, as shown in Figure 7.24. The generated photocurrent of the hybrid nanoelectrodes photomixer showed one order higher generated photocurrent as compared with that of the photomixer with graphene islands. This increase in the generated photocurrent by using the 300 nm Ag-NW instead of the 120 nm Ag-NW is attributed to the bigger diameter of the NW, which allows higher current flowing per cross-section, see Figure 7.25. Consequently, the higher the flowing generated photocurrent the higher the radiated THz power will become.

Furthermore, the DC measurement showed that the generated photocurrent of the photomixer with hybrid nanoelectrodes based on 1 × 1 μm^2 graphene islands and 300 nm Ag-NWs is twice higher than the generated photocurrent of the interdigitated graphene photomixer, as shown in Figure 7.26. This indicates that the hybrid nanoelectrodes photomixer based on 1 × 1 μm^2

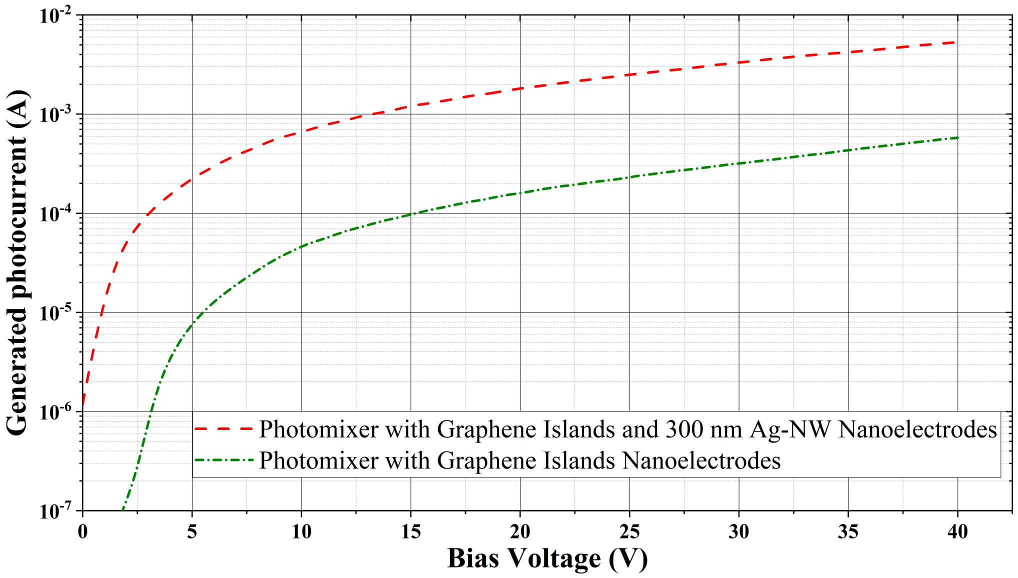

FIGURE 7.25: Comparison of the generated photocurrent for the photomixer with hybrid nanoelectrodes based on 1 × 1 μm^2 graphene islands and 300 nm Ag-NWs and the photomixer with graphene islands.

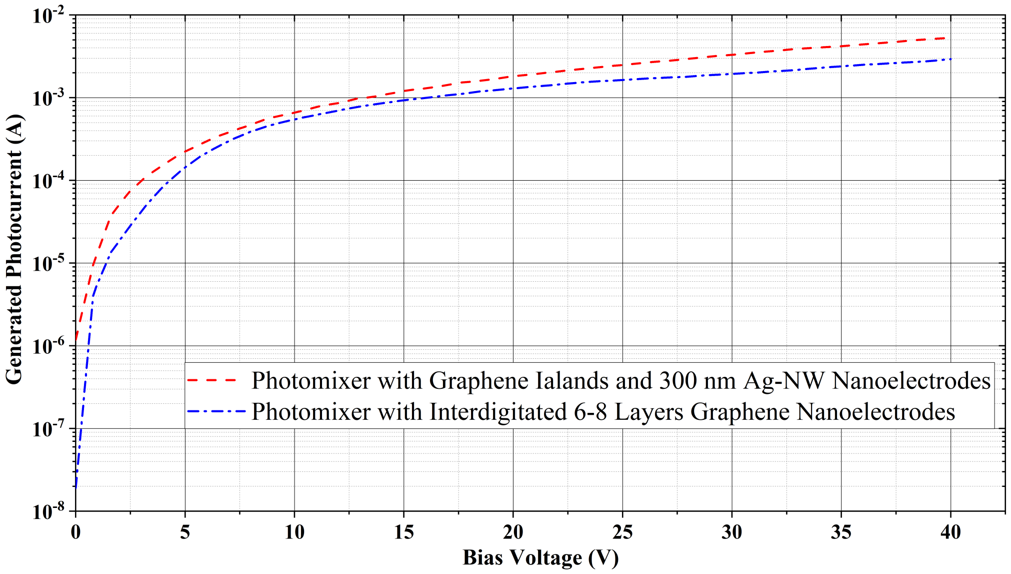

FIGURE 7.26: Comparison of the generated photocurrent for the photomixer with hybrid nanoelectrodes based on 1 × 1 μm^2 graphene islands and 300 nm Ag-NWs and the interdigitated photomixer with 6-8 layers graphene.

graphene islands and 300 nm Ag-NWs can radiate a higher THz output signal than the interdigitated graphene photomixer due to the combined benefits of the nanocomponents.

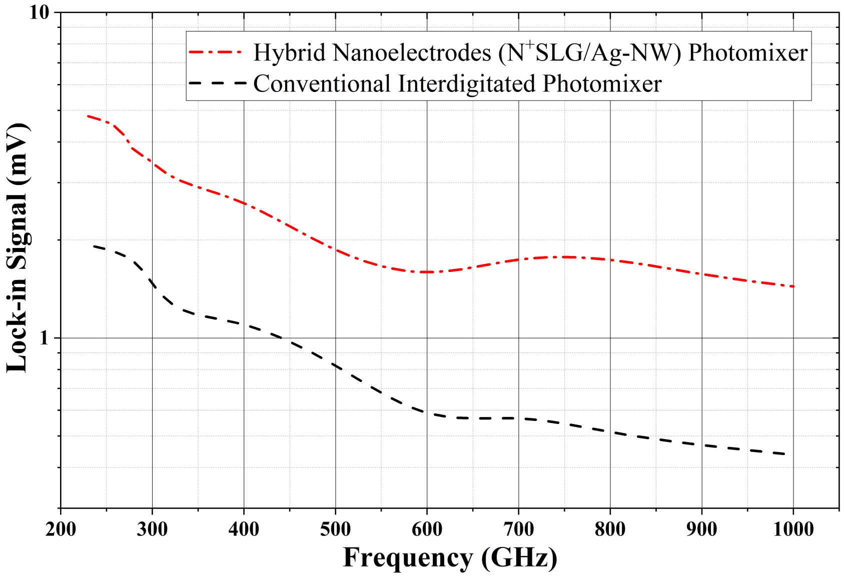

FIGURE 7.27: Comparison of the THz output signal measurement of the photomixer with hybrid electrodes (N^+SLG/Ag-NW) and a conventional interdigitated metal photomixer.

7.5 THz Signal Measurements and Results

1. Hybrid nanoelectrodes Based on Ag-NW and Graphene Flakes

The setup in Figure 4.10 was used to measure the THz output signal of the hybrid nanoelectrodes photomixer. The range between 200 GHz and 1 THz was covered by changing the frequency difference between the two DFB-LDs. The same total beat signal of the DC characterization was used to illuminate the active area. The generated photocarriers were accelerated by applying a bias voltage of 14 V between the photomixer contacts.

As expected from the results of the DC measurements, a significant improvement is obtained in the THz measurement results due to the use of hybrid electrodes instead of the interdigitated metal finger electrodes. The lock-in signal level is clearly increased for the whole THz measurement range (see Figure 7.27).

Figure 7.28 shows how much the performance was improved over the entire measurement range for THz photomixer by using graphene flakes and Ag-NW as hybrid nanoelectrodes instead of conventional metal electrodes. The hybrid nanoelectrodes photomixer shows more than twice at the low frequencies and a factor of more than three times at high frequencies higher THz output signal than what can be obtained by the conventional interdigitated photomixer. The

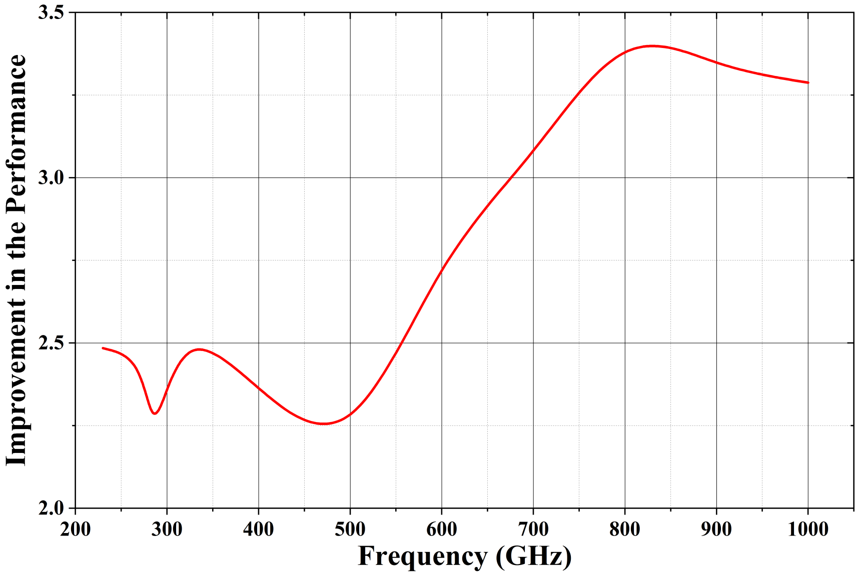

FIGURE 7.28: The ratio of the performance of the photomixer with hybrid electrodes (N^+SLG/Ag-NW) and a conventional interdigitated metal photomixer over the whole spectral range of the measurement.

increase in the THz output signal allows for the photomixer to operate the broadband THz source for much broader frequencies than that of the conventional interdigitated photomixer under the same antenna specifications.

The increase in the generated photocurrent leads to an increase in the THz output signal for the hybrid nanoelectrodes photomixer by a factor of more than twice at low frequencies and more than three times at high frequencies than the conventional interdigitated photomixer. This increase in the relative output power allows the new photomixer with a hybrid nanoelectrodes photomixer to operate for a broader range of frequencies. The enhancement in the generated photocurrent and measured THz signal is attributed to the transparency of the graphene, which increases the illuminated area and improves the optical conversion efficiency. Besides the increased number of photogenerated carriers, the field enhancement between graphene flakes allowed the fast carrier drift to the Ag-NW. The small contact area of the NW electrodes leads to higher THz power and increased cut-off frequencies. Furthermore, NWs also provide the capability to handle higher currents without damaging the device.

2. Hybrid Nanoelectrodes Based on 1 × 1 μm^2 Graphene Islands and Ag-NW

A total optical beat power of 30 mW was used to illuminate the active area of the hybrid nanoelectrodes photomixers, while a bias voltage of 15 V was applied

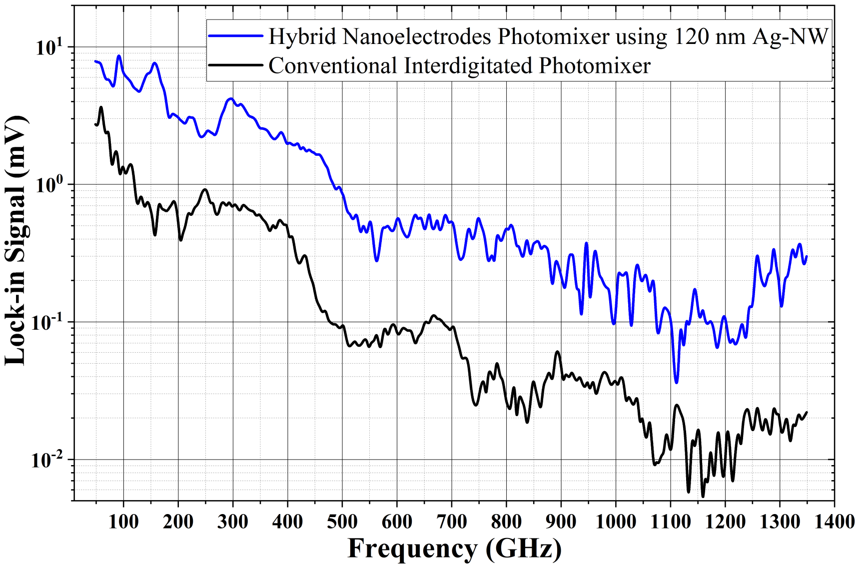

FIGURE 7.29: Comparison of the THz output signal for the photomixer with hybrid nanoelectrodes based on 1 × 1 μm^2 graphene islands and 120 nm Ag-NWs and the conventional interdigitated photomixer.

between the antenna contact to accelerate the generated photocarriers. The performance of each photomixer was compared with a conventional interdigitated photomixer. The measurement scan was performed using the python program with 5 GHz frequency steps to obtain a highly accurate measurement.

The hybrid nanoelectrodes photomixer, which consists of 120 nm Ag-NW and graphene islands, shows approximately one order higher relative output power than that of the conventional interdigitated photomixer, as shown in Figure 7.29. On the other hand, the hybrid nanoelectrodes photomixer based on 300 nm Ag-NW and graphene islands shows more than one order higher relative output power in comparison with that of the conventional interdigitated photomixer, as shown in Figure 7.30. The enhancement of the relative output power of the hybrid nanoelectrodes photomixer is attributed to the high transparency and conductivity of graphene, which combined with the high capability of the Ag-NW to handle very high current densities despite the small size of the Ag-NW. As the simulation predicted, the local recombination of the graphene islands reduces the transport path of the generated photocarriers and reduces the carrier lifetime. Furthermore, the local plasmonic field around the graphene islands creates good sources of generated photocarriers resulting in high drift current densities. Additionally, the big size of the islands which touch the Ag-NW provides an increase in the value of the surface current

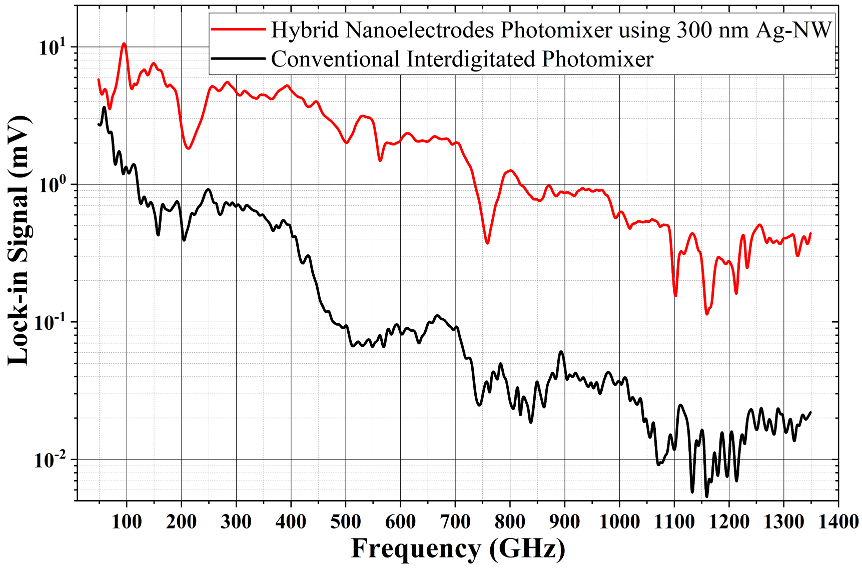

FIGURE 7.30: Comparison of the THz output signal for the photomixer with hybrid nanoelectrodes based on 1 × 1 μm^2 graphene islands and 300 nm Ag-NWs and the conventional interdigitated photomixer.

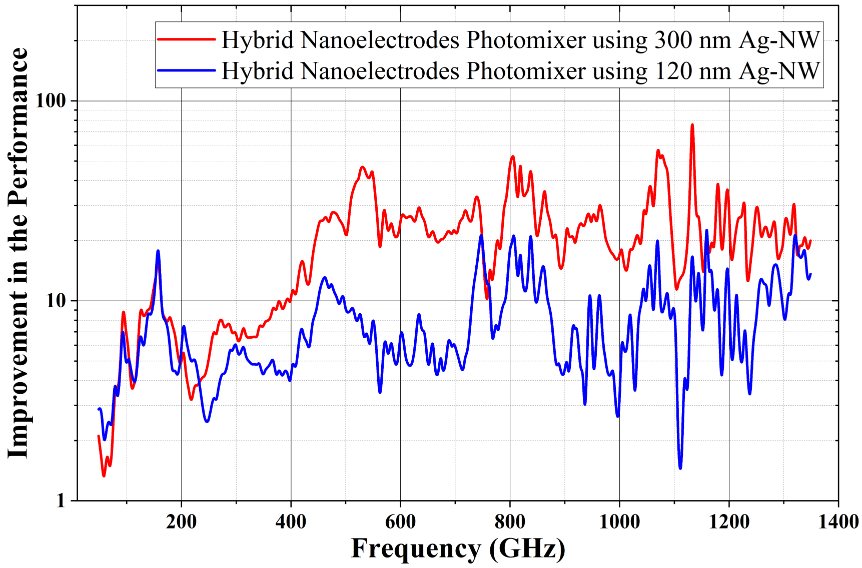

FIGURE 7.31: The ratio of the performance of the hybrid nanoelectrodes photomixer using Ag-NW ($\varnothing = 120$ nm) and ($\varnothing = 300$ nm), and a conventional interdigitated metal photomixer over the whole spectral range of the measurement.

flow between the graphene islands and Ag-NW. In this sense, The drifted current will be captured spontaneously by the Ag-NW due to the presence of the SPP of the Ag-NW. Therefore, the Ag-NW serves as a highly capable transport waveguide for the high current densities and increases the irradiated THz wave.

Figure 7.31 shows the ratio of the performance of each hybrid nanoelectrodes photomixer to the performance of the conventional interdigitated photomixer.

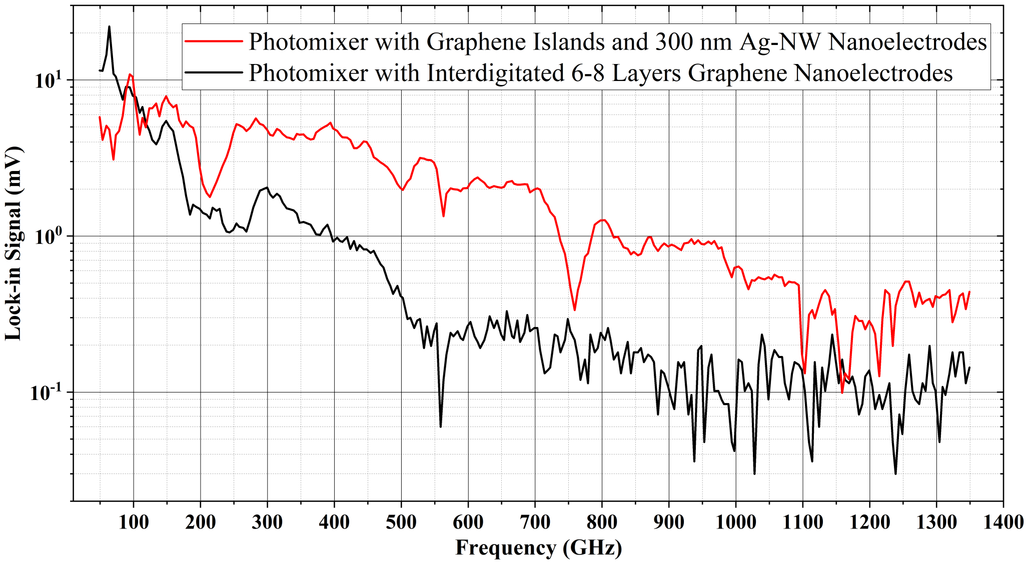

FIGURE 7.32: Comparison of the THz output signal for the hybrid nanoelectrodes photomixer using Ag-NW (∅ = 300 nm) and the interdigitated 6-8 layers graphene photomixer.

Additionally, Figure 7.31 shows how much the performance was improved over the entire measurement range for THz photomixer by using various Ag-NWs and graphene islands as hybrid nanoelectrodes instead of conventional metal electrodes. Because of the higher capability of the Ag-NW with a diameter of 300 nm than the Ag-NW with a diameter of 120 nm, the hybrid nanoelectrodes photomixer, which consists of Ag-NW with a diameter of 300 nm and graphene islands, shows higher output power than its competitor.

The measured THz signal of the hybrid nanoelectrodes photomixer based on $1 \times 1\ \mu\text{m}^2$ graphene islands and 300 nm Ag-NW was compared with the Measured THz signal of the interdigitated 6-8 layers graphene photomixer. The THz signal of the hybrid nanoelectrodes photomixer based on $1 \times 1\ \mu\text{m}^2$ graphene islands and 300 nm Ag-NW is one order of magnitude higher than the THz signal of the interdigitated 6-8 layers graphene photomixer, especially between 500 GHz to 1 THz, as shown in Figure 7.32. This enhancement in the device radiation is attributed to the optical and electrical properties of graphene and Ag-NW. The high transparency and conductivity of graphene allow generation and drift off more vectors into Ag-NW. While the Ag-NW provides a high capability to handle the high current density, which results in high output radiated THz power.

7.6 Summary

The measurement results of THz photomixers with hybrid nanoelectrodes based graphene and an Ag-NWs material have shown unique properties and a high potential for advance THz sources. Due to the high transparency of graphene, a high number of photocarriers can be generated. Graphene islands of good dimensions design enhance, on one hand, the electric field by reducing the mean free path of the generated photocarriers and reduce the carrier transit time. On the other hand, enhances the surface current flow, which allows the photocarriers to be captured easily by the Ag-NW nanoelectrodes. Ag-NWs, Despite their very small physical diameters, provide a significant capability to handle high drifted current densities. The measurement results have shown that a high generated photocurrent of 2.58 mA can be reached for the hybrid nanoelectrodes photomixer based on Ag-NW ($\varnothing = 120$ nm) and $1 \times 1\ \mu m^2$ graphene islands. The high generated photocurrent enables the device to radiate approximately more than one order of magnitude of relative THz power higher than that of the conventional interdigitated photomixer. Additionally, the measurement results have also shown that the various diameters for the Ag-NW nanoelectrodes affect directly the capability of the NW to handle even higher photocurrents. Where the higher the generated photocurrent the higher the radiative THz wave. The hybrid nanoelectrodes photomixer based on Ag-NW ($\varnothing = 300$ nm) and $1 \times 1\ \mu m^2$ graphene islands has shown a maximum reliable photocurrent of 5.3 mA, which allows 50 times higher radiative the THz power than the conventional interdigitated photomixer. Furthermore, the hybrid nanoelectrodes photomixer based on $1 \times 1\ \mu m^2$ graphene islands and 300 nm Ag-NW has shown an even higher THz signal than that of the interdigitated 6-8 layers graphene photomixer. The hybrid nanoelectrodes photomixer based on $1 \times 1\ \mu m^2$ graphene islands and 300 nm Ag-NW has shown one order of magnitude higher than the THz signal of the interdigitated 6-8 layers graphene photomixer. The measurement results have a good agreement with the simulation results. Further fabrication optimization, opens a door to fabricate good THz sources based on photomixers using nanomaterials.

Chapter 8

Conclusion and Outlook

Terahertz photomixers with nanoelectrodes based on graphene or hybrid nanoelectrodes based on graphene and Ag-NW were investigated in this work. The work in this dissertation was divided into three groups, depending on the function of the fabricated THz photomixer.

The first group has concerned with fabricating THz sources dependent on photomixer devices. These photomixers were fabricated using graphene with a various number of layers in various nanoelectrodes designs. Simulation and measurement results have confirmed that the THz photomixers with graphene nanoelectrodes are far superior to the conventional interdigitated competitors in general, where the high transparency of graphene material affects directly on the number of generated photocarriers and increase the generated photocurrent. Furthermore, the high thermal conductivity of graphene allows the generated optically and electrically local heat in the small active area of the photomixer to dissipate into the large antenna material. Lateral heat dissipation of the graphene material improves the reliability of the devices. The device reliability was shown by the standing devices under a high bias voltage.

Nanoelectrodes design has an essential influence on the value of the generated photocurrent and the radiative THz power. Numerical and simulation calculations showed that reducing the nanoelectrodes width reduces the device capacitance. The 2D graphene nanoelectrodes photomixers with 1 μm single gap in 5×5 μm^2 active area have half of the device capacitance of 2D graphene nanoelectrodes photomixers with 1 μm single gap in 10 × 10 μm^2 active area. Accordingly, they exhibit three times higher photocurrent and one order of magnitude higher THz output signal than that of the 2D graphene nanoelectrodes photomixers with 1 μm single gap in 10 × 10 μm^2 active area. The 2D graphene nanoelectrodes photomixers with 1 μm single gap in 5 × 5 μm^2 active area show one order on magnitude higher photocurrent and more than one order of magnitude higher THz output signal as compared with the photocurrent and THz output power of the conventional interdigitated photomixers in the entire measurement range.

On the other hand, Interdigitated graphene photomixers exhibit higher photoconductive gain because of the shorter transport time required for the carriers to travel from a finger to another. This leads to generating a higher photocurrent than the 10 × 10 μm^2 active area of 2D graphene photomixers with the same antenna design. According to the increase in the generated photocurrent, the interdigitated graphene photomixers have shown twice relative THz output power higher than that of the 10 × 10 μm^2 active area of 2D graphene photomixers.

The electrical (sheet resistance) and optical (transparency) properties of the multilayer graphene depend on the number of graphene layers, which affects directly the performance of the photomixer. The higher the transparency of thinner graphene the higher the illuminated effective area, the higher the number of generated photocarriers. However, a thicker graphene layer is required to carry high current density and enhance performance and manufacturing reliability. In this sense, the DC characterization demonstrates that the 3-5 layers graphene exhibits higher transparency than 6-8 layers graphene, but the 6-8 layers graphene showed a preference to handle higher current densities, which shown at a higher bias field. Interdigitated graphene photomixer using 6-8 layers graphene showed a higher THz output signal than the THz output signal of the same interdigitated graphene photomixer using 3-5 layers graphene under a high bias field (15 V), which is one order of magnitude higher than the THz output signal of the conventional interdigitated photomixer.

The second group of THz photomixer has concerned with fabricating THz photodetectors based on interdigitated graphene nanoelectrodes. The high transparency of graphene increases the number of generated photocarriers, which are modulated by the THz induced bias field. The measurement results have shown great enhancement of THz detection using a photomixer with interdigitated graphene nanoelectrodes instead of metal electrodes. The interdigitated graphene photomixer has detected more than one order of magnitude higher THz induced photocurrent than that of the conventional interdigitated photomixer. Furthermore, due to the use of the graphene nanoelectrodes, the graphene photomixer receiver was able to detect twice the spectral range of the detected THz beam by the conventional interdigitated photomixer.

The final group of this work was concerned with the use of combined nanomaterials as hybrid nanoelectrodes to enhance the performance of the photomixer. The hybrid nanoelectrodes were based on Ag-NWs with various dimensions and various types of graphene materials. Besides the increased photocurrent due to the high transparency of graphene, the high electrical conductivity of graphene enhances the transportation of the generated photocurrent into the Ag-NW. Despite the low fill factor of the Ag-NW nanoelectrodes provide the capability of handling rather high currents, leading to high THz output signals. Simulation results have shown a great improvement in the nanoelectrodes conductivity and surface current flow utilizing graphene and Ag-NW as hybrid nanoelectrodes. Hybrid nanoelectrodes photomixers have shown more than one order higher THz output signal. The increase in the THz output signal of the hybrid nanoelectrodes photomixer as a THz source indicates that the hybrid nanoelectrodes photomixer can operate in higher frequency ranges compared to the conventional interdigitated photomixer.

The simulation and measurement results for all groups indicate that the THz photomixers with nanoelectrodes have a better performance than the conventional interdigitated photomixers in general. This preferable performance of the nanoelectrodes photomixer opens the door to employ these photomixers in the many applications of interest in sensing, security, imaging, and many others.

This work opens new research directions in THz photomixers using the nanoelectrodes which can be improved and optimized further. Some of the suggested future work is summarized here:

1. **New graphene transfer method** The graphene transfer method is a simple technology to place the graphene layer on another host substrate. However, the method is not accurate and does not guarantee the same surface homogeneity and adhesion to the new substrate. Additional investigations on the graphene transfer technique will improve the device's reliability furthermore. The optimization of the surface homogeneity and the adhesion of the graphene will allow an advanced design for graphene-based plasmonic enhancements.

2. **New graphene nanoelectrodes configurations** Various graphene nanoelectrodes configurations illustrated in this dissertation have led to a significant difference in the performance of nanoelectrodes photomixers from several aspects. New configuration designs combine high optical/electrical conversion, plasmonic light confinement, and higher obtainable photoconductive gain. Different interdigitated fingers with different space gaps, such as using eight fingers, or using comp configuration, enhance the light confinement and increase the obtained photoconductive gain.

3. **New hybrid nanoelectrodes configurations** Using various graphene matrices to enhance the plasmonic designs. The graphene matrix with various squares or circles with various space gaps will confine the laser intensity and enhances the drifting it into NW nanoelectrodes.

4. **Optimization of the nanowire disposition** The nanowire alignment can still be optimized for better control of nanowire type, size, and position. This can be investigated using dielectrophoresis, optical tweezer, or other methods. The alignment control is essential for advanced hybrid configurations, such as multiple nanowire alignment with graphene islands in a very precise and accurate position.

5. **Using graphene as an active material** Design and implement THz sources and detectors using graphene as an active material. Active graphene enhances supporting tightly confined propagation of THz signals, with tailored phase velocity and characteristic impedance, and increases the compactness of the THz devices.

6. **New antenna design** Different broadband antenna designs can be investigated to modify the nanoelectrodes' dimension and location in the photomixer. The advantage of the dimension of the nanoelectrodes can be used to extend the antenna operating frequency.

7. **Various laser sources and photoconductive materials** Investigate the nanoelectrodes photomixer performance using the telecom laser wavelength 1550 nm with respective active material like ErAs:GaAs.

8. **pulse operation system** Investigate the performance of the nanoelectrodes photomixer using pulse operation. The light confinement and the optical/electrical conversion of the new nanomaterials photomixer can improve the characteristics of the pulsed THz sources and detectors for special application.

Acronyms

AFM	Atomic Force Microscopy
Ag-NW	Silver Nanowire
Au	Gold
CNTs	Carbon Nanotubes
CST	Computer Simulation Technology (Simulation software)
CVD	Chemical Vapor Deposition
CW	Continuous-waves
DFB-LDs	Distributed Feedback Laser Diodes
DR	Dynamic range
FIT	Finite integration technique
GaAs	Gallium Arsenide
GHz	Gigahertz
GIs	Graphene islands
GNR	Graphene Nanoribbons
I_{noise}	Noise current
I_{signal}	Signal photocurrent
ITO	Indium tin oxide
LTG-GaAs	Low-temperature-grown GaAs
N$^+$SLG	Nitrogen-doped single-layer Graphene Flakes
Ni	Nikal
PM	Polarization-maintaining Optical Fiber
PMMA	Poly-methyl-methacrylate

RS	Rayleigh Scattering
SDBS	Sodium Dodecyl Benzene Sulfonate
SPP	Surface Plasmon Polaritons
S-TCAD	Silvaco TCAD Software (Simulation software)
TEM	Transmission Electron Microscopy
THz	Terahertz
Ti	Titanium
TTG	Trivial Transfer Graphene
XRD	X-ray Diffraction

Symbols

A	Electrode contact area
A_{act}	Device active area
C	Device capacitance
c	Speed of light (2.99792458×10^{8} m·s^{-1})
d	Total contact length of the photoconductor
E	Electric field of the optical light signal
e	Electron charge (1.60217646×10^{-19} C)
$E_{beat}(t)$	Electric field of the optical beat signal
G_{dark}	Dark conductance
$G_{ph}(t)$	photoconductance
G_r	Generation rate
$G_{total}(t)$	Totat photoconductance
H	Physical thickness of the LTG-GaAs
h	Planck's constant ($6.62607004 \times 10^{-34}$ m^{2}kg/s)
I_{det}	Detected current
$I_{ph}(t)$	Photocurrent
$K(k)$	Complete elliptical integral of the first kind
l	Photocarriers transport path length
L_f	Finger length
m	Mixing efficiency
$n_c(t)$	Photocarriers density
$N_\circ$	Photo flux

ϕ	Phase difference between the two optical signals
$P(t)$	Incident optical beat power
$P_{THz}(t)$	THz power
$R(f)$	Responsivity at a certain chopping frequency
R_A	Antenna resistance
$S_{1,1}$	Reflection coefficient
S_{Ele}	Separation gap between the electrodes
S_g	Spacing gap between the fingers
t	Time
T_{MLG}	Multilayer graphene thickness
T_{SLG}	Singl-layer Graphene thickness
V_{bias}	Bias voltage
V_{det}	Detected voltage
V_{THz}	THz voltage
W_{Ele}	Electrode width
W_f	Finger width
α	Absorption coefficient
Δ_φ	Phase difference between the THz wave and the optical beat
Δf	Frequency difference
Δ_L	Path difference
ε_{eff}	Effective permittivity
ε_0	Absolute permittivity (8.8541878×10^{-12} F·m^{-1})
ε_r	Relative permittivity
η	Quantum efficiency
η_{ab}	Absorption efficiency factor
λ	Wavelength
μ_c	Carrier mobility
ν_{THz}	THz frequancy
$\sigma_{ph}(t)$	Conductivity
τ_c	Carrier lifetime
τ_t	Transit time

ω	Angler frequencies
ω_{THz}	Intermediate freqency signal in THz region

List of Figures

List of Tables

Bibliography

[1] H.-B. Liu, H. Zhong, N. Karpowicz, Y. Chen, and X.-C. Zhang, "Terahertz spectroscopy and imaging for defense and security applications," *Proceedings of the IEEE*, vol. 95, no. 8, pp. 1514–1527, 2007.

[2] S. Hunsche, M. Koch, I. Brener, and M. Nuss, "Thz near-field imaging," *Optics communications*, vol. 150, no. 1-6, pp. 22–26, 1998.

[3] P. H. Siegel, "Terahertz technology in biology and medicine," *IEEE transactions on microwave theory and techniques*, vol. 52, no. 10, pp. 2438–2447, 2004.

[4] B. Jin, C. Zhang, P. Wu, and S. Liu, "Recent progress of terahertz spectroscopy on medicine and biology in china," *Terahertz Sci. Technol.*, vol. 3, no. 4, pp. 192–200, 2010.

[5] J. Bjarnason, T. Chan, A. Lee, M. Celis, and E. Brown, "Millimeter-wave, terahertz, and mid-infrared transmissionthrough common clothing," *Applied Physics Letters*, vol. 85, no. 4, pp. 519–521, 2004.

[6] E. Brown, K. McIntosh, K. Nichols, and C. Dennis, "Photomixing up to 3.8 thz in low-temperature-grown gaas," *Applied Physics Letters*, vol. 66, no. 3, pp. 285–287, 1995.

[7] G. Scalari, C. Walther, M. Fischer, R. Terazzi, H. Beere, D. Ritchie, and J. Faist, "Thz and sub-thz quantum cascade lasers," *Laser & Photonics Reviews*, vol. 3, no. 1-2, pp. 45–66, 2009.

[8] A. Maestrini, J. Ward, J. Gill, H. Javadi, E. Schlecht, G. Chattopadhyay, F. Maiwald, N. R. Erickson, and I. Mehdi, "A 1.7-1.9 thz local oscillator source," *IEEE Microwave and Wireless Components Letters*, vol. 14, no. 6, pp. 253–255, 2004.

[9] F. Sizov and A. Rogalski, “Thz detectors,” *Progress in quantum electronics*, vol. 34, no. 5, pp. 278–347, 2010.

[10] R. Safian, G. Ghazi, and N. Mohammadian, “Review of photomixing continuous-wave terahertz systems and current application trends in terahertz domain,” *Optical Engineering*, vol. 58, no. 11, p. 110901, 2019.

[11] T. Ackemann, M. Alduraibi, S. Campbell, S. Keatings, P. Luke Sam, H. Fraser, A. Arnold, E. Riis, and M. Missous, “Diamond heat sinking of terahertz antennas for continuous-wave photomixing,” *Journal of Applied Physics*, vol. 112, no. 12, p. 123109, 2012.

[12] S. Preu, F. Renner, S. Malzer, G. Döhler, L. Wang, M. Hanson, A. Gossard, T. Wilkinson, and E. Brown, “Efficient terahertz emission from ballistic transport enhanced n-i-p-n-i-p superlattice photomixers,” *Applied Physics Letters*, vol. 90, no. 21, p. 212115, 2007.

[13] N. Chimot, J. Mangeney, P. Crozat, J. Lourtioz, K. Blary, J. Lampin, G. Mouret, D. Bigourd, and E. Fertein, “Photomixing at 1.55 μm in ion-irradiated in0. 53ga 0.47 as on inp,” *Optics express*, vol. 14, no. 5, pp. 1856–1861, 2006.

[14] J. Bjarnason, T. Chan, A. Lee, E. Brown, D. Driscoll, M. Hanson, A. Gossard, and R. Muller, “Eras: Gaas photomixer with two-decade tunability and 12 μ w peak output power,” *Applied Physics Letters*, vol. 85, no. 18, pp. 3983–3985, 2004.

[15] S.-H. Yang, R. Salas, E. M. Krivoy, H. P. Nair, S. R. Bank, and M. Jarrahi, “Characterization of eras: Gaas and luas: Gaas superlattice structures for continuous-wave terahertz wave generation through plasmonic photomixing,” *Journal of Infrared, Millimeter, and Terahertz Waves*, vol. 37, no. 7, pp. 640–648, 2016.

[16] M. Tamagnone, J. Gomez-Diaz, J. Mosig, and J. Perruisseau-Carrier, “Analysis and design of terahertz antennas based on plasmonic resonant graphene sheets,” *Journal of Applied Physics*, vol. 112, no. 11, p. 114915, 2012.

[17] M. Tamagnone, J. Gomez-Diaz, J. R. Mosig, and J. Perruisseau-Carrier, “Reconfigurable terahertz plasmonic antenna concept using a graphene stack,” *Applied Physics Letters*, vol. 101, no. 21, p. 214102, 2012.

[18] V. Ryzhii, M. Ryzhii, V. Mitin, M. Shur, A. Satou, and T. Otsuji, “Terahertz photomixing using plasma resonances in double-graphene layer structures,” *Journal of Applied Physics*, vol. 113, no. 17, p. 174506, 2013.

[19] P.-Y. Chen and A. Alu, “A terahertz photomixer based on plasmonic nanoantennas coupled to a graphene emitter,” *Nanotechnology*, vol. 24, no. 45, p. 455202, 2013.

[20] S. Al-Daffaie, O. Yilmazoglu, F. Küppers, and H. Hartnagel, “Nanogrid-based vertically integrated photomixer for continuous wave terahertz generation,” in *2012 37th International Conference on Infrared, Millimeter, and Terahertz Waves*. IEEE, 2012, pp. 1–3.

[21] ——, “Graphene ltg-gaas photomixer for reliable continuous wave terahertz generation,” in *2013 38th International Conference on Infrared, Millimeter, and Terahertz Waves (IRMMW-THz)*. IEEE, 2013, pp. 1–2.

[22] S. Al-Daffaie, O. Yilmazoglu, F. Küppers, and H. L. Hartnagel, “1-d and 2-d nanocontacts for reliable and efficient terahertz photomixers,” *IEEE Transactions on Terahertz Science and Technology*, vol. 5, no. 3, pp. 398–405, 2015.

[23] T. P. AG. (2020) Toptica’s terascan 780. [Online]. Available: https://www.toptica.com/products/terahertz-systems/time-domain/teraflash-pro/

[24] S. Ragam, T. Tanabe, Y. Oyama, K. Watanabe, and H. Dezaki, “Comparison of cw thz wave spectrometer with laser diode excitation and pulsed thz wave spectrometer with cr: forsterite sources based on difference frequency generation of near-infrared lasers in gap,” *Journal of Infrared, Millimeter, and Terahertz Waves*, vol. 31, no. 10, pp. 1164–1170, 2010.

[25] R. Mendis, C. Sydlo, J. Sigmund, M. Feiginov, P. Meissner, and H. L. Hartnagel, “Tunable cw-thz system with a log-periodic photoconductive emitter,” *Solid-State Electronics*, vol. 48, no. 10-11, pp. 2041–2045, 2004.

[26] G. Carelli, A. Moretti, D. Pereira, and F. Strumia, “Heterodyne frequency measurements of fir laser lines around 1.2 and 1.6 thz,” *IEEE journal of quantum electronics*, vol. 31, no. 1, pp. 144–147, 1995.

[27] R. H. Kingston, *Optical sources, detectors, and systems: fundamentals and applications*. Academic Press, 1995.

[28] E. Brown, F. Smith, and K. McIntosh, “Coherent millimeter-wave generation by heterodyne conversion in low-temperature-grown gaas photoconductors,” *Journal of Applied Physics*, vol. 73, no. 3, pp. 1480–1484, 1993.

[29] R. S. Hansen, “Modeling of the nonlinear response of the intrinsic hgcdte photoconductor by a two-level rate equation with a finite number of carriers available for photoexcitation,” *Applied optics*, vol. 42, no. 24, pp. 4819–4826, 2003.

[30] S. M. Sze and K. K. Ng, *Physics of semiconductor devices*. John wiley & sons, 2006.

[31] E. Brown, “Thz generation by photomixing in ultrafast photoconductors,” in *Terahertz Sensing Technology: Volume 1: Electronic Devices and Advanced Systems Technology*. World Scientific, 2003, pp. 147–195.

[32] S. Preu, G. Döhler, S. Malzer, L. Wang, and A. Gossard, “Tunable, continuous-wave terahertz photomixer sources and applications,” *Journal of Applied Physics*, vol. 109, no. 6, p. 4, 2011.

[33] S. Verghese, K. McIntosh, and E. Brown, “Optical and terahertz power limits in the low-temperature-grown gaas photomixers,” *Applied Physics Letters*, vol. 71, no. 19, pp. 2743–2745, 1997.

[34] A. Rogalski and F. Sizov, “Terahertz detectors and focal plane arrays,” *Opto-electronics review*, vol. 19, no. 3, pp. 346–404, 2011.

[35] E. Moreno, Z. Hemmat, J. Roldán, M. Pantoja, A. Bretones, and S. García, “Time-domain numerical modeling of terahertz receivers based on photoconductive antennas,” *JOSA B*, vol. 32, no. 10, pp. 2034–2041, 2015.

[36] D. Rutledge, D. Neikirk, and D. Kasilingam, “Integrated circuit antennas, infrared and millimeter waves, millimeter components and techniques,” 1983.

[37] F. González and G. Boreman, “Comparison of dipole, bowtie, spiral and log-periodic ir antennas,” *Infrared physics & technology*, vol. 46, no. 5, pp. 418–428, 2005.

[38] Y. Huo, G. W. Taylor, and R. Bansal, “Planar log-periodic antennas on extended hemishperical silicon lenses for millimeter/submillimeter wave detection

applications," *International Journal of Infrared and Millimeter Waves*, vol. 23, no. 6, pp. 819–839, 2002.

[39] J. Dyson, "The equiangular spiral antenna," *IRE Transactions on Antennas and Propagation*, vol. 7, no. 2, pp. 181–187, 1959.

[40] C. Sydlo, *Reliability investigations and development of compound semiconductor devices for microwave and terahertz applications.* Shaker, 2006.

[41] M. Kaspers, A. Bernhart, F. M. zu Heringdorf, G. Dumpich, and R. Möller, "Electromigration and potentiometry measurements of single-crystalline ag nanowires under uhv conditions," *Journal of Physics: Condensed Matter*, vol. 21, no. 26, p. 265601, 2009.

[42] S. Campbell, T. Ackemann, H. Fraser, and M. Missous, "On the thermal dependence of the generation of terahertz radiation by photomixing," *Semiconductor Science and Technology*, vol. 29, no. 3, p. 035006, 2014.

[43] K. S. Novoselov, A. K. Geim, S. V. Morozov, D. Jiang, Y. Zhang, S. V. Dubonos, I. V. Grigorieva, and A. A. Firsov, "Electric field effect in atomically thin carbon films," *science*, vol. 306, no. 5696, pp. 666–669, 2004.

[44] K. D. Sattler, *Handbook of nanophysics: functional nanomaterials.* CRC press, 2010.

[45] P. Li, C. Chen, J. Zhang, S. Li, B. Sun, and Q. Bao, "Graphene-based transparent electrodes for hybrid solar cells," *Frontiers in Materials*, vol. 1, p. 26, 2014.

[46] C. Soldano, A. Mahmood, and E. Dujardin, "Production, properties and potential of graphene," *Carbon*, vol. 48, no. 8, pp. 2127–2150, 2010.

[47] H. Bi, F. Huang, J. Liang, X. Xie, and M. Jiang, "Transparent conductive graphene films synthesized by ambient pressure chemical vapor deposition used as the front electrode of cdte solar cells," *Advanced materials*, vol. 23, no. 28, pp. 3202–3206, 2011.

[48] R. Murali, Y. Yang, K. Brenner, T. Beck, and J. D. Meindl, "Breakdown current density of graphene nanoribbons," *Applied Physics Letters*, vol. 94, no. 24, p. 243114, 2009.

[49] Y. Jiang, L. Gao, X. Wang, W. Dai, J. Wu, X. Dai, and G. Zou, "Laser tailored multilayer graphene grids for transparent conductive electrodes," *Nanoscale research letters*, vol. 14, no. 1, p. 207, 2019.

[50] K.-J. Lee, A. P. Chandrakasan, and J. Kong, "Breakdown current density of cvd-grown multilayer graphene interconnects," *IEEE Electron Device Letters*, vol. 32, no. 4, pp. 557–559, 2011.

[51] A. A. Balandin, "Thermal properties of graphene and nanostructured carbon materials," *Nature materials*, vol. 10, no. 8, pp. 569–581, 2011.

[52] G. Liu, D. Teweldebrhan, and A. A. Balandin, "Tuning of graphene properties via controlled exposure to electron beams," *IEEE Transactions on Nanotechnology*, vol. 10, no. 4, pp. 865–870, 2010.

[53] M. Craciun, S. Russo, M. Yamamoto, and S. Tarucha, "Tuneable electronic properties in graphene," *Nano Today*, vol. 6, no. 1, pp. 42–60, 2011.

[54] A. A. Balandin, S. Ghosh, W. Bao, I. Calizo, D. Teweldebrhan, F. Miao, and C. N. Lau, "Superior thermal conductivity of single-layer graphene," *Nano letters*, vol. 8, no. 3, pp. 902–907, 2008.

[55] J. Che, T. Çağın, W. Deng, and W. A. Goddard III, "Thermal conductivity of diamond and related materials from molecular dynamics simulations," *The Journal of Chemical Physics*, vol. 113, no. 16, pp. 6888–6900, 2000.

[56] d. Ghosh, I. Calizo, D. Teweldebrhan, E. P. Pokatilov, D. L. Nika, A. A. Balandin, W. Bao, F. Miao, and C. N. Lau, "Extremely high thermal conductivity of graphene: Prospects for thermal management applications in nanoelectronic circuits," *Applied Physics Letters*, vol. 92, no. 15, p. 151911, 2008.

[57] S. Park and R. S. Ruoff, "Chemical methods for the production of graphenes," *Nature nanotechnology*, vol. 4, no. 4, p. 217, 2009.

[58] M. J. Allen, V. C. Tung, and R. B. Kaner, "Honeycomb carbon: a review of graphene," *Chemical reviews*, vol. 110, no. 1, pp. 132–145, 2010.

[59] L. M. Viculis, J. J. Mack, and R. B. Kaner, "A chemical route to carbon nanoscrolls," *Science*, vol. 299, no. 5611, pp. 1361–1361, 2003.

[60] A. Reina, X. Jia, J. Ho, D. Nezich, H. Son, V. Bulovic, M. S. Dresselhaus, and J. Kong, “Large area, few-layer graphene films on arbitrary substrates by chemical vapor deposition,” *Nano letters*, vol. 9, no. 1, pp. 30–35, 2009.

[61] N. Liu, F. Luo, H. Wu, Y. Liu, C. Zhang, and J. Chen, “One-step ionic-liquid-assisted electrochemical synthesis of ionic-liquid-functionalized graphene sheets directly from graphite,” *Advanced Functional Materials*, vol. 18, no. 10, pp. 1518–1525, 2008.

[62] N. Behabtu, J. R. Lomeda, M. J. Green, A. L. Higginbotham, A. Sinitskii, D. V. Kosynkin, D. Tsentalovich, A. N. G. Parra-Vasquez, J. Schmidt, E. Kesselman *et al.*, “Spontaneous high-concentration dispersions and liquid crystals of graphene,” *Nature nanotechnology*, vol. 5, no. 6, pp. 406–411, 2010.

[63] Y. Hernandez, V. Nicolosi, M. Lotya, F. M. Blighe, Z. Sun, S. De, I. McGovern, B. Holland, M. Byrne, Y. K. Gun’Ko *et al.*, “High-yield production of graphene by liquid-phase exfoliation of graphite,” *Nature nanotechnology*, vol. 3, no. 9, p. 563, 2008.

[64] A. B. Bourlinos, V. Georgakilas, R. Zboril, T. A. Steriotis, and A. K. Stubos, “Liquid-phase exfoliation of graphite towards solubilized graphenes,” *small*, vol. 5, no. 16, pp. 1841–1845, 2009.

[65] X. Wang, H. You, F. Liu, M. Li, L. Wan, S. Li, Q. Li, Y. Xu, R. Tian, Z. Yu *et al.*, “Large-scale synthesis of few-layered graphene using cvd,” *Chemical Vapor Deposition*, vol. 15, no. 1-3, pp. 53–56, 2009.

[66] E. Rollings, G.-H. Gweon, S. Zhou, B. Mun, J. McChesney, B. Hussain, A. Fedorov, P. First, W. De Heer, and A. Lanzara, “Synthesis and characterization of atomically thin graphite films on a silicon carbide substrate,” *Journal of Physics and Chemistry of Solids*, vol. 67, no. 9-10, pp. 2172–2177, 2006.

[67] W. Zhang, J. Cui, C.-a. Tao, Y. Wu, Z. Li, L. Ma, Y. Wen, and G. Li, “A strategy for producing pure single-layer graphene sheets based on a confined self-assembly approach,” *Angewandte Chemie International Edition*, vol. 48, no. 32, pp. 5864–5868, 2009.

[68] N. Li, Z. Wang, K. Zhao, Z. Shi, Z. Gu, and S. Xu, “Large scale synthesis of n-doped multi-layered graphene sheets by simple arc-discharge method,” *Carbon*, vol. 48, no. 1, pp. 255–259, 2010.

[69] S. Karmakar, N. V. Kulkarni, A. B. Nawale, N. P. Lalla, R. Mishra, V. Sathe, S. Bhoraskar, and A. Das, "A novel approach towards selective bulk synthesis of few-layer graphenes in an electric arc," *Journal of Physics D: Applied Physics*, vol. 42, no. 11, p. 115201, 2009.

[70] C.-D. Kim, B.-K. Min, and W.-S. Jung, "Preparation of graphene sheets by the reduction of carbon monoxide," *Carbon*, vol. 47, no. 6, pp. 1610–1612, 2009.

[71] D. V. Kosynkin, A. L. Higginbotham, A. Sinitskii, J. R. Lomeda, A. Dimiev, B. K. Price, and J. M. Tour, "Longitudinal unzipping of carbon nanotubes to form graphene nanoribbons," *Nature*, vol. 458, no. 7240, pp. 872–876, 2009.

[72] L. Jiao, L. Zhang, X. Wang, G. Diankov, and H. Dai, "Narrow graphene nanoribbons from carbon nanotubes," *Nature*, vol. 458, no. 7240, pp. 877–880, 2009.

[73] A. Hirsch, "Unzipping carbon nanotubes: a peeling method for the formation of graphene nanoribbons," *Angewandte Chemie International Edition*, vol. 48, no. 36, pp. 6594–6596, 2009.

[74] A. Mattausch and O. Pankratov, "Density functional study of graphene overlayers on sic," *physica status solidi (b)*, vol. 245, no. 7, pp. 1425–1435, 2008.

[75] Z. Ni, W. Chen, X. Fan, J. Kuo, T. Yu, A. Wee, and Z. Shen, "Raman spectroscopy of epitaxial graphene on a sic substrate," *Physical Review B*, vol. 77, no. 11, p. 115416, 2008.

[76] M. Sprinkle, P. Soukiassian, W. De Heer, C. Berger, and E. Conrad, "Epitaxial graphene: the material for graphene electronics," *physica status solidi (RRL)–Rapid Research Letters*, vol. 3, no. 6, pp. A91–A94, 2009.

[77] A. C. S. ACS Material LLC. (2020) Trivial transfer graphene$^{\text{TM}}$. [Online]. Available: https://www.acsmaterial.com/

[78] S. J. Chae, F. Güneş, K. K. Kim, E. S. Kim, G. H. Han, S. M. Kim, H.-J. Shin, S.-M. Yoon, J.-Y. Choi, M. H. Park *et al.*, "Synthesis of large-area graphene layers on poly-nickel substrate by chemical vapor deposition: wrinkle formation," *Advanced materials*, vol. 21, no. 22, pp. 2328–2333, 2009.

[79] X. Li, W. Cai, J. An, S. Kim, J. Nah, D. Yang, R. Piner, A. Velamakanni, I. Jung, E. Tutuc *et al.*, "Large-area synthesis of high-quality and uniform graphene films on copper foils," *science*, vol. 324, no. 5932, pp. 1312–1314, 2009.

[80] A. Guermoune, T. Chari, F. Popescu, S. S. Sabri, J. Guillemette, H. S. Skulason, T. Szkopek, and M. Siaj, "Chemical vapor deposition synthesis of graphene on copper with methanol, ethanol, and propanol precursors," *Carbon*, vol. 49, no. 13, pp. 4204–4210, 2011.

[81] L. G. De Arco, Y. Zhang, A. Kumar, and C. Zhou, "Synthesis, transfer, and devices of single-and few-layer graphene by chemical vapor deposition," *IEEE Transactions on Nanotechnology*, vol. 8, no. 2, pp. 135–138, 2009.

[82] K. S. Novoselov, D. Jiang, F. Schedin, T. Booth, V. Khotkevich, S. Morozov, and A. K. Geim, "Two-dimensional atomic crystals," *Proceedings of the National Academy of Sciences*, vol. 102, no. 30, pp. 10 451–10 453, 2005.

[83] P. Nemes-Incze, Z. Osváth, K. Kamarás, and L. Biró, "Anomalies in thickness measurements of graphene and few layer graphite crystals by tapping mode atomic force microscopy," *Carbon*, vol. 46, no. 11, pp. 1435–1442, 2008.

[84] J. C. Meyer, A. K. Geim, M. I. Katsnelson, K. S. Novoselov, T. J. Booth, and S. Roth, "The structure of suspended graphene sheets," *Nature*, vol. 446, no. 7131, pp. 60–63, 2007.

[85] Z. Peng, F. Somodi, S. Helveg, C. Kisielowski, P. Specht, and A. T. Bell, "High-resolution in situ and ex situ tem studies on graphene formation and growth on pt nanoparticles," *Journal of catalysis*, vol. 286, pp. 22–29, 2012.

[86] G. Wang, J. Yang, J. Park, X. Gou, B. Wang, H. Liu, and J. Yao, "Facile synthesis and characterization of graphene nanosheets," *The Journal of Physical Chemistry C*, vol. 112, no. 22, pp. 8192–8195, 2008.

[87] C. Casiraghi, A. Hartschuh, E. Lidorikis, H. Qian, H. Harutyunyan, T. Gokus, K. S. Novoselov, and A. Ferrari, "Rayleigh imaging of graphene and graphene layers," *Nano letters*, vol. 7, no. 9, pp. 2711–2717, 2007.

[88] A. C. Ferrari, J. Meyer, V. Scardaci, C. Casiraghi, M. Lazzeri, F. Mauri, S. Piscanec, D. Jiang, K. Novoselov, S. Roth *et al.*, "Raman spectrum of graphene and graphene layers," *Physical review letters*, vol. 97, no. 18, p. 187401, 2006.

[89] F. Akbar, M. Kolahdouz, S. Larimian, B. Radfar, and H. Radamson, "Graphene synthesis, characterization and its applications in nanophotonics, nanoelectronics, and nanosensing," *Journal of Materials Science: Materials in Electronics*, vol. 26, no. 7, pp. 4347–4379, 2015.

[90] M. Gautam, Z. Shi, and A. H. Jayatissa, “Graphene films as transparent electrodes for photovoltaic devices based on cadmium sulfide thin films,” *Solar Energy Materials and Solar Cells*, vol. 163, pp. 1–8, 2017.

[91] S. Roscher, R. Hoffmann, and O. Ambacher, “Determination of the graphene–graphite ratio of graphene powder by raman 2d band symmetry analysis,” *Analytical methods*, vol. 11, no. 9, pp. 1224–1228, 2019.

[92] A. Gupta, G. Chen, P. Joshi, S. Tadigadapa, and P. Eklund, “Raman scattering from high-frequency phonons in supported n-graphene layer films,” *Nano letters*, vol. 6, no. 12, pp. 2667–2673, 2006.

[93] Tydex. (2020) Thz devices, golay detectors. [Online]. Available: http://www.tydexoptics.com/

[94] Z. Ni, H. Wang, J. Kasim, H. Fan, T. Yu, Y. H. Wu, Y. Feng, and Z. Shen, “Graphene thickness determination using reflection and contrast spectroscopy,” *Nano letters*, vol. 7, no. 9, pp. 2758–2763, 2007.

[95] O. Loebich, “The optical properties of gold,” *Gold bulletin*, vol. 5, no. 1, pp. 2–10, 1972.

[96] J. B. Soole and H. Schumacher, “Ingaas metal-semiconductor-metal photodetectors for long wavelength optical communications,” *Quantum Electronics, IEEE Journal of*, vol. 27, no. 3, pp. 737–752, 1991.

[97] Y. C. Lim and R. A. Moore, “Properties of alternately charged coplanar parallel strips by conformal mappings,” *IEEE Transactions on Electron Devices*, vol. 15, no. 3, pp. 173–180, 1968.

[98] W. Hilberg, “From approximations to exact relations for characteristic impedances,” *Microwave Theory and Techniques, IEEE Transactions on*, vol. 17, no. 5, pp. 259–265, 1969.

[99] A. Jumaah, S. Al-Daffaie, O. Yilmazoglu, F. Küppers, and T. Kusserow, “Interdigital multilayer-graphene nanoelectrodes for continuous wave terahertz photomixers,” in *2019 European Microwave Conference in Central Europe (EuMCE)*. IEEE, 2019, pp. 265–267.

[100] ——, “Experimental investigation of graphene layers as 2d nanoelectrode for continuous wave terahertz generation,” in *2019 44th International Conference*

on Infrared, Millimeter, and Terahertz Waves (IRMMW-THz). IEEE, 2019, pp. 1–2.

[101] A. Jumaah, S. Al-Daffaie, O. Yilmazoglu, and F. Küppers, "Graphene enhanced 2-d nanoelectrode for continuous wave terahertz photomixers," in *2018 43rd International Conference on Infrared, Millimeter, and Terahertz Waves (IRMMW-THz).* IEEE, 2018, pp. 1–2.

[102] T. P. AG. (2020) Toptica's terascan 780. [Online]. Available: https://www.toptica.com/products/terahertz-systems/frequency-domain/terascan/

[103] Y. Wu, J. Xiang, C. Yang, W. Lu, and C. M. Lieber, "Single-crystal metallic nanowires and metal/semiconductor nanowire heterostructures," *Nature*, vol. 430, no. 6995, pp. 61–65, 2004.

[104] S. De, T. M. Higgins, P. E. Lyons, E. M. Doherty, P. N. Nirmalraj, W. J. Blau, J. J. Boland, and J. N. Coleman, "Silver nanowire networks as flexible, transparent, conducting films: extremely high dc to optical conductivity ratios," *ACS nano*, vol. 3, no. 7, pp. 1767–1774, 2009.

[105] L. Hu, H. Wu, and Y. Cui, "Metal nanogrids, nanowires, and nanofibers for transparent electrodes," *MRS bulletin*, vol. 36, no. 10, pp. 760–765, 2011.

[106] M. M. Wiecha, S. Al-Daffaie, A. Bogdanov, M. D. Thomson, O. Yilmazoglu, F. Küppers, A. Soltani, and H. G. Roskos, "Direct near-field observation of surface plasmon polaritons on silver nanowires," *ACS omega*, 2019.

[107] A. L. Pyayt, B. Wiley, Y. Xia, A. Chen, and L. Dalton, "Integration of photonic and silver nanowire plasmonic waveguides," *Nature nanotechnology*, vol. 3, no. 11, p. 660, 2008.

[108] H. Lee, K. Heo, J. Park, Y. Park, S. Noh, K. S. Kim, C. Lee, B. H. Hong, J. Jian, and S. Hong, "Graphene–nanowire hybrid structures for high-performance photoconductive devices," *Journal of Materials Chemistry*, vol. 22, no. 17, pp. 8372–8376, 2012.

[109] M.-S. Lee, K. Lee, S.-Y. Kim, H. Lee, J. Park, K.-H. Choi, H.-K. Kim, D.-G. Kim, D.-Y. Lee, S. Nam *et al.*, "High-performance, transparent, and stretchable electrodes using graphene–metal nanowire hybrid structures," *Nano letters*, vol. 13, no. 6, pp. 2814–2821, 2013.

[110] X. Huang, Z. Zeng, Z. Fan, J. Liu, and H. Zhang, "Graphene-based electrodes," *Advanced Materials*, vol. 24, no. 45, pp. 5979–6004, 2012.

[111] A. Jumaah, S. Al-Daffaie, O. Yilmazoglu, and F. Küppers, "Graphene–nanowire hybrid photomixer for continuous-wave terahertz generation," in *2017 42nd International Conference on Infrared, Millimeter, and Terahertz Waves (IRMMW-THz)*. IEEE, 2017, pp. 1–2.

Own Publications

Journals

1. **Alaa Jumaah**, Shihab Al-Daffaie, Oktay Yilmazoglu, Thomas Kusserow: Continuous-wave terahertz emitter with hybrid nanoelectrodes based on graphene and nanowire. OSA Continuum 05/2020; Volume 3(Issue 7): 1826-1833.
   DOI: **10.1364/OSAC.392837**.
2. Hua Chen, Zhi-Yuan Zhou, **Alaa Jabbar Jumaah Zangana**, Zhen-Qiang Yin, Juan Wu, Yun-Guang Han, Shuang Wang, Hong-Wei Li, De-Yong He, Shelan Khasro Tawfeeq, Bao-Sen Shi, Guang-Can Guo, Wei Chen, Zheng-Fu Han: Continuous-wave terahertz emitter with hybrid nanoelectrodes based on graphene and nanowire. OSA Continuum 05/2020; Volume 3(Issue 7): 1826-1833.
   DOI: **10.1038/srep20962**.

Conference Proceedings

1. **Alaa Jumaah**, Shihab Al-Daffaie, Thomas Kusserow, Idelfonso Tafur Monroy: Highly Transparent Graphene Electrodes For CW THz Applications. 45th International Conference on Infrared, Millimeter, and Terahertz waves (IRMMW-THz), Buffalo, USA; 2020.
   DOI: **10.1109/IRMMW-THz46771.2020.9370966**.
2. **Alaa Jumaah**, Shihab Al-Daffaie, Thomas Kusserow, Idelfonso Tafur Monroy: High Performance Graphene-Based CW THz Photoconductive Detector. 45th International Conference on Infrared, Millimeter, and Terahertz waves (IRMMW-THz), Buffalo, USA; 2020.
   DOI: **10.1109/IRMMW-THz46771.2020.9370371**.
3. **Alaa Jumaah**, Shihab Al-Daffaie, Oktay Yilmazoglu, Franko Küppers, Thomas Kusserow: Experimental Investigation of Graphene Layers as 2D Nanoelectrode for Continuous Wave Terahertz Generation. 44th International Conference on Infrared, Millimeter, and Terahertz waves (IRMMW-THz), Paris, France; 2019.
   DOI: **10.1109/IRMMW-THz.2019.8874024**.

4. Verónica Laín Rubio, Shihab Al-Daffaie, **Alaa Jumaah**, Thomas Kusserow: Design and Implementation of a Terahertz Integrated Lens-Antenna for a Nanocontacts Based Photomixer. 44th International Conference on Infrared, Millimeter, and Terahertz waves (IRMMW-THz), Paris, France; 2019.
   DOI: **10.1109/IRMMW-THz.2019.8874028**.
5. **Alaa Jumaah**, Shihab Al-Daffaie, Oktay Yilmazoglu, Franko Küppers, Thomas Kusserow: Interdigital Multilayer-Graphene Nanoelectrodes for Continuous Wave Terahertz photomixers. European Microwave Conference in Central Europe (EuMCE), Prague, Czech Republic; 2019.
6. Dominika Warmowska, **Alaa Jumaah**, Shihab Al-Daffaie, Oktay Yilmazoglu, Zbynek Raida: Manufacture of high-gain, circularly polarized terahertz antenna array in silicon technology. 8th Asia-Pacific Conference on Antennas and Propagation (APCAP), Incheon, Korea, 2019.
   DOI: **10.1109/APCAP47827.2019.9472054**.
7. **Alaa Jumaah**, Shihab Al-Daffaie, Oktay Yilmazoglu, Franko Küppers: Graphene Enhanced 2-D Nanoelectrode for Continuous Wave Terahertz Photomixers. 43rd International Conference on Infrared, Millimeter, and Terahertz waves (IRMMW-THz), Nagoya, Japan; 2018.
   DOI: **10.1109/IRMMW-THz.2018.8510179**.
8. Shihab Al-Daffaie, Oktay Yilmazoglu, **Alaa Jumaah**, Franko Küppers: First Demonstration of Continuous Wave Terahertz Radiation from Semi-Insulating GaAs Photomixer with Nanowire. 43rd International Conference on Infrared, Millimeter, and Terahertz waves (IRMMW-THz), Nagoya, Japan; 2018.
   DOI: **10.1109/IRMMW-THz.2018.8510294**.
9. **Alaa Jumaah**, Shihab Al-Daffaie, Oktay Yilmazoglu, Franko Küppers: Graphene – Nanowire hybrid photomixer for continuous-wave terahertz generation. 42nd International Conference on Infrared, Millimeter, and Terahertz waves (IRMMW-THz), Cancun, Mexico; 2017.
   DOI: **10.1109/IRMMW-THz.2017.8067085**.